Combined Analysis using x-ray and neutron scattering

Daniel Chateigner

▶ **To cite this version:**

Daniel Chateigner. Combined Analysis using x-ray and neutron scattering. DEA. 2006. cel-00109040v1

HAL Id: cel-00109040

https://cel.hal.science/cel-00109040v1

Submitted on 23 Oct 2006 (v1), last revised 26 Oct 2010 (v2)

HAL is a multi-disciplinary open access archive for the deposit and dissemination of scientific research documents, whether they are published or not. The documents may come from teaching and research institutions in France or abroad, or from public or private research centers.

L'archive ouverte pluridisciplinaire **HAL**, est destinée au dépôt et à la diffusion de documents scientifiques de niveau recherche, publiés ou non, émanant des établissements d'enseignement et de recherche français ou étrangers, des laboratoires publics ou privés.

Combined Analysis: structure-texture-microstructure-phase-stresses-reflectivity determination by x-ray and neutron scattering

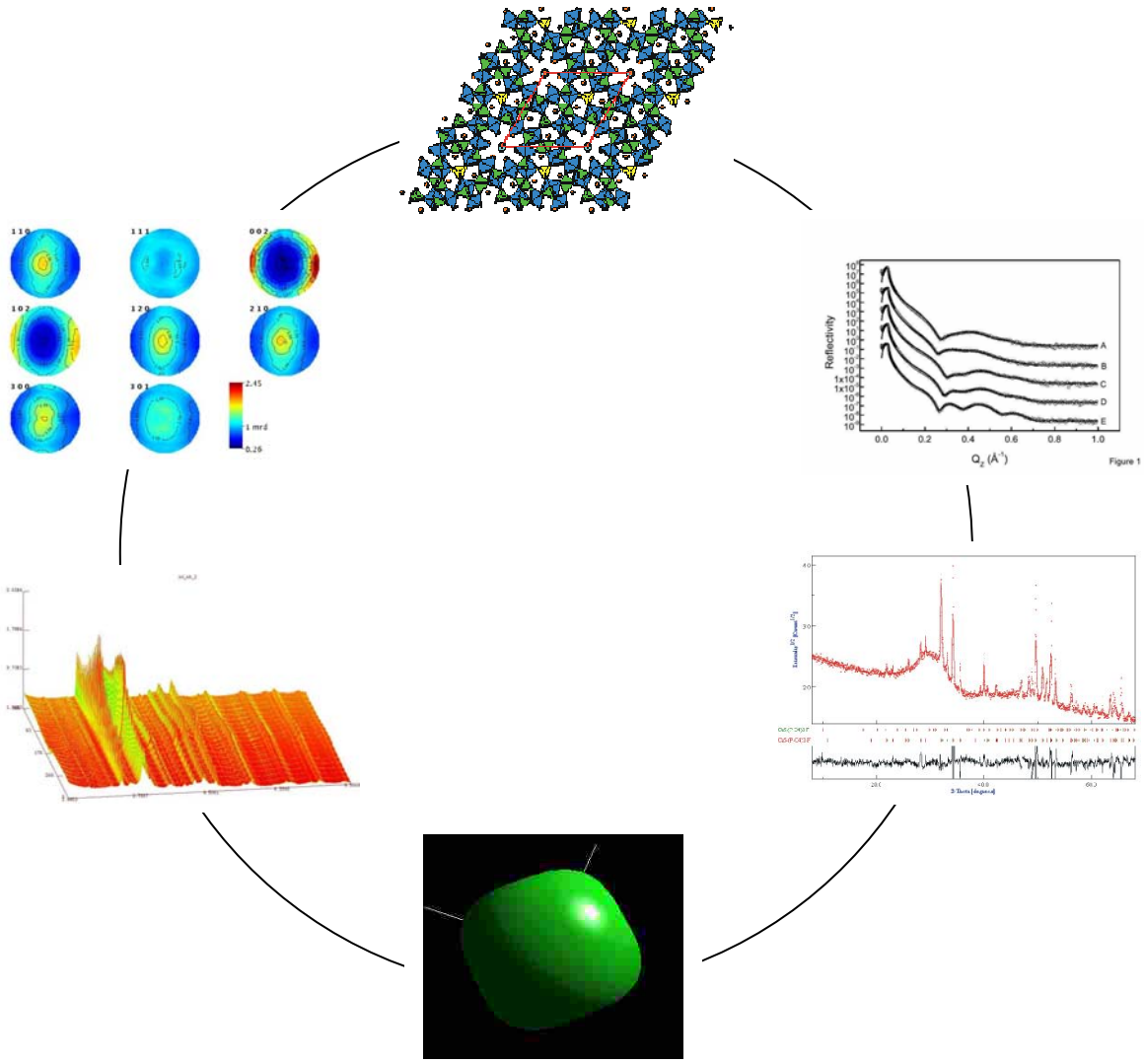

Daniel Chateigner

Laboratoire de Cristallographie et Sciences des Matériaux
UMR CNRS 6508,

Ecole Nationale Supérieure d'Ingénieurs de Caen

Département Mesures Physiques

Institut Universitaire de Technologie de Caen

Centre National de la Recherche Scientifique

Pôle Universitaire Normand

Sponsors:

INEL S.A.

International Union of Crystallography

Combined Analysis: structure-texture-microstructure-phase-stresses-reflectivity determination by x-ray and neutron scattering

Daniel Chateigner

daniel.chateigner@ensicaen.fr

CRISMAT-ENSICAEN, UMR CNRS n°6508, 6 Bd. M. Juin, F-14050 Caen, France

IUT Mesures-Physiques, Université de Caen Basse-Normandie, Caen, France

http://www.ecole.ensicaen.fr/~chateign/texture/combined.pdf

Some typographical mistakes may have been introduced throughout this document. Suggestions and corrections are very welcome.

0. Introduction

Solid state chemistry and technology recent developments gave rise to the necessity of intensive structural analysis from single crystal diffraction. However for many solids, single crystal growth is not easy to manage and sometimes impossible. When this is the case, or when structural defects cannot be overcome, the corresponding phases have often been forsaken, due to the inherent difficulties to carry out crystallographic characterisations on polycrystals. But in the last decades powder diffraction techniques progressed significantly, notably due to the Rietveld approach (Rietveld, 1969) and computer science developments. Undoubtedly these developments are of prior importance in the study of solids that do not form large crystals, but also of all materials elaborated by classical solid state reactions, thin deposited structures, natural materials like clays and more recently nanomaterials in which the required properties are intimately linked to the stabilisation of small crystals.

Since the Rietveld method's birth, several ten thousands of structures have been refined and some thousands have been resolved *ab-initio* from the only diffraction data of powder samples. The number of laboratories and industries using this technique, still fairly new when dealing with the incorporation of various formalisms like in the combined approach, does not stop increasing.

However, materials having specific properties are often elaborated from low symmetry phases, which are consequently anisotropic. Property's optimisation is then conditioned by the elaboration processes which have to keep the intrinsic microscopic anisotropy of the constituting crystals at the macroscopic level. These elaboration techniques are complex (alignment under uniaxial pressure, magnetic or electric fields, thermal gradients, flux or substrate growing ... and combinations) and often sample preparation is a hard, time consuming, matter. Naturally, non-destructive characterisations are then required. Unfortunately, when samples are oriented, which was not often the case until recently, most of the characterisation techniques (as the Rietveld analysis of concerns here) require samples grinding. Very often this grinding is not acceptable, for the previously described reasons, but also in the case of rare samples (fossils, comets ...) or simply when grinding modifies the physical behaviour of the samples themselves (thin films, residual stress materials ...). Sometimes grinding is simply not possible, imagine peeling off a 10 nm thick film on a substrate !

In all these cases, the combined analysis becomes essential.

The first part of this document is dedicated to some basic notions concerning diffraction by polycrystals. The various peak profiles used are described and some, most common combined analysis instrumental set-up detailed.

In the second part, powder diffraction data treatment is introduced. In particular, the Rietveld analysis is detailed, including treatment of all the information provided by diffraction diagrams, when texture is not present in the sample or simple to treat.

The third part deals with the automatic phase indexing, necessary step to solve a structure *ab-initio*.

Since its effect prevails on real samples where textures are often stabilised, quantitative texture analysis is detailed in the fourth part.

The fifth part is dedicated to microstructural aspects (isotropic and anisotropic crystal sizes and microdistortions) of the poder diffraction profiles.

In part six, quantitative phase analysis from Rietveld analysis is introduced.

Part seven describes residual stress analysis for isotropic and anisotropic materials.

The eighth part focuses on specular x-ray reflectivity and the various models associated.

Finally the combined analysis is described, showing all the dilemma that show up when one looks at only one part of the analyses, and case examples are shown as illustration of the methodology.

1 Some basic notions about powder diffraction

1.1. Crystallite, grain, polycrystal and powder

A polycrystal, dealing with diffraction, is a solid substance divided in very small homogeneous particles, elementary single crystals called crystallites. Crystallites are tridimensional domains which propagate an incident x-ray or neutron wave in a coherent way without phase lost. Crystallites are also called sometimes "coherent domains" in crystallography. A grain (as the ones we can observe using a microscope for instance) can be constituted of many crystallites or only a single crystallite. A single crystal is then composed of only one crystallite, and a polycrystal of an ensemble of crystallites.

A powder is an aggregate of crystallites (metal piece, ceramic, polymer or simply a compacted or not compacted powder) of varying number, shape, size and crystalline state. It is then a polycrystal. But an ideal powder or "standard", again concerning diffraction experiments, is constituted of a large number (several ten thousands at least) of crystallites in a perfect crystalline state (without microdistortion or any other defects) which exhibit a very narrow monomodal size and shape distribution. Furthermore, the standard powder has crystallites which are randomly oriented one to each other (without texture). In such conditions, whatever the incident beam angle, it always exist the same volume fraction of crystallites oriented in such a way that they are satisfying the Bragg law (Bragg, 1912), hereby diffracting. We call "powder" in this document the standard powder, and polycrystal the regular powder.

1.2. Bragg law and harmonic reflections

1.2.1. Bragg law

This law establishes that a diffracted beam exists for a wavelength λ, at an angle 2θ between the incident and diffracted beams (Figure 1), by the atoms lying in the {hkl} planes at an intereticular distance d_{hkl} one from each other if the relation:

- 1

$$2d_{hkl}\sin\theta = n\lambda$$

is satisfied, in which n is the order of the reflection.

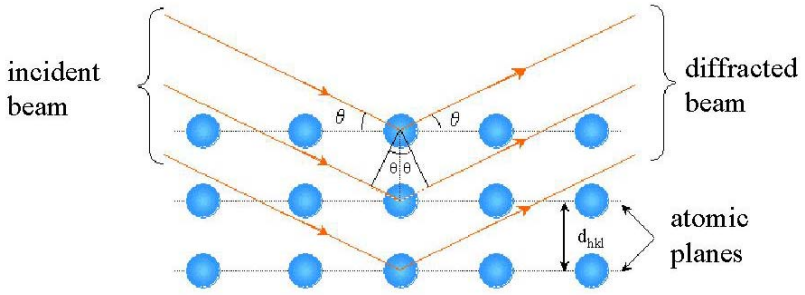

Figure 1: Schematic illustration of Bragg's law

1.2.2. Monochromator

A direct application of the Bragg law is its capacity to select discrete wavelength radiation components among a polychromatic incident source. Looking at equation - 1, one sees that, provided a given single crystal with specific $d_{hk\ell}$ interreticular distances and an incident polychromatic beam at θ from the planes surface, the diffracted beam located at 2θ from the incident beam will only be composed of one radiation λ for which the Bragg law is satisfied. This is a monochromator. Of course the wavelength resolution depends on the single crystal quality and in practice a given Δλ will be selected, that can be used in experiments.

1.2.3. Harmonic radiation components

Even for a perfect single crystal, the monochromator however can select other radiation components, which still satisfy equation - 1. Since $(d_{hk\ell})/n$ (n a positive integer) planes exist parallel to the ones that provide the λ radiation, any λ/n wavelength contribution will also respect the Bragg law, hence diffract. Such λ/2, λ/3 ..., contributions are called harmonics.

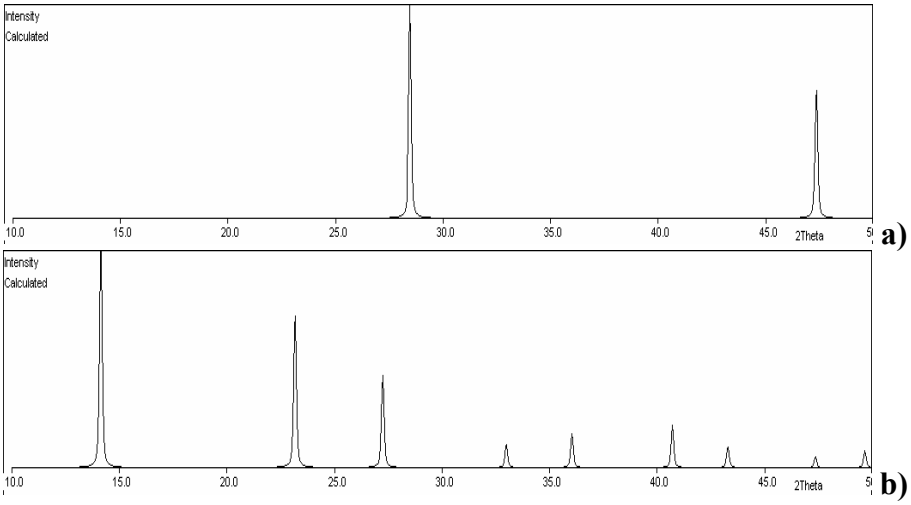

Figure 2: Simulated x-ray diffraction diagrams for a Si powder, for λ = 1.5406 Å **(a)** and for λ/2 = 0.7703 Å **(b)**. Intensities for the λ/2 contributions have been enhanced for visibility.

Figure 2 illustrates the λ/2 occurrence on simulated powder diagrams for Si, in the 10° ≤ 2θ ≤ 50° range. The use of the nominal wavelength (1.5406 Å, Figure 2a) only provides with the 111 and 220 lines in the available range, while the λ/2 contribution (0.7703 Å, Figure 2b) would make all the 11 first lines appearing (*i.e.* 111, 220, 311, 222, 400, 331, 422, 511, 333, 440, 531). Using classical x-ray generators the strong x-ray emission are discrete lines of a transition metal element (*e.g.* the Cu Kα line), for which the monochromator is adjusted. At half energy of such lines (*e.g.* λ/2) corresponds a comparatively very low *bremstralung*, making the harmonics in general weak compared to the main selected radiation. However in some cases like thin films deposited on single crystal substrates, the harmonic diffraction lines are sometimes larger than the film peaks. Using synchrotron x-rays or thermal neutrons the

incident spectrum is on the contrary continuous, and harmonics can be of non negligible intensity.

In practice the harmonic lines are hardly visible from powder diffraction, and even on large single crystals the λ/2 is often the only one detected.

1.3. Geometrical conditions of diffraction, Ewald sphere

The geometrical aspect of powder diffraction is represented with the help of the Ewald sphere, of radius $1/\lambda$, when each reciprocal vector $\mathbf{h} = <hk\ell>^*$ is allowed to take all the possible orientations (Figure 3):

The extremities of the vectors **h** are localised on a sphere, called {hkl} pole sphere, of centre O' and radius $||\mathbf{h}||$. Each resulting pole sphere intercepts the Ewald sphere on a small circle, diffracted rays being distributed on a cone called diffraction cone, which axis is co-linear with the incident beam, and of half-angle at summit $2\theta_{hkl}$. Under these conditions, for the pole sphere vectors having their extremity on the small circle, Bragg's law is satisfied and a diffracted beam emerges giving the so-called Debye-Scherrer rings on a flat detector.

For a powder, the crystallite orientations in the sample are randomly distributed, and the **h** vectors extremities cover all the pole spheres. In the case of preferred orientations (or texture), vectors extremities are around more or less localised arcs and zones called poles, which can be really punctual in the case of single crystals or strongly oriented polycrystals.

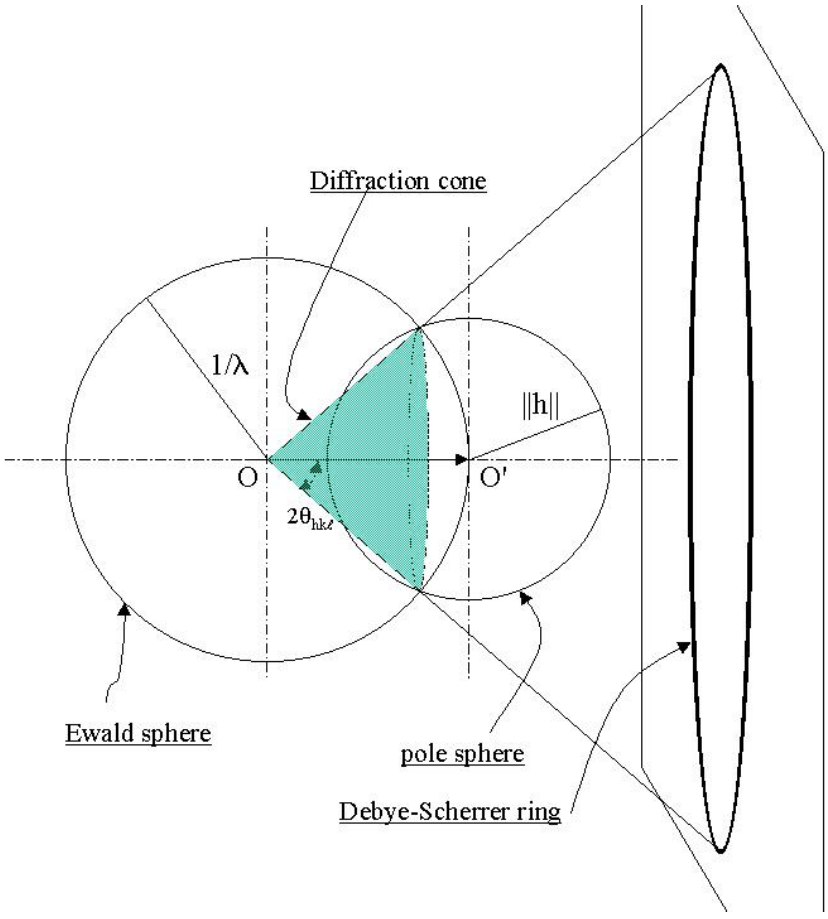

Figure 3: Ewald and pole sphere, Debye-Scherrer rings, geometrical interpretation of diffraction

1.4. Imperfect powders

The geometrical representation is however too much simplistic for a correct description of the polycrystal diffraction phenomenon, because it requires three assumptions:

(i) Crystallite dimensions are considered infinite compared to typical distances between two close scatterers,

(ii) A perfect tridimensionnal order,

(iii) The punctual source delivers a monochromatic radiation of wavelength λ, sample dimensions are negligible and the experimental setup does not show any aberration.

When these three conditions are verified, the intensity diffracted by the (hkl) planes can be represented by a Dirac distribution located at $2\theta_{hkl}$ relative to the incident beam. In reality condition (iii) is never respected and conditions (i) and (ii) can be unsatisfied for imperfect sample crystalline states. Consequently, the three conditions can be the cause of a diffraction line broadening. Hence:

- The condition (i) is no longer satisfied as soon as the crystallite dimensions are small enough (typically lower than 300 nm for an experimental resolution of common laboratory set-up). The coherent domain limits are always defects (surfaces, stacking faults, dislocations, twins, polytypism …). In such case the former work of Scherrer [1918] shows in an approximate way that the crystallite size is inversely proportional to the width of the reflection.

- The condition (ii) is no longer satisfied when the sample exhibits crystalline imperfections like microdistortions induces by internal microstresses, stoechiometric inhomogeneities, dislocations, surface or point defects, stacking faults ...

- The condition (iii) is just never satisfied because any instrument has its own aberrations which are influencing the used spectral domain. These are affecting both the shapes, widths and positions of the diffraction lines. The resulting peak broadening is represented by the function *g(x)* or "instrument resolution function", x being an appropriate variable for the kind of measure used (in one dimensional measurements).

1.5. Origin of the diffraction line profiles

Powder diffraction raw data are composed generally of a list of intensities measured at many angular positions using a constant angular step in a given angular range. The first task of the experimentalist is then to reduce these data (recorded diagram) into observation sets that can be analysed using diffraction and crystallographic knowledge (unit-cell parameters, bond distances and angles, crystallite sizes, volume fractions, …). This is not feasible without knowing *a priori* the contribution of each of the previously mentioned effects to the observed line profiles h(x). This latter is in fact composed of two contributions, from the sample, f(x), for the conditions (i) et (ii), and g(x) from the instrument (condition (iii)).

Sample and instrument contributions convolute into the observed profile h(x), in the real mathematical and signal treatment senses [Jones 1938]:

- 2
$$h(x) = f(x) \otimes g(x) = \int_{-\infty}^{+\infty} f(y)g(x-y)dy$$

where x and y variables define the angular position of each measured point of the profile and have the same dimensions as 2θ, or as the reciprocal used variable.

1.5.1 Origin of g(x)

Instrumental aberrations are technique dependant (Bragg-Brentano geometry, Guinier camera, …). The instrument resolution function g(x) is the result of the convolution of the different aberration profile contributions, purely geometrical (beam divergence, optics misalignments, deviation from punctuality of the source, collimator slit widths, …), or physical like the emitted spectral width and distribution of the incident radiation [Alexander 1948, Alexander 1950, Alexander 1955].

It is interesting to note that g(x) is depending on the variable used in the experiment (Bragg angle in constant-wavelength set-up or wavelength for energy dispersive instruments for instance). The angular variation of the full-width at half-maximum H (or FWHM) of the diffraction lines is usually represented by the Cagliotti et *al*. [1958] relationship:

- 3 $$HWHM^2 = H^2 = U \tan^2\theta + V \tan\theta + W$$

This form includes the one proposed by Khattak et Cox (1977) as a simplification in the case of X-ray diffraction diagrams. Note here that we should not confuse the FWHM (which is called sometimes "Halfwidth", particularly in pioneering works) and HWHM (Half Width at Half Maximum) the half of the former.

The g(x) function is experimentally accessible by measuring a standard powder sample. An example of instrumental resolution function is shown in Figure 4, for the D1B neutron instrument of the ILL-Grenoble and for the x-ray instrument of CRISMAT-Caen. Neutron resolution curve has been measured on a Belemnite rostrum having large calcite grains while the x-ray curve was measured using the standard SRM 660 LaB_6 powder from NIST shape as a flat specimen (ω = 11.5°).

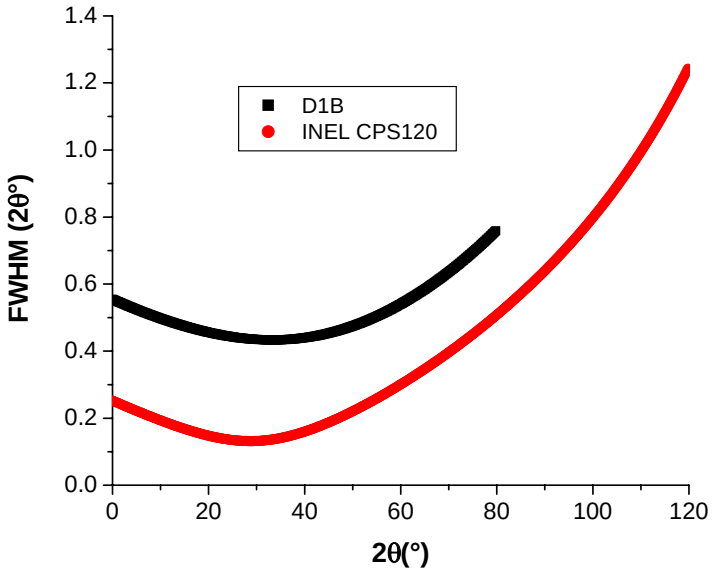

Figure 4: Instrument resolution curves for a neutron (D1B-ILL, calcite rostrum sample) and a x-ray (CRISMAT, LaB_6 standard powder) diffractometer set-up

1.5.2 Origin of f(x)

Using enough resolved diffractometers one can observe the deviation of h(x) from g(x) due to sample microstructure. The line broadening increase comes essentially from the two following effects:

i) broadening due to the finite size of the crystallites. Small crystallites give rise to diffraction lines that are no longer Dirac-like but have widths and shapes depending on the mean particle sizes and shapes in the **h** direction. The simplest analysis of such broadening gives [Scherrer 1918]:

- 4
$$\Delta(2\theta) = \frac{K\lambda}{T\cos\theta}$$

in which T is the mean thickness of the diffracting crystallites for the **h** direction selected by θ, and K is the Scherrer dimensionless constant, close to unity, which depends on the crystallite shape.

ii) broadening due to crystallite microdistortions. This broadening is defined by the crystalline non-uniform variations of $d_{hk\ell}$, which can be produced by external stresses, crystalline defects (dislocations for instance) or local compositional variations (in solid solutions for instance). One can show that:

- 5
$$\Delta(2\theta) = 4\,\varepsilon\,\tan\theta$$

where ε is the relative deformation of the interreticular distance: $\varepsilon = \Delta d_{hk\ell} / d_{hk\ell}$.

This broadening variation with θ is larger than for finite crystalline sizes.

Of course microdistortions and size effects can be present simultaneously in the same sample. Their measurement, for instance to determine the anisotropic shape of the crystallites from diffraction, is not every time easy and various more or less complex methods have been proposed [Warren 1969, Klug & Alexander 1974]. Some of them will be described in the corresponding microstructural analysis paragraph.

1.6 Peak profile Parameters

The parameters used to define the peak profiles are:

i) positions of the individual contributions
ii) their angular or energetic dispersions (FWHM)
iii) their surface under profile (intensity)
iiii) their shape.

Other parameters are sometimes used like the barycenter of the profile:

- 6

$$\langle 2\theta \rangle = \frac{\int 2\theta\, I(2\theta)\, d(2\theta)}{\int I(2\theta)\, d(2\theta)}$$

These parameters play a rule in the identification of solid substances, pattern indexing … It is then of prior importance to operate to a careful calibration of the instrument to avoid as much as possible systematic errors. Also, some structural defects or states like stacking faults or residual stresses can shift the diffraction peaks, that have to be taken into account before any result can be given.

1.7 Modelling of the diffraction peaks

1.7.1 Why needing modelling ?

A central problem of powder diffraction is peak overlapping [Smith 1977, Smith 1989, Wagner 1966]. The increase in diffraction peak density with 2θ results in strong peak overlaps, particularly for low crystal symmetries and low instrumental resolutions. This gives rise to a rapidly increasing jamming of the information at large 2θs, and to non usable diagram. The 2θ limit value above which the diagram becomes unusable is never strictly defined and often prevents a careful determination of the needed information. The overlapping problem imposes the optimisation of both the instrument resolution and the mathematical/computer treatment in order to obtain the best possible Bragg components.

When several physical phenomena are visible in the diagram, their relative contributions cannot be extracted without modelling of the convolution effects. Any deconvolution should be carried out with prior knowledge of the way they affect the profiles.

1.7.2 Modeling of a powder diffraction pattern

Depending on the seek information and on the *a priori* knowledge of the material, one can use one of the two methodologies hereafter, or the Rietveld approach (next paragraph).

1.7.2.1 Decomposition of the diagram (individual adjustment of the peaks)

The principle of this method, called direct integration, is to adjust an analytical function on each of the peaks of the pattern, provided the individual contributions do not overlap too much. This method is used when the desired crystallographic information is linked to the peak positions, intensities and/or shape of a limited number of peaks, and we do not need the full diagram. In this approach the diagram can be divided in several, individually treated parts. Any common software with peak profile refinements can be used in this approach. The approximate positions and widths of the peaks are in general firstly visually intuited from a graphic interface, then adjusted by a least-square refinement procedure, by minimising the residual M:

- 7

$$M = \sum_i \frac{1}{y_{ic}} (y_{io} - y_{ic})^2$$

where y_{io} and y_{ic} are the observed and calculated intensities at point i respectively, which describe the considered peak. The only imposed constraint in this method lies in the choice of the mathematical function used to describe the individual profiles. For this it exists a full set of used functions that will be detailed in following paragraphs. The simplest are the Gaussian and Lorentzian functions [Snyder 1983, Suorti 1995]. For some reasons the most used functions in crystallography are Voigt [Langford 1992] and Pseudo-Voigt.

Lets note that we find such functions also in the description and refinement of other physical measurements, for instance in spectroscopy (Raman, Nuclear Magnetic Resonance, Mössbauer ...). The important thing is to give a physical meaning to the parameters of the mathematical function used to describe the observations.

The efficiency of this methodology is rapidly limited by the overlap of neighbouring peaks. This limitation can be partially bypassed by imposing some constraints on the refined parameters of the lines: this is for instance the case when all the lines are imposed with the same shape and FWHM evolution with θ.

A refinement example using this approach to fit a five components pattern is shown in Figure 5.

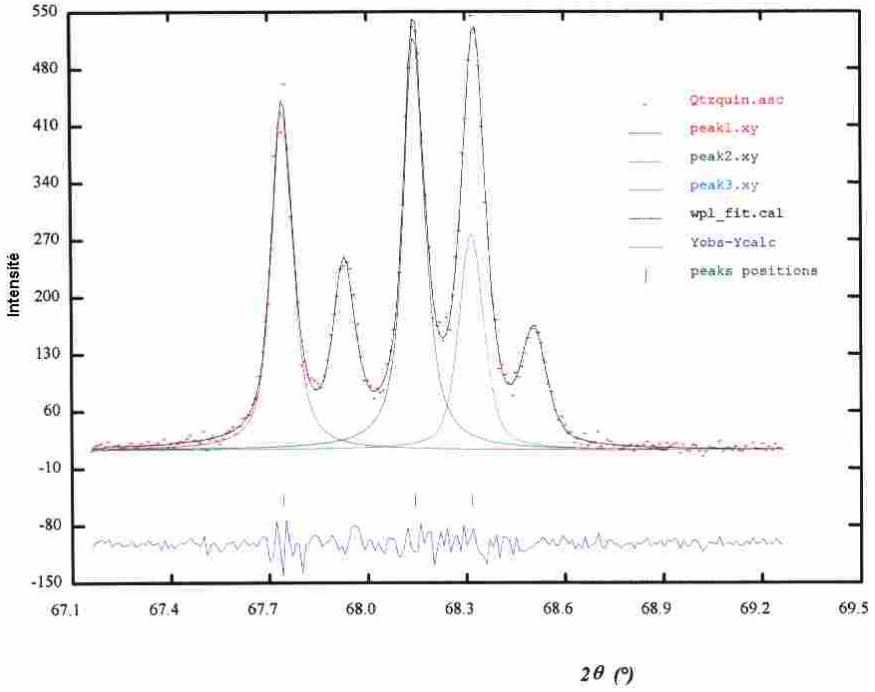

Figure 5: Least-squares result on a quartz powder

1.7.2.2 Profile refnement with cell constraint (*Whole pattern fitting*)

In this approach the full diffraction pattern is analysed without a structural model but constraining the unit-cell [Toraya 1986]. The peak positions are linked to the unit-cell parameters but their intensities is not taking account of the structure and are adjusted simultaneously with the other parameters of the profiles. The dependency of the peak widths

is described by the Cagliotti relation (Eq. - 3) [Cagliotti et al. 1958] or some related approaches [Prince 1989, Cheary et Cline 1994].

The observed intensity y_{io} at each step i of the profile is modelled by a calculated intensity y_{ic}:

- 8
$$y_{ic} = y_{ib} + \sum_k I_k \Omega_{ik}$$

where y_{ib} is the background intensity at step i.
$\Omega_{ik} = \Omega(2\theta_i - 2\theta_k)$ is the profile shape function of the k^{th} peak at $2\theta_k$.
I_k is the integrated intensity of the k^{th} peak of the diagram contributing to step i.

This method was originally proposed by Pawley [1981]. In the procedure, all the possible reflections are first generated from the approximate unit-cell parameters (and space group if known for systematic extinction's). Then the corresponding integrated intensities are refined by a least-square approach together with the line profiles and unit-cell. Since there is no constraint on the intensities via the structure, convergence of this approach is however relatively unstable, but provides important information for unknown structures. Figure 6 shows an example of a Whole Pattern Fitting of an anatase/rutile mixture, operated with the Fullprof software [Rodriguez 2003].

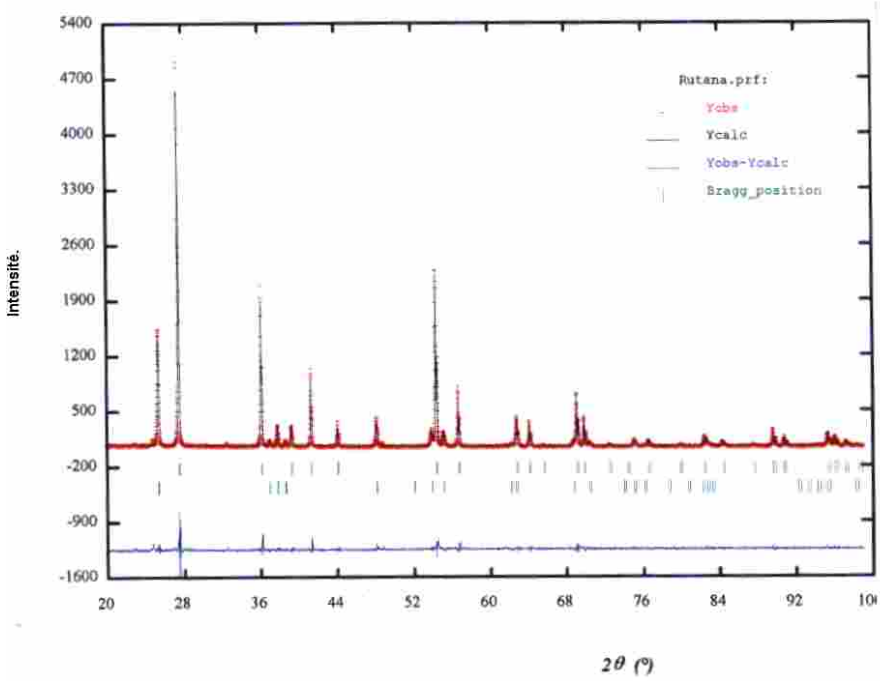

Figure 6: Refinement of an anatase/rutile powder operated by Whole Pattern Fitting using Fullprof

1.7.2.3. Functions describing the peak shape

1.7.2.3.1. Gaussian

- 9

$$G(2\theta_i) = \frac{2I_0\sqrt{\ln 2}}{H_k\sqrt{\pi}} \exp\left(\frac{-4\ln 2(2\theta_i - 2\theta_k)^2}{{H_k}^2}\right)$$

Where: $$H_k = \sqrt{U\tan^2\theta_k + V\tan\theta_k + W + P/\cos^2\theta_k}$$

I_0 is the integrated intensity.
$2\theta_i$ is the two theta value of each profile point i.
$2\theta_k$ is the expected two theta value for each reflection k.
H_k is the FWHM for each reflection k.
U, V, W and P are the resolution function parameters of the diffractometer.

Refinable parameters: U, V, W, P

1.7.2.3.2. Lorentzian and Modified Lorentzian (Pearson VII)

- 10

$$L(2\theta_i) = \frac{I_0\sqrt{C}}{\pi H_k}\left(\frac{1}{1 + C\left(\frac{2\theta_i - 2\theta_k}{H_k}\right)^2}\right)^m$$

with $$C = 4\left(2^{1/m} - 1\right)$$

m is the Lorentzian order which varies between 0 and infinity.
m = 1 gives the "pure" Lorentzian function.
m = 1.5 gives the "intermediate" Lorentzian function [Malmros et Thomas 1977].
m = 2.0 gives the "modified" Lorentzian function [Sonneveld et Visser 1975].

Refinable parameters: U, V, W, P, m

1.7.2.3.3. Voigt

- 11

$$V(2\theta_i) = L(2\theta_i) \otimes G(2\theta_i)$$

Refinable parameters: U, V, W, P, m

1.7.2.3.4. Pseudo-Voigt

- 12

$$PV(2\theta_i) = \eta L(2\theta_i) + (1-\eta)G(2\theta_i)$$

η is the mixing parameter of the linear combination which varies between 0 and 1.
$L(2\theta_i)$ is the pure Lorentzian function and $G(2\theta_i)$ the pure Gaussian function.

Refinable parameters: U, V, W, P, n

1.7.2.3.5. Split Pearson VII [Toraya 1986]

- 13
$$PVII(2\theta_i) = \frac{Q}{H_k}\left(L_0\left[1+\left(\frac{1+As}{As} \right)^2 C_1\left(\frac{2\theta_i - 2\theta_k}{H_k} \right)^2 \right] \right)^{-1}$$

for $2\theta_i \le 2\theta_k$

- 14
$$PVII(2\theta_i) = \frac{Q}{H_k}\left(H_0\left[1+(1+As)^2 C_2\left(\frac{2\theta_i - 2\theta_k}{H_k} \right)^2 \right] \right)^{-1}$$

for $2\theta_i > 2\theta_k$

with $C_1 = 2^{1/L_0} - 1$ and $C_2 = 2^{1/H_0} - 1$

$$As(\theta_k) = As(1) + As(2)/\sin\theta_k + As(3)/\sin^2\theta_k$$
$$L_0(\theta_k) = L_0(1) + L_0(2)/\sin\theta_k + L_0(3)/\sin^2\theta_k$$
$$H_0(\theta_k) = H_0(1) + H_0(2)/\sin\theta_k + H_0(3)/\sin^2\theta_k$$

Q is a function of As, L_o and H_o.

Refinable parameters: U, V, W, P, As(1–3), Lo(1–3), Ho(1–3)

1.7.2.3.6. Variable pseudo-Voigt

- 15
$$PV(2\theta_i) = \eta_V L(2\theta_i) + (1-\eta_V)G(2\theta_i)$$

$$\eta_V(\theta_k) = p(1)\tan^2\theta_k + p(2)\tan\theta_k + p(3)$$

Refinable parameters: U, V, W, P, p(1–3)

1.7.2.3.7. Parameterised pseudo-Voigt [Thompson et al. 1987]

- 16
$$PV_P(2\theta_i) = \eta_P L(2\theta_i) + (1-\eta_P)G(2\theta_i)$$

$$\eta_P = 1.36603(Y_L/Y) - 0.47719(Y_L/Y)^2 + 0.11116(Y_L/Y)^3$$
$$Y = \left[Y_G{}^5 + 2.69269 Y_L Y_G{}^4 + 2.42843 Y_L{}^2 Y_G{}^3 + 4.47163 Y_L{}^3 Y_G{}^2 + 0.07842 Y_L{}^4 Y_G + Y_L{}^5 \right]^{1/5}$$

Gaussian part $Y_G(\theta_k) = \sqrt{U\tan^2\theta_k + V\tan\theta_k + W + P/\cos^2\theta_k}$

Lorentzian part $Y_L(\theta_k) = X\tan\theta_k + Y/\cos\theta_k + Z$

Refinable parameters: U, V, W, P, X, Y, Z

1.7.2.3.8. Anisotropic variable pseudo-Voigt [Le Bail et Jouanneaux 1997]

- 17 $$PV_A(2\theta_i) = \eta_A L(2\theta_i) + (1-\eta_A)G(2\theta_i)$$

- 18 $$H_k = \sqrt{U_{hk\ell}\tan^2\theta_k + V_{hk\ell}\tan\theta_k + W_{hk\ell}}$$

$$\eta_A(\theta_k) = pU_{hk\ell}\tan^2\theta_k + pV_{hk\ell}\tan\theta_k + pW_{hk\ell}$$

- 19

$$U_{hk\ell} = d_{hk\ell}{}^2 (U_{11}h^2a^{*2} + U_{22}k^2b^{*2} + U_{33}\ell^2c^{*2} + 2U_{12}hka^*b^* + 2U_{13}h\ell a^*c^* + 2U_{23}k\ell b^*c^*)$$

and similar expressions as Eq. - 19 for $V_{hk\ell}, W_{hk\ell}, pU_{hk\ell}, pV_{hk\ell}, pW_{hk\ell}$

Refinable parameters: U_{11}, U_{22}, U_{33}, U_{12}, U_{13}, U_{23}
and V_{ij}'s, W_{ij}'s, pU_{ij}'s, pV_{ij}'s, pW_{ij}'s.

Meaning 36 parameters to fit. This procedure is actually not linked to the Popa-like parameters for microstructure.

1.7.2.3.9. Anisotropic variable Pearson VII [Le Bail et Jouanneaux 1997]

The function is defined as in Eq. - 13 and - 14 with H_k given by Eq. - 18 and m is a function of hkℓ:

- 20 $$m_{hk\ell}(\theta_k) = pU_{hk\ell}\tan^2\theta_k + pV_{hk\ell}\tan\theta_k + pW_{hk\ell}$$

Refinable parameters: U_{11}, U_{22}, U_{33}, U_{12}, U_{13}, U_{23}
and V_{ij}'s, W_{ij}'s, pU_{ij}'s, pV_{ij}'s, pW_{ij}'s.

Meaning 36 parameters to fit. This procedure is actually not linked to the Popa-like parameters for microstructure.

1.7.2.3.10. Anisotropic parameterised pseudo-Voigt [Stephens 1999]

This function is derived from the Thompson, Cox et Hastings parameterised pseudo–Voigt.

- 21 $$PV_P(2\theta_i) = \eta_P L(2\theta_i) + (1-\eta_P)G(2\theta_i)$$

$$\eta_P = 1.36603(Y_L/Y) - 0.47719(Y_L/Y)^2 + 0.11116(Y_L/Y)^3$$

$$Y = \left[Y_G^{\,5} + 2.69269 Y_L Y_G^{\,4} + 2.42843 Y_L^{\,2} Y_G^{\,3} + 4.47163 Y_L^{\,3} Y_G^{\,2} + 0.07842 Y_L^{\,4} Y_G + Y_L^{\,5}\right]^{1/5}$$

But the Gaussian and Lorentzian parts change to:

Gaussian part $$Y_G(\theta_k) = \sqrt{U\tan^2\theta_k + V\tan\theta_k + W + (1-\xi)^2\Gamma_A^2(hkl)}$$

Lorentzian part $$Y_L(\theta_k) = X\tan\theta_k + Y/\cos\theta_k + \xi\Gamma_A(hkl)$$

The anisotropic contribution is included in the $\Gamma_A(\mathrm{hkl})$ expression:

$$\Gamma_A(hkl) = \sqrt{\sigma^2(M_{hkl})}\tan\theta_k / M_{hkl}$$

Where $\sigma^2(\mathrm{M_{hkl}})$ is the variance of $\mathrm{M_{hkl}} = 1/\mathrm{d}^2_{\mathrm{hkl}}$

$$\sigma^2(M_{hkl}) = \sum_{HKL} S_{HKL} h^H k^K l^L \qquad \text{with H+K+L = 4}$$

Refinable parameters: U, V, W, X, Y, ξ

1.8 Experimental geometry

As far as combined analysis is of concerns, the acquisition of many diagrams may be required, particularly if texture analysis is of importance. Using point detectors consequently gives rise to prohibitive acquisition times. These experimental times can be reduced by the use of unidimentional (linear or curved) or bidimensional (CCD camera or image plates) detectors. Using the formers can economise a scan (generally along the 2θ rotation for diffraction experiments, or along another for diffusion experiments) while the latter, depending on the geometry, allows to work with even one less rotation. In any case it is useful to hold these detectors on monitored arms that allow a precise positioning which allow misorientations to be corrected. Working with 4 (or more) circles diffractometer is then preferred.

1.8.1. Curved Position Sensitive detector, asymmetric reflection geometry

Figure 7 illustrates the mounting of a CPS detector on a 4-circles diffractometer with the different angular variables and frames. The arrows rotation arrows indicate the + sign for each rotation. The sample reference frame K_A and the spectrometer reference frame K_S are indicated. One can see on this figure the following rotations:

- ω: the incidence angle of rays, rotation around Z_S
- χ: the co-latitude or pole distance, rotation around the Eulerian cradle axis, intersection between sample and scattering planes
- φ: the azimuth angle, rotation around the sample normal Z_A

- τ: detector position relative to Z_S
- 2θ: signal position (diffracted or scattered) from the incident beam in the scattering plane

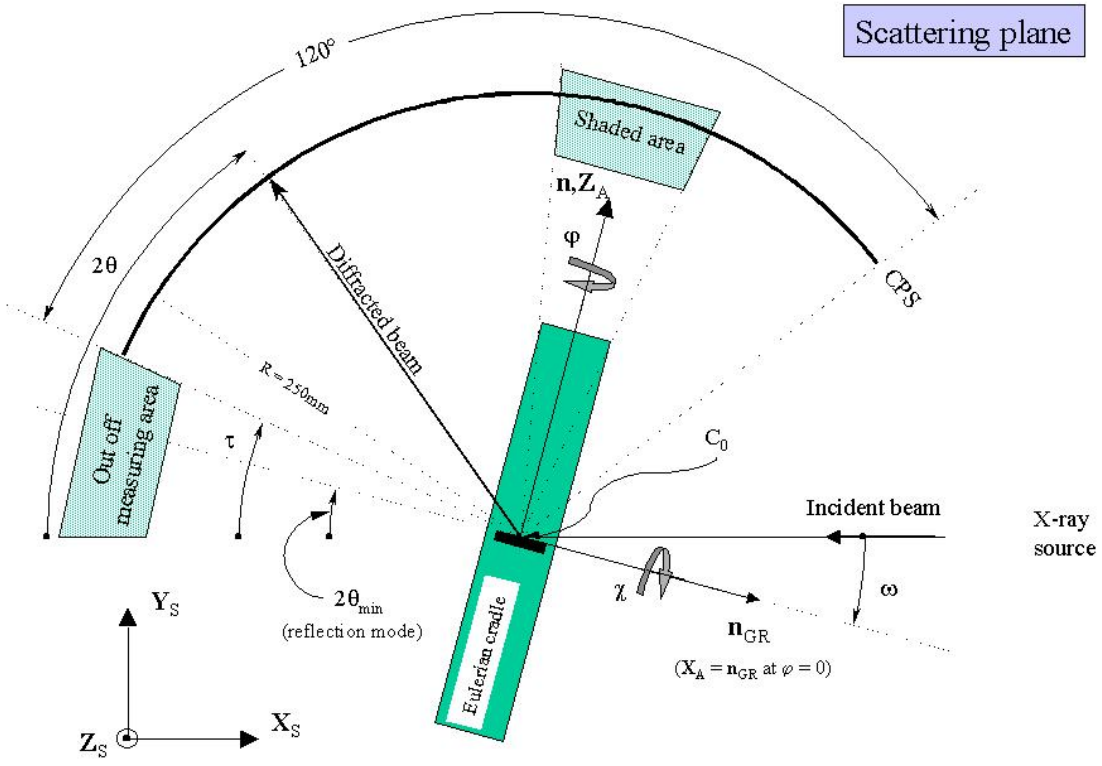

Figure 7: 4-circles reflection Geometry using a CPS detector

Depending on the Eulerian cradle (opened or closed circle), a dead-area can be present due to shading of the signal by absorption through the cradle. Also, an out of measuring area is present in reflection geometry due to absorption through the flat sample, which starts at ω.

1.8.2. CCD or image plate detector, asymmetric transmission geometry

In this instrumental set-up the ω angle is the same as the one of Figure 7, while ζ is a rotation perpendicular to the incident beam and the ω axis.

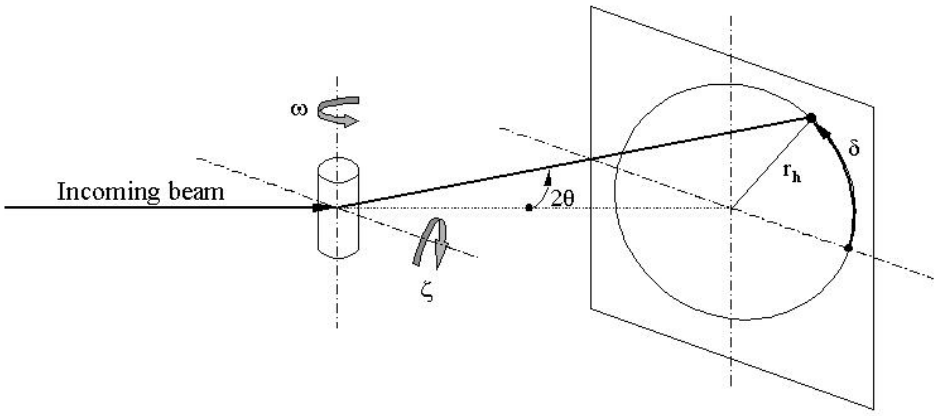

Figure 8: 4-circles transmission Geometry using a 2D detector

2 Structure refinement by diffraction profile adjustment (Rietveld method)

2.1 Principle

Another approach starts with roughly estimated integrated intensities I_k^0, in order to calculate new intensities at the cycle n+1, I_k^{n+1}, using the expression:

- 22
$$I_k^{n+1} = \sum_i I_k^n \Omega_{ik} \frac{y_{io} - y_{ib}(n)}{y_{ic}(n) - y_{ib}(n)}$$

where y_{ib} is the background associated to the i^{th} measured intensity y_{io}.

This method is numerically more stable and efficient than the Pawley approach, and has initially been proposed by Rietveld [1967]. Many other algorithms use it [Taylor 1985, Le Bail 1992, Rodriguez 2003] also. It is actually the most intensively used technique because of its efficiency in powder diffraction when the crystal structure of the sample is known. It has originally been developped for monochromatic neutron powder diffraction analysis, and has been extended to monochromatic x-ray experiments and modified to allow time of flight neutron and x-ray energy dispersive data analyses.

The Rietveld algorithm uses all the information of the experimental spectral range, including information outside the diffraction peaks. The used variables are:

- the instrumental characteristics (resolution curve of the diffractometer, displacement parameters concerning goniometer misadjustments, experimental geometry, detector characteristics ...)
- the structural parameters (unit-cell parameters, atomic positions, atomic occupations, thermal vibrations, ...)
- the microstructural parameters (mean crystallite sizes and microstrains, defects ...)
- the sample parameters (preferred orientations, residual stresses, excentricity, thicknesses, transparency, absorptions, phase fractions ...)

The refinement code minimises the following function:

- 23
$$M = \sum_i w_{io} (y_{io} - y_{ic})^2$$

where $w_{io} = \frac{1}{\sigma_{io}^2}$ is the statistical weight associated to the observed intensity y_{io} at the i^{th} measured point (σ_{io} is the variance associated to the observed y_{io}), and $y_i = y_{io} - y_{ib}$. During the refinement the used weights are $w_{io} = \frac{1}{y_{io}}$, while for a refinement using the maximum likelihood (Bernoulli 1861, Fisher 1922) they are $w_{ic} = \frac{1}{y_{ic}}$. Relation - 23 implies that the measurements are independent and that the variations of the observations obey a normal

frequency distribution. The second weighting scheme is then preferred for diagrams with low counting levels where normal distributions are not satisfied.

The sum extends to all the measured points of the pattern. Calculated intensities are determined by adding the contributions of all the peaks for all N_Φ phases of the sample, which superimpose with the background contribution at each point i:

- 24

$$y_{ic} = y_{ib} + \sum_{\Phi=1}^{N_\Phi} S_\Phi \sum_{k=K_1}^{K} j_{\Phi k} Lp_{\Phi k} P_{\Phi k} \left|F_{\Phi k}\right|^2 \Omega_{i\Phi k}$$

in which:

- S_Φ is a scale factor, proportional to the volumic fraction of each refined phase Φ
- $j_{\Phi k}$ is the multiplicity factor of the peak for phase Φ
- $Lp_{\Phi k}$ is the Lorentz-polarisation factor
- $P_{\Phi k}$ is a correction factor describing preferred orientations of phase Φ
- $|F_{\Phi k}|$ is the modulus of the structure factor (including thermal agitation) of phase Φ
- $\Omega_{i\Phi k}$ describes the profile function of the peaks of phase Φ, which represents instrumental and potential sample broadenings.

The first sum runs for all the phases in the sample and the second for all the reflections k which contribute to the i^{th} measured point. As the feet of the function $\Omega_{i\Phi k}$ are often rapidly decreasing, the calculation of the contribution of a given reflection k at the angle $2\theta_i$ is necessary only in a limited range on each side of the peak barycenter. For a Gaussian shape, this range is typically of 1.5 times the FWHM of the peak. However, this value may be increased (sometimes up to 20 FWHMs) for profiles comprising Lorentzian contributions.

2.2 Rietveld based codes

The original program of 1969 [Rietveld 1969], is written for monochromatic neutron powder diffraction analysis and has been widely distributed by the author. Since then the programs and algorithms have been ameliorated by many authors. Some landmarks should be cited. The development by Von Dreele et *al*. [1982] carried out in order to analyse time of flight neutron data. The former uses have been extended to x-ray powder diffraction data around the late 70's [Malmros et Thomas 1977, Katack et Cox 1977]. A large number became available since then, most of them being capable to manage both x-ray and neutron data, and sometimes simultaneously. Most of them allow refinements with more or less complex refinement constraint systems [Pawley et *al.* 1977, Wiles et Young 1981, Bearlocher 1993, Lutterotti et al. 1999, WinMProf Jouanneaux 1999, Von Dreele 2002, Rodriguez 2003]. Refinement of many phases simultaneously is now accepted by quite all the softwares. Some of them allow magnetic struture refinements like Fullprof [Rodriguez 2003], and/or modulated strutures like Jana [Dusek 2001]. The MAUD program by Lutterotti et al. [1999] allows the combination of many different approaches (texture, stress, structure ...) and experimental configurations. Most of these programs in their actual versions allow visual interfacing and easy handling of most functionalities. It exists a tremendous number of programs that use the Rietveld method and it would be fastidious to describe their characteristics and specificities her. The Cransvick [1999] site is a place where to find practically all the existing programs used in crystallography in general.

2.3 Parameters modelling

2.3.1 Background modelling

The background at the i^{th} measurement can be modelled using two main different approaches, depending if one can place a physical explanation to the background signal.

2.3.1.1. Empirical approaches

In the empirical approach, an array of data given by the user can be selected and interpolated, or all the points used and fitted in the program. The interpolation or fit is operated through polynomial or Fourier series analytical functions [Richardson 1993].

2.3.1.1.1. m^{th} order polynomial function

A phenomenological function, used in absence of any better model, is a polynomia of order m which the origin Bkpos is specified. We can also add Gaussian functions to the background in order to better represent it, for instance to model the direct beam influence at low angles or to shape bumps coming from amorphous phases at a first approach or if these latter are not interesting. The function used is:

- 25
$$y_{ib} = \sum_{g=1}^{G} G_{ig} + \sum_{m=0}^{M} B_m [(2\theta_i / Bkpos) - 1]^m$$

where G and M are the total number of Gaussians and the order of the polynomia respectively.
y_{ib} is the calculated background at each point (i).
$2\theta_i$ and bkpos are in degrees.

2.3.1.1.2. Fourier series

- 26
$$B(i) = BK_0 + BK_1 \cos 2\theta_i + ... + BK_{11} \cos(11 * 2\theta_i)$$

Refinable parameters: BK_j (j=0 .. 11)

2.3.1.1.3. 2D detectors

Unlike 2θ diagrams, the background measured on CCD or image plate detectors may vary with 2 degrees of freedom. The radial variation from the centre (intercept of the incident beam) of the detector corresponds to the variation in 2θ and as such can be treated using Eqs. - 25 and - 26. If the background in not homogeneous in azimuth δ, then this variation has to be taken into account:

- 27 $$y_{ib\delta} = \sum_{g=1}^{G} G_{ig} + \sum_{m=0}^{M}\sum_{n=0}^{N} B_{mn}[(2\theta_i / Bkpos) - 1]^m \delta^n$$

with n an index running for all the measured points in δ. Note that since Gaussian contributions are generally axially symmetric around the incident beam, the background does not depend on δ in the previous equation. It would however not be a problem to include such variation.

2.3.1.2. Physical approaches

During the refinement of y_{ib}, a phenomenological function can be used when a known function describes the physical reality: amorphous phase scattering (taking account of a radial distribution function), thermal scattering … [Riello et al. 1995, Riello et al. 1995a].

2.3.2 Structure factor

The structure factor is given by [Eberhardt 1976]:

- 28 $$F_{\mathbf{k}} = \sum_j N_j f_j \exp(2\pi i[hx_j + ky_j + \ell z_j]) \exp(-M_j)$$

with:
- *h*, *k*, *ℓ*: Miller indices
- x_j, y_j, z_j: atomic positions of the atom *j* in the unit-cell
- f_j: atomic scattering factor for atom j

The X–ray scattering factor is defined as:

- 29 $$f_j (\sin\theta/\lambda) = f_0 + f' + if''$$

where f_0 is the normal atomic scattering factor, f' and f'' are the real and imaginary dispersion terms respectively which account for the anomalous scattering.
The f_0 values may alternately be calculated using the formula:

- 30 $$f_0(\sin\theta/\lambda) = \sum_{i=1}^{4} \left[a_i \exp\left(-b_i(\sin\theta/\lambda)^2\right)\right] + c$$

The nine coefficients a_i, b_i, i = 1 to 4 and c can be retrieved by the programs simply by supplying the atom name (neutral atoms and ions, *e.g.* Sr^{2+}, O^{2-} etc.).

- N_j: occupation ratio of site j
- $\exp(-M_j)$: thermal vibration parameter

Here are the atomic parameters which may be specified:

1) The Atomic Scattering Factor which may include both nuclear and magnetic scattering for neutron diffraction, or real and anomalous scattering for X–ray diffraction.

2) The Site Occupation Factor, which may reflect genuine defects in the occupancy of a particular atomic site, or, more usually, is employed to produce correct structure factor contributions from atoms situated on crystallographic symmetry elements.

3) The Coordinates within the unit cell expressed relative to the possibly non−orthogonal unit cell axes in terms of fractions of the unit cell edge.

4) The Thermal vibration parameters, which may describe either isotropic or anisotropic vibration. The isotropic temperature correction to the calculated structure factor is:

5)

- 31
$$\exp\left[-B(\sin\theta/\lambda)^2\right]$$

where B is the temperature factor expressed in $Å^2$. It then is the mean quadratic displacement of the atom. The anisotropic correction for reflection (hkℓ) is:

- 32
$$\exp-\left[h^2\beta_{11}+h^2\beta_{22}+\ell^2\beta_{33}+2hk\beta_{12}+2h\ell\beta_{13}+2k\ell\beta_{23}\right]$$

where β_{11} to β_{23} are the unique elements of the symmetric tensor describing the thermal vibration ellipsoid.

5) The components of the magnetic vector along each of the unit cell axes. If these parameters are supplied, additional symmetry information is required in order to determine the direction of the magnetic vector for each of the magnetic atoms in the unit cell. The calculation of the magnetic scattering cross section may be greatly simplified if the structure possesses either uniaxial or cubic spin configurational symmetry [Shirane 1959].

2.3.3 Crystallites Preferred Orientation (texture)

The correction of preferred orientations has to be taken into account as soon as the crystallites are likely to orient in one or several directions of the sample. Texture is particularly present in easy-clivage materials or having anisotropic growing, and when the samples are elaborated by anisotropic techniques. For instance NaCl crystallises as parallelepipedic crystallites limited by (001) planes which tend to orient parralel to the sample surface when compacting it for measurement purposes. In Bragg-Brentano geometry, the corresponding intensities will be favoured.

One should not confuse the texture effect and the lack in statistics in terms of number of irradiated crystallites, which both reinforce some peaks. In the latter case, reinforcements appear more or less stochastically, while in the former all the hkℓ, 2h2k2ℓ, 3h3k3ℓ, ..., are reinforced (if hkℓ is the textured direction).

It exists two types of texture treatments in Rietveld analysis. If the texture is simple (high symmetry and regular dispersion), it can be modelled by a classical analytical shape (Gaussian ...). If it is more complex (several texture components, non regular distributions ...) the treatment requires a quantitative texture analysis, matter of §5. In this paragraph only the simplest textures are of concerns.

The texture can be roughly modelled using three parameters:

- a texturation axis linked to the sample symmetry (the normal to the sample surface for a flat sample in Bragg-Brentano geometry, the cylinder axis in Debye-Scherrer geometry)
- the crystallographic direction **h** which tends to align with the previous axis
- a texturation strength (angular dispersion, texturation factor ...).

2.3.3.1. Original Rietveld and March approaches

The preferred orientations are modelled in the original equation of Rietveld by the March approach [1992] using the function $P_{\mathbf{h}}$:

- 33
$$P_{\mathbf{h}} = \exp\left(-G_1\alpha_{\mathbf{h}}^2\right)$$

or

- 34
$$P_{\mathbf{h}} = G_2 + (1-G_1)\exp(-G_1\alpha_{\mathbf{h}}^2)$$

with G_1 and G_2 refinable parameters and $\alpha_{\mathbf{h}}$ the angle between the texture direction **h** and the scattering vector $\Delta\mathbf{k}$.

2.3.3.2 March–Dollase approach

Dollase shown that the following function is more efficient [Dollase 1986, Bowman et Mendendorp 1994]:

- 35
$$P_{\mathbf{h}} = (G_1^2\cos^2\alpha_{\mathbf{h}} + \left(\frac{1}{G_1}\right)\sin^2\alpha_{\mathbf{h}})^{-3/2}$$

where α is the acute angle between the scattering vector and the preferred orientation axis. Originally, the correction assumed a Gaussian distribution of the preferred orientation axis of the individual crystallites about the normal to the plane of the sample. G_1 is the refinable parameter ($G_1 = 1$: no preferred orientation) that now controls the distribution shape and is an index of the preferred orientation strength ($G_1 = 1$ for a random orientation).

This model provides:

- a preferred orientation correction factor which minimum or maximum at $\alpha = 0°$
- a symmetric and smooth evolution in the [0,90°] α range
- a single parameter to be fitted
- the possibility of normalisation of the orientation:

- 36
$$\int_0^{\frac{\pi}{2}} P_{\mathbf{h}}\, d\alpha = 1$$

This latter property is important in order to keep constant the total diffracted intensity in a diffraction diagram whatever the distribution shape $P_{\mathbf{h}}$.

However, this type of formulation is only valid for axially distributed, single component, textures (with a cylindrical symmetry around the scattering vector, and for a Bragg-Brentano geometry), for which it has proved to provide efficient corrections [O'Connor et al. 1991, Capkova 1993, Cerny 1995]. It is implemented in many softwares, and some of them allow a two texture components of this type. For all the other textures, measurements

and formalisms to resolve the texture are more complex and have to be envisaged, unless a destruction of the sample is acceptable, as has been demonstrated for instance by O'Connor et al. (1992).

2.3.3.3 Donnet–Jouanneaux function

This model for correcting preferred orientations is purely empirical.

- 37
$$P_h = 1 + \frac{D.\cos 2\alpha}{1 + (G-1)\sin^2 \alpha}$$

Refinable parameters: G, D (D = 0: no preferred orientation)

By no way the Mach-Dollase or Donnet-Jouanneaux models allow the descriptions of textures in terms of distribution densities. These descriptions are then depending on sample dependent factors like porosity, crystalline state ...

2.3.4 Peak asymmetry

It is often observed that the diffraction peaks exhibit some asymmetry, particularly at low Bragg angles in Bragg-Brentano configuration. This effect can come from the convolution of the goniometer slit shapes by the sample signal. Geometrically, the intersection between a linear detecting slit and a Debye-Scherrer cone of half-aperture α introduce distortions of the peak shapes, which are most detectable at low and high angles. Such an effect can be corrected during the refinement by multiplying y_{io} by an asymmetric factor of various shapes, among which the most used ones are the following.

2.3.4.1 Rietveld's correction [Rietveld 1969]:

- 38
$$A(2\theta_i - 2\theta_h) = 1 - A\, sign(2\theta_i - 2\theta_h).(2\theta_i - 2\theta_h)^2 / \tan\theta_h$$

A is the refined parameter and θ_k the line position (the inverse dependence in $\tan\theta_k$ is not always used). The asymmetry can be used for instance for an asymmetric Lorenztian (AL):

- 39
$$AL = A(2\theta_i - 2\theta_h)L$$

2.3.4.2 Howard's correction [Howard 1982]

The correction employs the Simpson's or Bode's integration rule and is applied in the form of a sum of n peaks, n being the number of integration ordinates. For instance, if a Pseudo-Voigt function is used, the corrected peak shape function (PSF) will be defined as:

- 40
$$\Omega_{ik}(2\theta_i) = \sum_{\ell=1}^{n} g_\ell \quad PV\left[2\theta_i - f_\ell(\alpha)P / \tan(2\theta_k)\right]$$

P is the asymmetry parameter (P = 0: no correction). The values of the Simpson's or Bode's rule coefficients, f_ℓ and g_ℓ, depend on the number of terms in the summation. $f_\ell(\alpha)$ is related to the ordinates positions; α is a refinable parameter which enables the positions not to be only equidistant. Depending on the program, the correction can be applied to some or other peak shape functions.

Refinable parameters: P, α.

2.3.4.3. Finger, Cox et Jephcoat's correction [Finger et al. 1994]

This correction is the most physically appropriate. It is expressed as a function of three parameters:

i) L, the sample to detector distance,
ii) 2H, the aperture of the detector slit and
iii) 2S, the beam size on the sample or alternately the sample size if the beam is larger.

For X–ray powder diffraction, 2H is the horizontal width of the detector slit and 2S is the horizontal beam size. For neutron diffraction, 2H is the vertical width of the slit and 2S is the vertical beam size.

Refinable parameters: the ratios S/L, H/L.

2.3.4.4 Bérar-Baldinozzi correction [Bérar et Baldinozzi 1993]

The asymmetry correction, which works well for weak asymmetries, takes the form:

- 41
$$1+\left[P_1+2P_2\left(2z^2-3\right)\right]\frac{F_a(z)}{\tan\theta_k}+\left[P_3+2P_4\left(2z^2-3\right)\right]\frac{F_a(z)}{\tan 2\theta_k}$$

where $z=\dfrac{2\theta_i-2\theta_k}{H_k}$ and $Fa(z)=2z\exp(-z^2)$.

Refinable parameters: P_1, P_2, P_3, P_4 (Pi = 0, i = 1,4: no assymetry)

2.3.4.5 TOF neutrons

The neutron pulse structure imposes an additional asymmetric broadening effect. Von Dreele et al. [1982] proposed an empirical form for this asymmetry, composing the peak shape function with back-to-back paired set of exponential convoluted with Gaussians:

- 42
$$\Omega_{ik}(\Delta T) = N\,[\exp(u)\,\mathrm{erfc}(x) + \exp(v)\,\mathrm{erfc}(y)]$$

The refinable parameters N, u, ν, x, y have various functional dependencies on the d-spacing of the reflection, the scattering angle of the detector and the structure of the neutron source. ΔT is the offset of the profile point from the reflection position.

2.3.5 Peak displacements

Diffraction diagrams can be affected by systematic errors coming either from the diffractometer or from the sample (bad adjustment of the instrument, incorrect sample positioning) [Wilson 1963]. Most often met aberrations of this kind are described here. They all induce peak displacements varying with the Bragg angle as a cosθ or sinθ law, with a coefficient depending of the diffractometer geometry and the nature of the aberration. Rietveld software allow the refinement of the factors composing these errors.

2.3.5.0 Zero-shift

If the detector is shifted relative to the incident beam, a constant shift $\Delta 2\theta_0$ appears for all peaks and has to be refined.

2.3.5.1 Debye-Scherrer geometry

- 43 $$\Delta 2\theta = a \cos\theta / R - b \sin 2\theta / R$$

Where a and b are sample displacements in the directions parallel with and perpendicular to the incident beam, respectively, and R is the sample to detector distance.

2.3.5.2 Flat plate, θ-2θ Bragg-Brentano symetrical geometry

- 44 $$\Delta 2\theta = -2 s \cos\theta / R$$

s is the sample displacement and R the radius of the goniometer circle.

2.3.5.3 Flat plate at fixed sample angle ω, asymetrical geometry

- 45 $$\Delta 2\theta = b \sin 2\theta / R \sin\omega$$

2.3.5.4 Flat plate transmission geometry

- 46 $$\Delta 2\theta = -a \sin(2\theta) / R$$

2.3.5.5 Sample excentricity (Bragg-Brentano geometry)

This is often the largest error source of peak positions. This error is given by [Matulis et Taylor, 1993]:

- 47 $$\Delta(2\theta) = -2sR^{-1}\cos\theta$$

s being the sample displacement relative to the goniometer axis in the **Δk** direction. The minus sign stands for peak shifts towards lower angle for displacements below the focalisation circle. The refined parameter is often the whole ($-2sR^{-1}$) factor.

2.3.5.6 Sample transparency

Transparency correction is operated through [Alexander 1948]:

- 48 $$\Delta(2\theta) = -(\mu R)^{-1}\sin\theta$$

in which μ is the linear absorption coefficient of the sample.

2.3.5.7 Sample planarity (Bragg-Brentano geometry)

In this geometry the sample surface is not concentric to the focalisation circle of the goniometer, but usually flat and tangent to this circle. It results an asymmetrical broadening of the line profile and a shift of its barycenter:

- 49 $$\Delta(2\theta) = -\frac{6}{\alpha^2}\cot an\theta$$

α is here the incident beam divergence.

2.3.6 Lorentz-polarisation correction

2.3.6.1. X-ray diffraction

2.3.6.1.1. Bragg-Brentano geometry

For powders and x-ray diffraction, the Lorentz factor is defined by:

- 50 $$L = \frac{1}{2\sin^2\theta\cos\theta}$$

For X–ray diffraction, the incident X–ray beam can be polarised or not. The form adopted in most programs for the polarisation factor p is:

- 51 $$P = 1 + \cos^2 2\theta_m \cos^2 2\theta$$

where $\cos^2 2\theta_m$ is the monochromator polarisation correction and θ_m the exit angle of the monochromator.

For an unpolarised incident beam on the sample (no front monochromator inserted), $\cos^2 2\theta_m = 1$. With a front or back monochromator set-up, the $\cos^2 2\theta_m$ value must be specified. For instance, with a graphite monochromator and Cu-Kα radiation, $\cos^2 2\theta_m = 0{,}7998$.

For synchrotron radiation when the beam is 100% polarised in the plane perpendicular to the incident and diffracted beams, $\cos^2 2\theta_m = 0$.

The Lp factor takes finally the following form [Langford 1986]:

- 52 $$Lp = [1 + \cos^2 2\theta_m \cos^2 2\theta] / 2 \sin^2 \theta \cos\theta$$

2.3.6.1.2. 2D detector and polarised beams

On a 2D detector using a polarised beam, the polarisation is not symmetrical around the incident beam (Figure 8), and the corresponding correction to be applied depends also on the running angle δ on the detector:

- 53 $$p = 1 - 0.5 \sin^2(2\theta) [1-p'\cos(2\delta)]$$

in which p' is the degree of polarisation of the primary beam. This latter can reach quite 100% using synchrotron radiation.

2.3.6.2. Time Of Flight neutrons

For neutrons, there is no polarisation but only the Lorentz factor, which for TOF neutron data takes the form [McCusker et al. 1999]:

- 54 $$L = d^4 \sin\theta$$

This factor strongly enhances the scattered intensity for large d-spacing reflections.

2.3.7 Volume, Absorption, thickness corrections

In many programs the volumic and absorption corrections may be applied for various experimental geometries. They depend also of the sample geometry, for instance thin films require specific correction and so on.

2.3.7.1. Schulz geometry, point detector, thin layered structure

Measuring textures requires to rotate the sample around two more axes than θ and 2θ [Schulz 1949a], called tilt χ and azimuth φ angles. Dealing with thin structures will then need an additional correction that compensates the volume and absorption variations when rotating the sample by χ. Using a point detector [Chateigner et al. 1992, Chateigner et al. 1994, Chateigner et al. 1994a], one can correct the observed intensities using:

Top Film:

- 55
$$y_i(0) = y_i(\chi)\frac{\left(1-\exp\left(-2\mu T/\sin\theta_i\right)\right)}{\left(1-\exp\left(-2\mu T/\sin\theta_i\cos\chi\right)\right)}$$

$y_i(\chi)$: profile intensity measured in the χ orientation at the i^{th} point of the profile
$y_i(0)$: corrected profile intensity like if measured at χ=0 at the i^{th} point of the profile
μ: linear absorption coefficient of the film
T: thickness of the film

Covered layer:

- 56
$$y_i(0) = y_i(\chi)\frac{\left(1-\exp\left(-2\mu T/\sin\theta_i\right)\right)\exp\left(\frac{-2\sum_j \mu_j T_j}{\sin\theta_i}\right)}{\left(1-\exp\left(-2\mu T/\sin\theta_i\cos\chi\right)\right)\exp\left(\frac{-2\sum_j \mu_j T_j}{\sin\theta_i\cos\chi}\right)}$$

μ: linear absorption coefficient of the considered layer of the stack
T: thickness of the considered layer of the stack
μ_j: linear absorption coefficient of the covering layers
T_j: thickness of the covering layers

Substrate:

- 57
$$y_i(0) = y_i(\chi)\frac{\exp\left(\frac{-2\sum_j \mu_j T_j}{\sin\theta_i}\right)}{\exp\left(\frac{-2\sum_j \mu_j T_j}{\sin\theta_i\cos\chi}\right)}$$

Multilayer:

- 58
$$y_i(0) = y_i(\chi)\frac{\left(1-\exp\left(-2\mu_\ell T_\ell/\sin\theta_i\right)\right)\exp\left(\frac{-2\sum_{j=1}^{\ell-1} \mu_j T_j}{\sin\theta_i}\right)}{\left(1-\exp\left(-2\mu_\ell T_\ell/\sin\theta_i\cos\chi\right)\right)\exp\left(\frac{-2\sum_{j=1}^{\ell-1} \mu_j T_j}{\sin\theta_i\cos\chi}\right)}$$

μ_ℓ: linear absorption coefficient of the considered layer of the stack
T_ℓ: thickness of the considered layer of the stack

2.3.7.2. Schulz geometry, CPS detector, thin layered structure

The use of a CPS detector on the previous 4-circle diffractometer implies different corrections have to be carried out, since the outcoming beam differs from peak position to

peak position. Considering an angle ω of incidence, the corrections to be applied are [Morales et al 2002]:

Top Film:

- 59
$$y_i(0) = y_i(\chi)\frac{\left(1-\exp\left(-2\mu TM(\omega,\theta_i)\right)\right)}{\left(1-\exp\left(-2\mu TM(\omega,\theta_i)/\cos\chi\right)\right)}$$

with

- 60
$$M(\omega,\theta_i) = \frac{1}{\sin\theta_i} + \frac{1}{\sin(2\omega-\theta_i)}$$

Covered layer:

- 61
$$y_i(0) = y_i(\chi)\frac{\left(1-\exp\left(-2\mu T M(\omega,\theta_i)\right)\right)\exp\left(-2M(\omega,\theta_i)\sum_j \mu_j T_j\right)}{\left(1-\exp\left(\frac{-2\mu T M(\omega,\theta_i)}{\cos\chi}\right)\right)\exp\left(\frac{-2M(\omega,\theta_i)\sum_j \mu_j T_j}{\cos\chi}\right)}$$

Substrate:

- 62
$$y_i(0) = y_i(\chi)\frac{\exp\left(-2M(\omega,\theta_i)\sum_j \mu_j T_j\right)}{\exp\left(\frac{-2M(\omega,\theta_i)\sum_j \mu_j T_j}{\cos\chi}\right)}$$

Multilayer:

- 63
$$y_i(0) = y_i(\chi)\frac{\left(1-\exp\left(-2\mu_\ell T_\ell M(\omega,\theta_i)\right)\right)\exp\left(-2M(\omega,\theta_i)\sum_{j=1}^{\ell-1} \mu_j T_j\right)}{\left(1-\exp\left(\frac{-2\mu_\ell T_\ell M(\omega,\theta_i)}{\cos\chi}\right)\right)\exp\left(\frac{-2M(\omega,\theta_i)\sum_{j=1}^{\ell-1} \mu_j T_j}{\cos\chi}\right)}$$

2.3.7.3. Transmission geometry, 2D detectors, flat sample

Using the set-up of Figure 8 and a platelet-shaped sample with the normal to the slab parallel to the incident beam in the $\omega = \zeta = 0°$ orientation, a correction has to be applied to account for absorption and volume changes for $\omega \neq 0°$ [Heidelbach et al. 1999]:

- 64
$$I(\omega) = I(0)\exp\left(-\mu T\left(\frac{1}{\cos\omega}-1\right)\right)$$
$$V(\omega) = V(0)/\cos\omega$$

where T is the sample thickness.

2.3.8. Localisation corrections

Localisation corrections are the ones that have to be operated on the angular co-ordinates of the data from the diffractometer space where the scattered intensities have been measured to the space in which modelling occurs, for instance the pole figure space $\mathcal{Y}$.

2.3.8.1. Schulz reflection geometry, CPS detector

In general using a CPS detector on a 4-circle diffractometer in the Schulz geometry, the (χ,φ) co-ordinates of the diffractometer space for which the diffracted intensities have been measured are not the ones of the $\mathcal{Y}$-space, except for that pole figure which have been measured exactly at the angle $2\theta = \omega$ (symmetric case) For all the other pole figures, the pole figure co-ordinates (φ_y,ϑ_y) have to be calculated [Matthies et Chateigner 2000]:

$$\vartheta_y = \arccos\{\cos(\theta - \omega)\cos\chi\}$$

$$\varphi_y = \varphi_y^0 - \varphi \qquad \textbf{- 65}$$

$$\varphi_y^0 = \mathrm{sign}\{-\cos(\theta - \omega)\sin\chi\}\arccos\{\sin(\theta - \omega)/\sin\vartheta_y\}$$

φ_y^0 is the φ value at 0.

These formulae are obviously depending on the geometry of the experiment, but also on the rotations signs. We placed our frames in the geometry of Figure 7, which differs somehow from the geometries used by other authors for the same calculations [Bunge et al. 1982, Heizmann et Laruelle 1986].

2.3.8.2. Transmission geometry, 2D detectors

Using the set-up of Figure 8, a given r_h Debye-Scherrer ring can be discretised in poles (say for instance every 5° along the ring) which have to be translated into co-ordinate of the pole figure space [Heidelbach et 1999] using:

$$\cos\vartheta_y = \mathrm{cosc}\sqrt{\left(1-\frac{\sin^2\theta\sin^2\delta}{1-\cos^2 c}\right)\left(1-\frac{\sin^2\varsigma\sin^2\delta}{1-\cos^2 c}\right)} - \frac{\sin\varsigma\sin\theta\sin^2\delta}{1-\cos^2 c}$$

$$\cos c = \cos\theta\cos\varsigma + \sin\theta\sin\varsigma\cos\delta \qquad \textbf{- 66}$$

$$\varphi_y = \omega + \arccos\left(\frac{\sin(\theta-\varsigma)}{\sin\vartheta_y}\right)$$

which, when the ζ rotation is not used simplifies:

$$\cos\vartheta_y = \cos c\sqrt{\left(1-\frac{\sin^2\theta\sin^2\delta}{1-\cos^2 c}\right)}$$

- 67

$$\cos c = \cos\theta$$

$$\varphi_y = \omega + \arccos\left(\frac{\sin\theta}{\sin\vartheta_y}\right)$$

Here also the rotations are of course oriented. Using neutrons or hard x-rays, these corrections are the only ones to achieve. However, if the sample shape differs from a regular cylinder, and/or for strongly absorbing samples, the ω and ζ rotations will give rise to absorption and irradiated volume changes which will need particular corrections.

2.3.9. Microabsorption/Roughness corrections

The microabsorption or surface roughness correction can apply on highly absorbing materials when systematic intensity decrease is detected at low angles. Four empirical formulations for this effect have been described in the literature. The surface roughness is introduced as a factor in the Rietveld refinement, S_R, that is large at low θ-values and takes the value 0 at θ = 90° (at normal incidence no roughness is "seen" by the incident beam). Such corrections have been implemented in the program by Young et al. (1999).

2.3.9.1. Sparks model, Bragg-Brentano

Sparks et al. (1992) use a monoparametric function for S_R:

- 68

$$S_R = 1 - t\left[\theta - \frac{\pi}{2}\right]$$

with t the parameter to refine and θ in radians.
This model is linear and does not satisfy corrections at very low θ angles (Figure 9).

2.3.9.2. Suortti model, Bragg-Brentano

Suortti (1972) uses a two-parameters function for SR, with the two parameters to refine p and q. This function can represent roughness effects even at low θ angles thanks to the additional parameter and the exponential variation:

- 69

$$S_R = 1 - p\exp(-q) + \mathrm{p}\exp\left(\frac{-\mathrm{q}}{\sin\theta}\right)$$

2.3.9.3. Pitschke model, Bragg-Brentano

Pitsche et al. (1993) also use two parameters to be refined, in the simplified function, which does not hold at very low θ's (Figure 9) because of the vertical asymptotic variation for θ = 0:

- 70

$$S_R = 1 - pq(1-q) - \frac{pq}{\sin\theta}\left[1 - \frac{q}{\sin\theta}\right]$$

2.3.9.4. Sidey model, Bragg-Brentano

In the two previous models, it exists a strong correlation between the two refinable parameters and the overall scale factor, atomic displacement parameters and site occupancies. In order to improve the refinement stability Sidey (2004) closely approximate the Pitschke and Suortti models using a monoparameter function:

- 71

$$S_R = \left(\frac{\theta}{\pi/2}\right)^{\frac{s}{\theta}} = \exp\left(\frac{s}{\theta}\ln\frac{\theta}{\pi/2}\right)$$

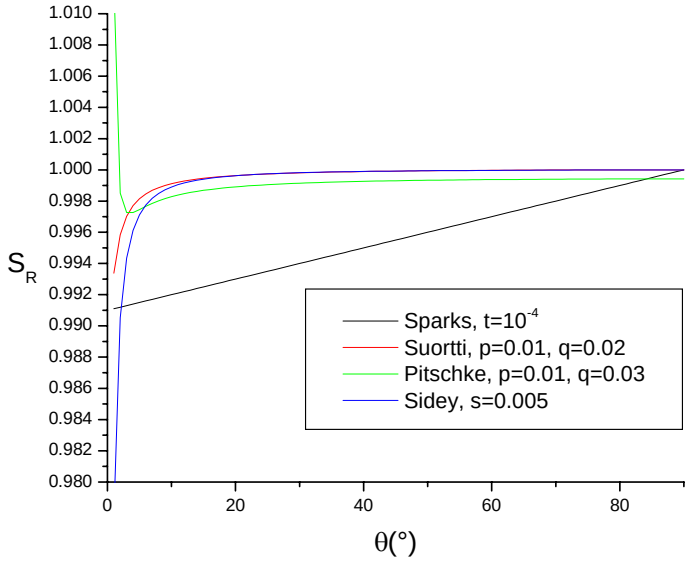

Figure 9: Model functions for surface roughness corrections from various authors. The parameters used in the models are not intended to fit the closest same solution.

2.3.10. Wavelength

Even in experiments carried out using a monochromatised radiation, the spectral distribution of the incident beam is never purely monochromatic. The spectral extension results in a peak broadening that has to be taken into account in the refinements. This broadening is calibrated inside the resolution curve of the diffractometer.

However, since most instruments are working with wavelengths issued for the K-edge emission of metals, the monochromator may also influence strongly the instrumental contribution to the peak shape. For instance, using a flat graphite monochromator, with usual crystallite mosaic of 0.4°, one will not be able to dissociate between the $K_{\alpha 1}$ and $K_{\alpha 2}$ lines of the radiation. Since these latter do not have the same intensity, and depending upon the actual adjustment of the monochromator, the real ratio between the two contributions will have to be determined. This is also done using a standard powder.

2.3.11. Microstructure modelling (classical)

In the expressions giving the width of the Gaussian and Lorentzian components of a Pseudo-Voigt profile, we find the terms varying as tanθ and cosθ. These two variations are respectively linked to broadening due to crystallite microdistortions and sizes. The microdistortions can affect the two components of the profile and then have two components:

- 72 $$\varepsilon_G(\%) = \frac{\pi}{1.8}[U - U_0]^{1/2}$$

- 73 $$\varepsilon_L(\%) = \frac{\pi}{1.8}[X - X_0]$$

with U_0 and X_0 instrumental Gaussian and Lorentzian contributions respectively to the line broadening, which are determined on a standard sample.
The crystallite sizes is only Lorentzian:

- 74 $$T_L = K\lambda / H$$

with *K* the Scherrer constant and H the FWHM of the peak in 2θ. However the Lorentzian component of the microstrains is most usually neglected [Delhez et al. 1993, Langford et al. 1993, Lutterotti et al. 1994].

2.4. Crystal Structure Databases

Many crystal structure databases exist, that provide files of already determined structures which are understandable by crystallographic softwares. Among all the formats available, the ".CIF" format, developed by the International Union of Crystallography, is the most used. These files ease the incorporation of the structure atomic co-ordinates in the softwares, a fastidious task for large unit-cells wit lots of atoms, when the structure is already known or when the use of a closely-related structure is possible.

Depending on how has been elaborated each database, it is with full free access or not. When severe control of the files is warranted (for instance the CCSD, ICDD, CRYSMET databases), fees are applied. On the contrary, if the database has been developed by personal resources of researchers without careful assess of the files, no fee is asked to get the files (like the COD, AMCSD ... databases). For these latter, a smaller number of structures are accessible, because they have been developed more recently and only depend on the work of some researchers at spare times. However, they sometimes also contain "predicted structures" which may deserve some *ab-initio* structural determinations (like the PCOD extension of the COD database). Some programs like MAUD also allow to submit new .cif files to the COD directly via internet.

Most of the free databases are linked at http://www.ecole.ensicaen.fr/~chateign/texture/cif/ciffiles.htm

2.5. Reliability factors in profile refinements

The validation of a powder diffraction pattern refinement is a bit more delicate than ones on single crystals, based on intensities directly measured as integrated. On single crystal diagrams the angular information between crystalline directions is present which is not the case for powder diagrams. Lines of powder diffraction diagrams have to be deconvoluted in order to access the integrated intensities. Furthermore, each deconvoluted line of a powder diagram concerns all the multiplicity of **h**.

In order to evaluate the quality of the refinement, several factors have been introduced which allow the statistical comparison between the calculated model and the measured experiment [Hill et Flack 1987, Jansen et al. 1994]. The mostly used factors are:

- 75 R-pattern: $$R_p = \sum \left| y_{io} - y_{ic} \right| / \sum y_i$$

- 76 R-weighted profile: $$R_{wp} = [\sum_i w_{io} (y_{io} - y_{ic})^2 / \sum w_{io}\ y_i^{\,2}]^{1/2}$$

Here y_i is understood as the net intensities measured at step i. However some programs calculate R_{wp} including the background. This gives rise to lower R_{wp} values, particularly for high level backgrounds, since in the numerators of R_p and R_{wp} the difference (y_{io} - y_{ic}) suppresses the background influence while in the denominator background subsists. It is preferred to discriminate between R-factors which contain or are free of background intensities, the former being subscripted b (*e.g.* R_{wpb}, R_{pb} ...). We should note here that the assigned weights w_{io} should be calculated with the background included since they come from the errors made on the measures of the intensities, *i.e.* incorporating backgrounds.

To allow the comparison of the results with results that would have been obtained from single crystal data, it is convenient to use:

- 77 R-Bragg: $$R_B = \sum \left| I_k - I^{cal}{}_k \right| / \sum I_k$$

with $I_{\mathbf{k}} = mF_{\mathbf{k}}^2$, m being the multiplicity of the reflection

- 78 or $$I_k = \sum I_k{}^{cal} \Omega_{ik} \frac{y_{io} - y_{ib}}{y_{ic} - y_{ib}}$$

We also use:

- 79 R-structure factor: $$R_F = \sum \left| F_{\mathbf{k}} - F_{\mathbf{k}}{}^{calc} \right| / \sum F_{\mathbf{k}}$$

The R_{wp} value is dominated by the profile function and is not much sensitive to structural parameters, it then deserves preferably the profile comparison.

Since the number of parameters to fit, the way the parameters are linked to each other and the number of observations influence the value of all these factors, some other factors are used which are independent of them:

- 80 Goodness of fit: $$\chi^2 = \sum_i w_{io}(y_i - y_{ic} - y_{ib})^2 / (N - P + C) = (R_{wp} / R_{exp})^2$$

- 81 R-expected: $$R_{exp} = R_{wp} / \sqrt{\chi^2} = [(N - P + C) / \sum_i w_{io} {y_i}^2]^{1/2}$$

where *N* and *P* are the number of used information (y_i) and the number of refined parameters, and *C* the number of applied constraints between parameters.

The ''*Goodness-Of-Fit*'' χ^2 should go to 1 for an exact refinement. In practice its value is of course larger. The expected R_{exp} gives an hint about what one should expect as the best result from the experiment that have been measured.

Used in crystallography, all these factors are not necessarily perfectly satisfying from a statistical point of view, and particularly when counting statistics are too much low. In this latter case, the usual weighted least-squares minimisation of the Rietveld method and the maximum likelihood method (Fisher 1922) show very similar behaviours. However, when insufficient counting times have been available, the maximum likelihood approach is to be preferred, and for this reason, other parameters have been proposed in this case:

- The deviance D [Antoniadis et al. 1990], based on the maximum log-likelihood approach, which is a measure of the discrepancy between the actual model used for the fit (with p parameters to fit) and a model with as many parameters to fit as the number of observations:

- 82 $$D = 2\sum_{i=1}^{N}[y_i \ln \frac{y_i}{y_{ci}} - (y_i - y_{ic})]$$

with n the number of observations. For a fit with n-p degrees of freedom and no systematic error, the D distribution evolves approximately like χ^2, and can be used for goodness-of-fit purposes. From it one can calculate another estimator usable to measure the cost of additional parameters to fit in the model. It takes into account χ^2 and the number of independent parameters m(k) of the refinement for the k^{th} model:

- 83 $$C_k = D_k + \alpha(n)m(k)$$

Such parameters take the form of a penalised likelihood model, *i.e.* each additional parameter in the fit adds to the deviance and is represented by the penalty function $\alpha(n)m(k)$. D_k is the deviance of the k^{th} model, $\alpha(n)$ represents the cost of fitting an additional parameter. Such criterion is a special form of those introduced by Akaïke [1974] (C_{Akaike} uses $\alpha=2$ whatever n) and Schwartz [1978] ($C_{Schwartz}$ uses $\alpha = \ln(n)$). Schwarz's criterion favours models with fewer parameters than does Akaike's.

- The Dubin-Watson parameters *d* and *Q*: these two quantities were suggested by par Hill & Flack [1987]. They indicate the correlation between two closely-related remainders:

- 84
$$d = \sum_{i=1}^{N} [w_{io}(y_{io} - y_{ic}) - w_{io-1}(y_{io-1} - y_{ic-1})]^2 / \sum_{i=1}^{N} {w_{io}}^2 (y_{io} - y_{ic})^2$$

- 85
$$Q = 2\left[\frac{N-1}{N-P}.\frac{3.0902}{(N+2)^{1/2}}\right]$$

This correlation can be tested (at the 99,9% level) by comparison of *d* and *Q*. Three cases can arise:
- d≤Q: positive serial correlation, the (y_{io} - y_{ic}) of two neighbouring points get tendency to have the same sign. This is the most usual case of a refinement.
- Q<d<4-Q: There is no correlation between neighbouring points.
- d>4-Q: the serial correlation is negative, (y_{io} - y_{ic}) neighbouring points have in majority opposite signs.

Furthermore, in order to compare refinements operated on different measurements, the quality factors are depending on the measuring angular steps and counting times at each step. For instance, χ^2 and deviance vary proportionally to $\sqrt{t}$, *C* to $\sqrt{t}/s$ and *D* is linearly depending of *s* and *t*.

One of the best reliability criterion remains human eye, par comparing calculated and measured data at the end of the refinement. For instance using the difference curve.

2.6. Parameter exactness

The mostly used estimator of precision in Rietveld analysis is the standard deviation σ_j given by:

- 86
$$\sigma_j = [M^{-1}{}_{jj} \frac{\sum {w_{io}}^2 (y_{io} - y_{ic})^2}{N - P + C}]^{1/2}$$

with M_{jj} the diagonal matrix element of the inverse matrix.

Young et *al*. [1977] showed that for x-rays, the ratio between powder diffraction and single crystal standard deviations is 2 or 3 for all parameters, except for position parameters for which this ratio can be 1.

2.7: The Le Bail method

The Rietveld method is for the refinement of a crystal structure. When solving structures from powder data it is necessary to extract the intensities of the overlapping peaks without a structural model. The Le Bail method allows this, given a starting set of unit-cell parameters and a list of possible reflections. The method is similar to Rietveld in that a calculated profile is refined by least squares against the observed diffraction pattern. Hence lattice parameters, peak widths, peak–shape parameters are allowed to vary. The intensities

are, however, unknown. In the Rietveld method, at the end of the least–squares cycles, overlapping intensity can be partitioned between the reflections in the ratios predicted by the structural model. In the Le Bail method, the intensity is partitioned between overlapping peaks from arbitrarily assigned starting values – all equal say. At the end of the first cycle, the peaks no longer have equal intensities. The strong peaks will be strong, and the weak peaks weak. The process is repeated. The overlapping intensity is now partitioned using the new intensities such that the strong peaks take a larger fraction and another new set of intensities results. The process is cycled until a stable refinement is obtained. Hence the Le Bail method uses the observed intensities directly to partition the intensity between overlapping peaks.

Note that the Le Bail method may be used with neutron nuclear diffraction, synchrotron and conventional X–ray diffraction but not for magnetic scattering.

2.8: Refinement procedures

Since we will need here and in the next sections to deal with refinement, lets introduce here some of the procedures that are used in the adjustment of models to experimental data.

2.8.1. Least squares

Computationally, both the Rietveld and Le Bail methods may be divided into two parts:

- before a powder profile refinement can be successfully carried out, it is necessary to determine (from consideration of the lattice parameters, zero–point, halfwidth parameters and peak–shape function) which reflections from the specimen contribute to which part of the powder profile pattern. This is the preparation or « pre–profile » stage (which is actually transparent for the user) which is carried out just before least squares refinement takes place since it involves considerable reorganisation of data which must be regrouped in the most convenient form. The value of the least–squares weight assigned to each profile point is also calculated in this stage. This task must be carried out more than once during the course of refinement because alteration of the unit cell and profile parameters will change the relationship between the reflections and the observed profile. It is recommended that the profile preparation stage should be repeated whenever significant changes in the unit cell or profile parameters occur.

- the refinement of the structure or extraction of the intensities using the data prepared in the previous stage is then carried out. It is necessary to calculate the intensity expected at each point in the observed powder diffraction profile, and also the derivatives of that intensity with respect to the parameters.

The least squares equations used during refinement are constructed as follows. Let call p_j the parameters to be refined (variables), j varying from 1 to P. There are then a series of variables p_1 to p_P the subscript specifying which of the least squares equations refers to that parameter. For each profile point, contributions to the matrix equation:

- 87

$$[A] . [s] = [d]$$

must be evaluated. [A] is a symmetric, positive definite matrix of order P, which elements A_{mn} are:

- 88
$$\sum \left[w \left(\frac{\partial y_{ic}}{\partial p_m} \right) \left(\frac{\partial y_{ic}}{\partial p_n} \right) \right]$$

[d] is a column vector of order P which elements d_m are:

- 89
$$\sum \left[w \left(\frac{\partial y_{ic}}{\partial p_m} \right) (y_{io} - y_{ic}.\text{scale}) \right]$$

[s] is a column vector which is to be calculated after the inversion of the matrix [A]. The summations indicated are carried out over all profile points i. The elements of [s], s_n, are the shifts which are to be applied to the refined parameter p_j in order to yield better estimates of their true value. The Estimated Standard Deviations (ESD_j) of the refined parameters are then given by:

- 90
$$ESD_j = \sqrt{[A]^{-1} \sum \left[w (y_{io} - y_{ic}\text{scale})^2 \right] / (N - P + C))}$$

A^{-1} is the inverted matrix, N the total number of observations, P the number of refined parameters and C the number of constraining terms.

A more complete discussion of the least squares method is given by Rollett [1965].

2.8.2. Genetic or evolutionary algorithms

This kind of algorithms has been introduced as a powerful technique for solving optimisation and fitting problems (Goldberg 1989). Their ability to avoid local minima by following many search paths makes them particularly suited to refine data in which a relatively large number of parameters has to be fitted, relative to the number of experimental points. For instance, Torres-Costa et al. (2004) used them to fit visible reflectance spectra. In such methods, no gradient is calculated, but only a penalty function is evaluated.

In this approach, a possible solution of a given problem that depends on the x_i (i: 1 → n) parameters is represented as a vector **v** of the form:

- 91
$$\mathbf{v} = (x_1, x_2, ..., x_n)$$

With this set of parameters a simulation of the problem is calculated and compared with the experimental one. Then the penalty or cost function F(**v**) is calculated for all the J experimental points:

- 92
$$F(\mathbf{v}) = \sum_{j=1}^{J} P(i)(y_{io} - y_{ic})^2$$

Here the $P(y_i)$ factor is a weight similar to w_i in the Rietveld approach (Eq. - 23), except that it allows the incorporation of the weight dependence *versus* the analysed range. This parameter can then force a better fit in one spectral range compared to others.

The function F(**v**) is therefore representing the weighted misfit between simulated and experimental data. Hence lower F(**v**) values represent better fits.

The analogy to evolution lies in the following. Each refinable parameter is called a "gene", in such a way that the complete set of parameters, **v**, is a "chromosome". A population is an ensemble of individuals, each of them being defined by its own chromosome. Each individual represents a different simulation. The penalty function determines how much well adapted an individual is. The lower the F-value of the individual the more this individual is adapted to its "environment". Individuals are then crossed to each others, resulting in a given number of offsprings, produced from a mixture of the parents chromosomes. This population then evolves as evolutionary schemes, and the process ends with the best set of genes leading to best fits of the experimental data.

The algorithm starts then by initialising the population, a step in which a number of parents N_{par} are created. Each parameter of each one of the N_{par} individuals is assigned equally spaced values in the interval of all possible values. Then each individual has unique chromosome **v**.

In the next step, each parent has a given number of offsprings. For a given mother, the gene crossover can take place in two ways, 1 or 2, according to a probability p_1. In way 1 the offspring inherits each gene either from its father or his mother according to:

- 93
$$x_i^{son} = \begin{cases} x_i^{father} \text{ if } p < p_1 \\ x_i^{mother} \text{ if } p \geq p_1 \end{cases}$$

In way 2, the offspring's genes are simple averages of the parents':

- 94
$$x_i^{son} = (x_i^{father} + x_i^{mother}) / 2$$

Once the N_{off} offsprings have been generated, they suffer genes mutations, resulting in new genes (new parameter values) that did not exist before. This mutation takes place in every gene according to:

- 95
$$x_i^{son'} = x_i^{son} (1 + N_{(0,1)}T)$$

where T is the mutation size in that family and $N_{(0,1)}$ is a random value from a normal distribution. The mutation allows the creation of new genes, but also helps the algorithm escaping from false minima (it plays somehow the role of the temperature term in simulated annealing).

Then the penalty function is calculated for all the family members (father and N_{off} offsprings), and the one who has the lowest F(**v**) survives for the next generation, the others are rejected. If this one is the father, the algorithm has not improved the species in that generation and other mutations are required. If this is an offspring the species is improved, smaller mutations are required and the algorithm is getting closer to the final solution. In that case the family mutation size T is enlarged or reduced by a factor ε:

- 96
$$T' = T(1 \pm \varepsilon)$$

Equations - 93 to - 96 are repeated for all N_{par} individuals for a number N_{gen} of generations. Finally F(**v**) is computed for all individuals and the best adapted is chosen.

2.8.3. Derivative difference minimisation (DDM)

Solovyov [2004] proposes to introduce the minimisation of the derivative of the difference between measured and calculated profiles, rather than minimising their absolute difference. Such a procedure minimises the oscillations (curvature) of the difference profile, in order to better account for oscillations in the background than simple polynomial (or other) expressions. The minimisation function M is:

- 97
$$M = \sum \left\{ w^1 \left[\frac{\partial}{\partial \theta} (y_{io} - y_{ic}) \right]^2 + w^2 \left[\frac{\partial^2}{\partial \theta^2} (y_{io} - y_{ic}) \right]^2 + \ldots + w^j \left[\frac{\partial^j}{\partial \theta^j} (y_{io} - y_{ic}) \right]^2 \right\}$$

Which rewrites, using the Savitzky-Golay [1964] formalism:

- 98
$$M = \sum_{i=m+1}^{N-m} \sum_{j} w_i^j \left(\sum_{r=-m}^{m} c_r^j \Delta_{i+r} \right)^2$$

c_r^j are the SG coefficients for the derivative of order j in the profile convolution interval [-m,m], N is the number of measured points in the profile and $\Delta = y_{io} - y_{ic}$.

The structure and profile parameters, v_n, are introduced for refinement in the equations corresponding to the minimum of Eq. - 98:

- 99
$$\sum_{j} \sum_{i=m+1}^{N-m} w_i^j \left(\sum_{r=-m}^{m} c_r^j \Delta_{i+r} \right) \left(\sum_{r=-m}^{m} c_r^j \frac{\partial y_{c,i+j}}{\partial v_n} \right) = 0$$

The main advantage of this method is that it does not require the background line modeling or approximations. Eliminating the systematic errors caused by inadequate background definitions, the DDM approach allows structure refinement with increased stability and precision. The first implementation of such an algorithm was tested successfully in BDWS-9006PC [Wiles et Young, 1981].

2.9 Refinement Strategy

As every least-squares modelling technique, the Rietveld method possesses a limited convergence radius in the parameters space.

Provided minimised diffractometer aberrations (calibrated on a standard sample), one has to chose the best starting model. This is relatively easy for background and cell parameters. When the starting model is very rough, a *Whole Pattern Fitting may help*. All the parameters should not be released at once. Indeed, some parameters are strongly influencing the minimised function, and have to be refined first, while others may be released in the last steps. The following sequence is often used:

1. Scale factor + polynomial background.

2. Same + zero theta shift.
3. + atomic positions + global Debye-Waller factor. Atomic co-ordinates are refined beginning par the heaviest atoms (x-rays) or these that have the largest scattering cross-section (neutrons), adding them one by one.
4. + asymmetric sample parameters.
5. + site occupations.
6. + displacement parameters (+ individual anisotropic Debye-Waller factor)
7. + the five individual *Debye-Waller* factors.
8. + unit-cell parameters.

Using x-rays, the refinement of thermal anisotropic vibration parameters often lead to aberrant results. These parameters are more sensitive to large θ values.

It is always advisable to frequently plot the difference diagram in order to check for large mistakes and software stability. These are on some programs, sometimes together with reliability factors, lively available and can help in better defining the model or the refinement strategy to be used.

It may also be useful to limit the range of variation of the parameters to a physically meaningful domain, like giving lower and larger variable limits or obliging constraints between parameters. This is the case for instance for occupation sites in order to respect the chemical composition.

3 Automatic indexing of powder diagrams

3.1 Principle

The automatic *ab initio* indexing consists in retrieving unit-cell parameters of the reciprocal lattice from the peak positions (list of d*). This method relies on resolving the following system of linear equations from the quadratic form obtained by squaring the reciprocal-lattice vector $\mathbf{d^*} = h\mathbf{a^*} + k\mathbf{b^*} + \ell\mathbf{c^*}$:

- 100 $Q_i(hkl) = d_i^{*2} = h_i^2 a^{*2} + k_i^2 b^{*2} + \ell_i^2 c^{*2} + 2k_i\ell_i \mathbf{b^*}.\mathbf{c^*} + 2h_i\ell_i \mathbf{c^*}.\mathbf{a^*} + 2h_i k_i \mathbf{a^*}.\mathbf{b^*}$

Where h, k, ℓ are Miller indices and i: 1 .. N with N the number of observed lines. Equation -100 rewrites:

- 101 $|Q_i(hkl) - h_i^2 a^{*2} - k_i^2 b^{*2} - \ell_i^2 c^{*2} - 2k_i\ell_i \mathbf{b^*}.\mathbf{c^*} - 2h_i\ell_i \mathbf{c^*}.\mathbf{a^*} - 2h_i k_i \mathbf{a^*}.\mathbf{b^*}| \leq \Delta Q_i$

in which ΔQ_i is the error in Q_i that one can accept for the system.

In this equation, **a***, **b*** anc **c*** are the unknown vectors of the reciprocal lattice. In this system the number of equations (N) is always smaller than the number of unknowns (*i.e.* 6 for a triclinic, 4 for monoclinic, ..., 1 for cubic lattices, and N sets of three indices h_i, k_i, ℓ_i). Hence there is no algebraic solution to this problem.

Resolving methods to this equation have been described since the earliest times [Runge 1917, Ito 1949, de Wolff 1957]. The main indexing method developments are described by Shirley [1980, 1990] and Louër [1991].

We just mention here a quick view of the three main approaches:

- The Runge-Ito-de Wolff method, based on the research of zones, lies on the existence of specific relationship in the reciprocal space. Visser [1969] proposed the first automatic program for powder diagram indexing.

- The procedure of Werner [1964], based on Miller indices permutations of the main lines. It uses a semi-exhaustive trial and error approach. Werner's principle is used in several programs [Taupin 1973, Kohlbeck et Hörl 1976, Kohlbeck et Hörl 1978, Werner et *al*. 1985].

- The dichotomy approach which we will describe a bit more in the next paragraph.

3.2 Dichotomy approach

The principle of the dichotomy procedure has been described by Louër et Louër (1972) for crystal systems down to orthorhombic, and later for the monoclinic and triclinic cases [Louër et Vargas 1982, Shirley 1990], then implemented in the program *DICVOL91* [Boultif et Louër 1991]. In the more recent version *DICVOL04* [Boultif et Louer 2004]

several problems occurring during automating search are addressed like the zero-angle offset, the cell analysis and unindexed diffraction lines.

In this approach, Equation - 100 is parameterised as $Q_i(hkl) = f(\mathbf{h},\mathbf{x})$, **x** being a vector formed by the n cell constants (n := 1 .. 6 depending on the crystal system) and **h** is a vector with three components (k,k,ℓ). Since we *a priori* do not know which are the cell parameters, one has to define ranges of variations for these parameters, *i.e.* the x_i components of **x** have to vary from minimum to maximum values, x_i^{min} and x_i^{max} respectively. This finally defines a n-dimensional domain D for cell parameter variations and a 3-dimensional domain H for Miller indices variations:

- 102 $$D = [x_1^{min},x_1^{max}] \times [x_2^{min},x_2^{max}] \times \ldots \times [x_n^{min},x_n^{max}]$$

- 103 $$H = [h^{min},h^{max}] \times [k^{min},k^{max}] \times [\ell^{min}, \ell^{max}]$$

Within a defined experimental range (*e.g.* 2θ range), this limits the number of **h** to N possible values that forms the set H of **h**.

In turns, D then admits lower and higher bounds for f, f^{min} and f^{max} respectively calculated from all the h and x values. Then, if for a given D one cannot find $f \in [f^{min}, f^{max}]$ whatever **h** in H, no solution is found for indexing, the domain D is eliminated and a new one created. Conversely, if a solution exists in D, this domain is further explored by bisecting each $[x_i^{min},x_i^{max}]$, *i.e.* D is divided into 2^n sub-domains. Each sub-domain is then examined and the procedure repeated several times to a given resolution.

The potential solutions found for cell parameters are then refined (by least-squares procedures for instance), including or not 2θ systematic shift and sample displacement. If these latter are too large, it may happen that the indexing vanishes, and the corrections must be applied before indexing using for instance a standard powder or the reflection-pair method [Dong et al., 1999].

3.3 Criterions for quality

In order to discern between solutions, de Wolff [1968] suggests the M_N factor and Smith et Snyder [1979], F_N:

- 104 $$M_N = Q_N / 2\langle \Delta Q \rangle N_{poss}$$

- 105 $$F_N = N / \langle \Delta(2\theta) \rangle N_{Poss}$$

with:

$$Q_N = \left(1 \middle/ d_N^2 \right)$$

N_{poss} is the number of theoretical peaks up to the n^{th} observed line. $<\Delta Q>$ and $<\Delta(2\theta)>$ are the average absolute discrepancies between Q_{calc} and Q_{obs} , $2\theta_{obs}$ and $2\theta_{cal}$ respectively.

4 Quantitative Texture Analysis (QTA)

4.1. The orientation Distribution Function (ODF)

4.1.1. Definition

The quantitative determination of the texture is based on the concept of Orientation Distribution Function, f(g), which represents the statistical distribution of the orientations of the constitutive crystals (crystallites) in a polycrystalline aggregate:

- 106

$$\frac{dV(g)}{V} = \frac{1}{8\pi^2} f(g)\, dg$$

where $dg = \sin\beta\, d\beta\, d\alpha\, d\gamma$ is the orientation element, defined by three Euler angles $g = \{\alpha,\beta,\gamma\}$ (Figure 10) in the orientation space (or $\mathscr{A}$-space), that bring a given crystal co-ordinate system K_B co-linear with the sample co-ordinate system K_A = (**X,Y,Z**), or (**100**, **010**, **001**). The $\mathscr{A}$-space can be constructed from the space groups, taking into account their rotation symmetry operators and the inversion centre. The two first angles β and α determine generally the orientation of the $[001]^*$ crystallite direction in K_A, they are called co-latitude (or pole distance) and azimuth respectively. The third angle, γ, defines the location of another crystallographic direction, chosen as $[010]^*$ (in the (a,b) plane or orthogonal crystal cells). V is the irradiated volume (if one uses diffraction experiments) of the sample, dV(g) the volume of crystallites which orientation is between g and g+dg.

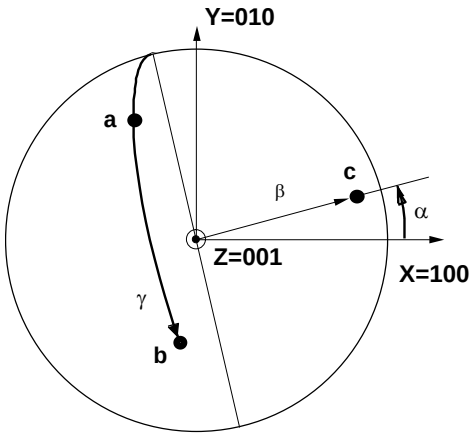

Figure 10: Definition of the three Euler angles that define the position of the crystallite co-ordinate system K_B=(**a**,**b**,**c**) of an orthogonal crystal cell in the sample co-ordinate system K_A=(**X**,**Y**,**Z**). Note, **100**, **010** and **001** are not Miller indices but vectors referring to an ortho-normal frame aligned with K_A

4.1.2. Angle conventions

There are numerous angular conventions used by the different authors. These are summarised in Table 1 for the most used angular sets. Figure 11 illustrates the Roe/Matthies and Bunge's conventions for bringing X_1, Y_1 and Z_1 axes colinear respectively to X_2, Y_2 and Z_2.

For instance, in the Roe-Matthies frame, K_1 is brought coincident to K_2 by the operation $g : [K_1 \mapsto K_2]$, using the three following rotations:

- Rotation of K_1 about the axis Z_1 through the angle α:
  $[K_1 \mapsto K'_1]$; associated rotation $g_1 = \{\alpha,0,0\}$
- Rotation of K'_1 about the axis Y'_1 through the angle β:
  $[K'_1 \mapsto K''_1]$; associated rotation $g_2 = \{0,\beta,0\}$
- Rotation of K''_1 about the axis Z''_1 through the angle γ:
  $[K''_1 \mapsto K'''_1 // K_2]$; associated rotation $g_3 = \{0,0,\gamma\}$

we obtain finally:

$$g = g_1\, g_2\, g_3 = \{\alpha,0,0\}\ \{0,\beta,0\}\ \{0,0,\gamma\} = \{\alpha,\beta,\gamma\}$$

Using the Bunge convention:

- Rotation of K_1 about the axis Z_1 through the angle φ_1:
  $[K_1 \mapsto K'_1]$; associated rotation $g_1 = \{\varphi_1,0,0\}$
- Rotation of K'_1 about the axis X'_1 through the angle Φ:
  $[K'_1 \mapsto K''_1]$; associated rotation $g_2 = \{0,\Phi,0\}$
- Rotation of K''_1 about the axis Z''_1 through the angle φ_2:
  $[K''_1 \mapsto K'''_1 // K_2]$; associated rotation $g_3 = \{0,0,\varphi_2\}$

Matthies	Roe	Bunge	Canova	Kocks
α	Ψ	$\varphi_1 = \alpha + \pi/2$	$\omega = \pi/2 - \alpha$	Ψ
β	Θ	Φ	Θ	Θ
γ	Φ	$\varphi_2 = \gamma + 3\pi/2$	$\phi = 3\pi/2 - \gamma$	$\Phi = \pi - \gamma$

Table 1: Correspondences between the most used Euler angle sets

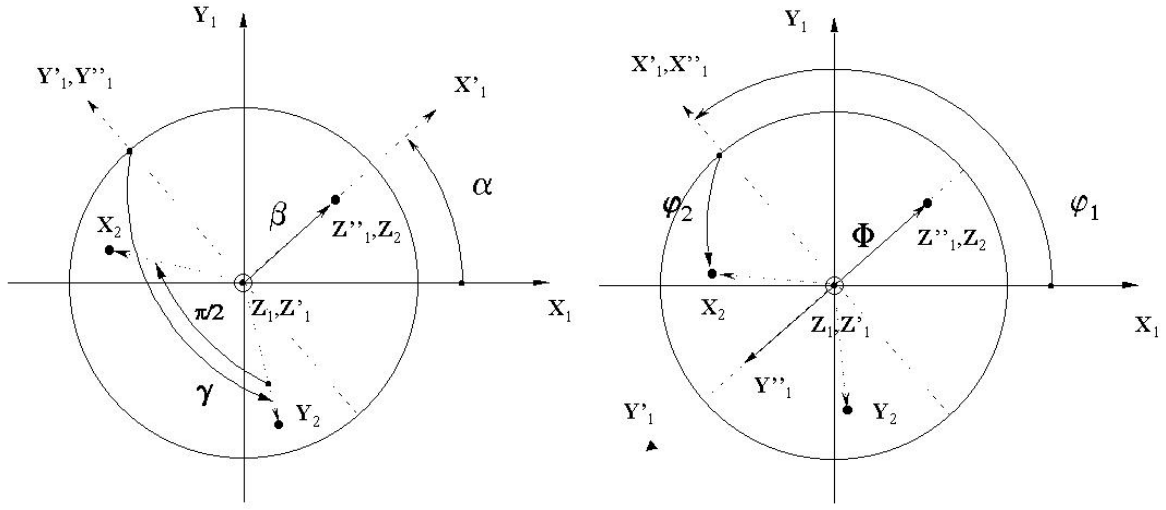

Figure 11: Definition of the three Euler angles in the Roe-Matthies (left) and Bunge's (right) conventions

4.1.3. Orientation distance

The distance $\tilde{g}$ between two orientations g_1 and g_2 can be calculated, similarly as the angle difference for planar angles, by the orientation difference using the contribution of the three rotations in the Euler space, with:

- 107

$$\tilde{g} = \tilde{g}(g_2, g_1) = g_1^{-1} g_2$$

- 108

$$\begin{aligned}\cos\tilde{g} = \frac{1}{2}[&\cos(\alpha_1 - \alpha_2)\cos(\gamma_1 - \gamma_2)(1 + \cos\beta_1 \cos\beta_2) \\ &- \sin(\alpha_1 - \alpha_2)\sin(\gamma_1 - \gamma_2)(\cos\beta_1 + \cos\beta_2) \\ &+ [\cos(\alpha_1 - \alpha_2) + \cos(\gamma_1 - \gamma_2)]\sin\beta_1 \sin\beta_2 + \cos\beta_1 \cos\beta_2 - 1]\end{aligned}$$

if the Roe-Matthies convention is used [Matthies et al. 1987], or

- 109

$$\begin{aligned}\cos\frac{\tilde{g}}{2} = [&\cos\left(\frac{\varphi_{11} - \varphi_{12}}{2}\right)\cos\left(\frac{\varphi_{21} - \varphi_{21}}{2}\right)\cos\left(\frac{\Phi_1 - \Phi_2}{2}\right) \\ &- \sin\left(\frac{\varphi_{11} - \varphi_{12}}{2}\right)\sin\left(\frac{\varphi_{21} - \varphi_{21}}{2}\right)\sin\left(\frac{\Phi_1 - \Phi_2}{2}\right)\end{aligned}$$

for the Bunge convention [Bunge et Esling 1982].

4.2. Distribution density and normalisation

The function f(g) then represents the volumic density of crystallites oriented in dg. It is measured in m.r.d. (multiple of a random distribution) and normalised to the value $f_r(g) = 1$ m.r.d. for a sample without any preferred orientation (or random or powder). These values are called orientation distribution densities, and the function f(g) can take values from 0 (absence of crystallites oriented in dg around g) to infinity (for some of the $\mathcal{H}$-space values of single crystals).

The normalisation condition of f(g) over the whole orientation space is expressed by:

- 110

$$\int_{\varphi_y=0}^{2\pi} \int_{\vartheta_y=0}^{\pi/2} \int_{\gamma=0}^{2\pi} f(g)\, dg = 8\pi^2$$

4.3. Direct and normalised Pole figures

Experimental measurements are the so-called direct pole figures, $I_{\mathbf{h}}(\mathbf{y})$, with $\mathbf{h}=\langle hk\ell\rangle^*$ and $\mathbf{y}=(\vartheta_y,\varphi_y)$ (Figure 12). They always are incomplete in some way. They determine the distribution of the normals $\langle hk\ell\rangle^*$ to the crystallographic planes $\{hk\ell\}$ which are diffracting for the (ϑ_y,φ_y) orientation of the sample in K_A, pole figure space . For one direct pole figure, **y** is varied in order to cover the maximum range of orientations.

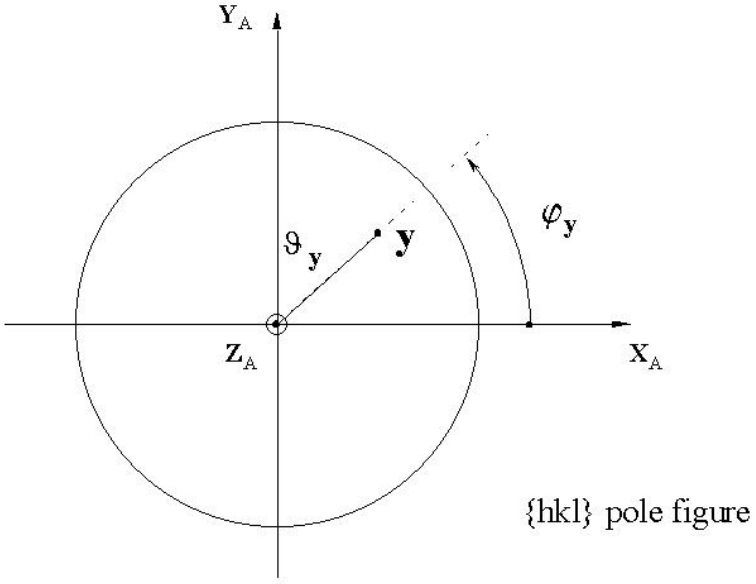

Figure 12: Pole figure co-ordinates in the sample reference frame K_A

The diffracted intensities $I_{\mathbf{h}}(\mathbf{y})$ depend on the porosity, crystalline state, ..., of the sample. To compare samples between each others a quantity only depending on the orientation has to be calculated. This quantity is the normalised pole figure $P_{\mathbf{h}}(\mathbf{y})$, representing the distribution densities of **h** directions on the pole sphere, comprised inside dy $= \sin\vartheta_y \, d\vartheta_y \, d\varphi_y$:

- 111
$$\frac{dV(\varphi_y \vartheta_y)}{V} = \frac{1}{4\pi} P_{\mathbf{h}}(\varphi_y \vartheta_y) \sin\vartheta_y d\vartheta_y d\varphi_y$$

and similarly to f(g), every pole figure of a random sample will have the same density $P_{\mathbf{h}}(\mathbf{y}) = 1$ m.r.d.. The $P_{\mathbf{h}}(\mathbf{y})$ are in fact the factors $P_{\Phi k}$ of Equation - 24.

The normalisation of the pole figures is, similarly as in Eq. - 110, operated through:

- 112
$$\int_{\varphi_y=0}^{2\pi} \int_{\vartheta_y=0}^{\pi/2} P_{\mathbf{h}}(\varphi_y \vartheta_y) \sin\vartheta_y \, d\vartheta_y d\varphi_y = 2\pi$$

4.4. Reduced pole figures

Let mention at this step that the pole figures obtained using normal diffraction methods are the so-called reduced ones, $\widetilde{P}_{\mathbf{h}}(\mathbf{y})$. The Friedel's law makes that the measured pole figures are superpositions of +**h** and -**h** true pole figures. The fact that for normal diffraction (and for centrosymmetric crystal systems even for anomalous scattering too) only reduced pole figures can be measured is known for texturologists as 'ghost' phenomena [Matthies et Vinel 1982, Matthies et al. 1987]. The true, unreduced, pole figure is defined by:

- 113
$$P_{\mathbf{h}}(\mathbf{y}) = \widetilde{P}_{\mathbf{h}}(\mathbf{y}) + \widetilde{\widetilde{P}}_{\mathbf{h}}(\mathbf{y})$$

in which $\tilde{\tilde{P}}_{\mathbf{h}}(\mathbf{y})$ is the non measured part of the pole figure.

We will not take account of this here since the ghost suppression, if possible, would need anomalous diffraction and very intense beams. Instead, theoretically derived ghost-correcting approximations will be used.

4.5. Fundamental equation of texture analysis

4.5.1. Fundamental equation

However, one pole figure is only a measure of the distribution of one direction type <hkℓ>*. Any rotation around this direction by a $\tilde{\varphi}$ angle results in the same diffracted intensity.

Following Equations - 106 and - 111, one can obtain the fundamental equation of texture analysis:

- 114
$$P_{\mathbf{h}}(\mathbf{y}) = \frac{1}{2\pi} \int_{\mathbf{h}//\mathbf{y}} f(g) d\tilde{\varphi}$$

This equation represents the fact that each pole figure (a 2D object) is a projection along a certain path $\tilde{\varphi}$ of the ODF (a 3D object), which of course depends on the crystal symmetry (Figure 13). Each cell of a given pole figure will then be an average over several cells of the ODF, and each cell of the ODF will be measured by one or more cells from the pole figures. The larger the number of pole figure cells that measure a specific ODF cell and the more statistically reliable is the measurement of this ODF. In practice, one has to measure the largest number as possible of reliable (enough intense) pole figures to define the ODF with the best resolution available.

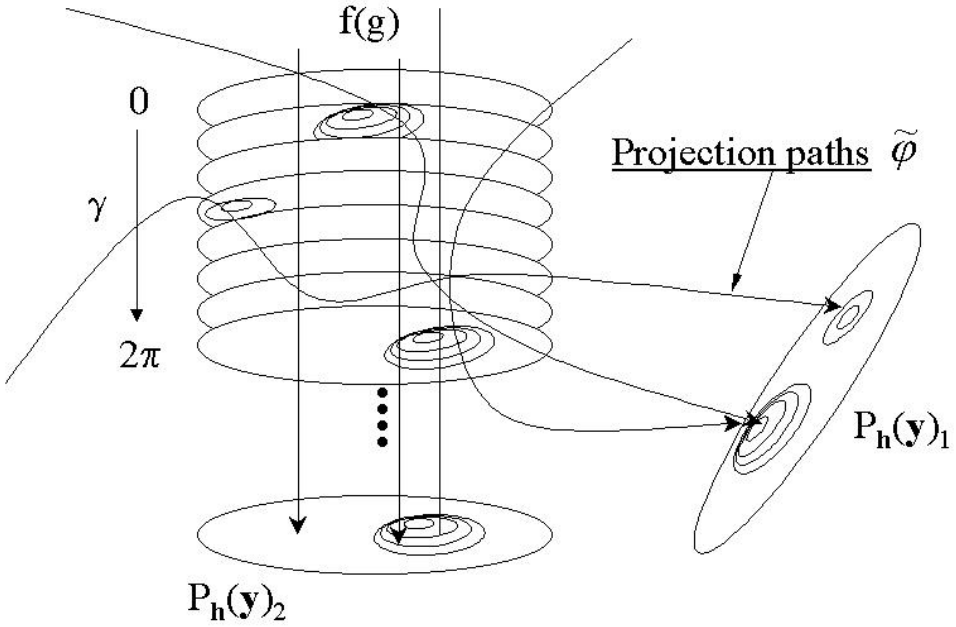

Figure 13: Relationship between the 3D object f(g) and the pole figures $P_{\mathbf{h}}(\mathbf{y})$. To each pole figure cell corresponds several ODF boxes, and each ODF box is linked to several pole figure cells.

Equation - 114 was solved several years ago by Bunge, using generalised spherical harmonics formulation [Bunge et Esling 1982, Bunge 1982], but only in the case of high crystal symmetries. An exact solution of (4-7) in an analytical closed form without any series expansion was given [Matthies 1979], which permits, in a systematic way, to analyse the properties of the ghosts and to develop reasonable ghost correcting algorithms. The so-called "vector" [Ruer 1976, Vadon 1981], entropy maximisation [Schaeben 1988] and ADC [Pawlik 1993] methods were developed later.

4.5.2 Typical ODFs

4.5.2.1. Random ODF and random part: FON

A sample exhibiting randomly oriented crystallites has an ODF with 1 m.r.d. distribution densities for all g values. However, in some samples only a fraction of the total volume is randomly oriented, V_r, the rest, $V_c(g)$, being the oriented fraction volume having the orientation component or components, $f_c(g)$. The random part produces a "background" level in the ODF, sometimes called "FON", and one can decompose the ODF in:

- 115
$$f(g) = f_r + f_c(g)$$

with the mandatory condition $0 \le f_r \le 1$.

By integrating Equation - 106 and taking into account Equation - 115, one obtains:

$$\frac{1}{V}\oint[V_r + V_c(g)]\,dV(g) = \frac{1}{8\pi^2}\oint[f_r + f_c(g)]\,dg$$

which verifies after identification:

- 116
$$V_r / V = f_r \quad \text{for the random part, and}$$
$$\frac{dV_c(g)}{V} = \frac{1}{8\pi^2} f_c(g)\,dg \quad \text{for the textured part}$$

This strictly means that the minimum value of the ODF, e.g. $f_r = 0.3$ m.r.d., identifies with the random volume fraction, i.e. 30 % of the material is randomly oriented in this case.

4.6. Resolution of the fundamental equation

4.6.1. ODF and OD

Before describing the various methods to solve the fundamental equation of QTA, one may have noticed that authors refer here or there to OD or ODF. The latter case implicitly ascribe a given function to the distribution of crystallites. This is for instance the case of the generalised spherical harmonics or the component methods. However, there is no *a priori* needs for fitting a function to the data, and many "direct" methods (*e.g.* the maximisation of

entropy, vector or WIMV methods) have been developed that do not. In this case the term "Function" can be omitted.

We will respect this scheme in the following, calling OD only the f(g) that have been fitted from direct methods. But bear in mind that, even for ODs that have been refined using direct methods, it is somewhat hard to represent ODs on figures without using contour and isolines, which in turns are results of interpolations of discrete OD points by functions (*e.g.* splines).

4.6.2. Generalised spherical harmonics

4.6.2.1. Principle

The solution proposed by Bunge et Esling [1982] consists in developing the ODF and the pole figures into series of generalised spherical harmonics:

- 117
$$f(g) = \sum_{\lambda=0}^{\infty} \sum_{m,n=-\lambda}^{\lambda} C_\lambda^{mn} T_\lambda^{mn}(g)$$

and

- 118
$$P_{\mathbf{h}}(\mathbf{y}) = \sum_{\lambda=0}^{\infty} \frac{4\pi}{2\lambda+1} \sum_{n=-\lambda}^{\lambda} k_\lambda^n(\mathbf{y}) \sum_{m=-\lambda}^{\lambda} C_\lambda^{mn} k_\lambda^{*m}(\Theta_{\mathbf{h}} \phi_{\mathbf{h}})$$

The Equation - 114 still holds, and in this approach one has to determine the C_λ^{mn} Fourier coefficients from the experiments, which are the proportions of the respective T_λ^{mn}. The T_λ^{mn} are known generalised spherical harmonics which depend on the crystal and texture symmetries. k_λ^n and k_λ^{*m} are spherical harmonics based on Legendre polynomia. The angles $\Theta_{\mathbf{h}}$ and $\phi_{\mathbf{h}}$ are the spherical co-ordinates of the **h** direction in the crystal reference frame.
T_λ^{mn} functions are given by:

- 119
$$T_\lambda^{mn} = e^{im\gamma} P_\lambda^{mn}(\beta) e^{in\alpha}$$

with

- 120
$$P_\lambda^{mn}(\beta) = \frac{(-1)^{\lambda-m} i^{n-m}}{2^\lambda (\lambda-m)!} \sqrt{\frac{(\lambda-m)!(\lambda+n)!}{(\lambda+m)!(\lambda-n)!}} (1-\beta)^{\frac{m-n}{2}} (1+\beta)^{-\frac{m+n}{2}} \frac{d^{\ell-n}}{d\beta^{\ell-n}} \left[(1-\beta)^{\ell-m}(1+\beta)^{\ell+m}\right]$$

and k_λ^n, k_λ^{*m} by:

- 121
$$k_\lambda^s(\varsigma,\upsilon) = \frac{1}{\sqrt{2\pi}} \sum_{j=-\lambda}^{\lambda} a_\lambda^{sj} e^{i(j\varsigma+s\upsilon)}$$

with

- 122
$$a_\lambda^{sj} = i^s \sqrt{\frac{2\lambda+1}{2}} Q_\lambda^{sj} Q_\lambda^{0j} \text{ and}$$

- 123
$$Q_\lambda^{sj} = i^{s+j} P_\lambda^{sj}\left(\frac{\pi}{2}\right)$$

The T_λ^{mn} and k_λ^n factors need to respect orthonormality conditions. Their formulation can be simplified by the crystal and texture symmetries. The number of C_λ^{mn} coefficients to be refined and the extension L to which the series in Eq. - 117 has to be expended in λ are also depending on these symmetries.

4.6.2.2. Diffraction and Positivity of f(g)

Using normal diffraction Friedel's law applies and one cannot dissociate diffracted intensity $I_{\mathbf{h}}$ from $I_{-\mathbf{h}}$. Consequently the pole figures are even objects, and it comes out:

- 124 $$\overline{P}_{\mathbf{h}}(\mathbf{y}) = [P_{\mathbf{h}}(\mathbf{y})+P_{-\mathbf{h}}(\mathbf{y})]/2$$

which gives rise that the measured pole figures of Equation - 118 are only the even orders of the development into Fourier series. On another hand f(g) can be either even or odd, and two different ODF objects have then to be dissociated, depending on the parity of the λ terms exist:

- 125 $$f^e(g) = \sum_{\lambda=0(2)}^{\infty} \sum_{m,n=-\lambda}^{\lambda} C_\lambda^{mn} T_\lambda^{mn}(g)$$

for even terms, and

- 126 $$f^o(g) = \sum_{\lambda=1(2)}^{\infty} \sum_{m,n=-\lambda}^{\lambda} C_\lambda^{mn} T_\lambda^{mn}(g)$$

for odd terms.

and

- 127 $$f(g) = f^e(g) + f^o(g)$$

The even part of the harmonic series $f^e(g)$ being the part accessible to normal diffraction, the odd part being measurable only using anomalous scattering. This phenomenon creates ghosts (negative, unphysical distribution densities) in the ODF [Matthies 1979, Matthies et Vinel 1982] undesirable for a quantitative description of f(g).

An approximative "ghost correction" by creating the odd orders is very complicated in the harmonic apparatus [Esling et al. 1982]. One approach for this correction is called the "positivity method" [Dahms et Bunge 1988, Wagner et Dahms 1991], but in any case up to now there is no theoretical justification of applying the positivity.

Also, for strongly textured samples, the harmonics formulation creates strong negative density values and has been proved to be less adequate than other discrete methods. A philosophical disadvantage of the method is that it assumes a particular shape of the distributions, the one that corresponds to a harmonic analytical formulation, whereas it does not correspond in all cases to a real physical description. This is why in this text f(g) refers to the Orientation Distribution (or OD) of the crystallites instead of the Orientation Distribution Function (or ODF) of many texture textbooks.

However, one advantage of using harmonic series is that it provides the necessary material for the simplest approximation of the mechanical property simulations with a limited number of coefficients to be refined (the harmonic coefficients in fact). These coeeficients

can now however be computed from the Orientation Distributions as calculated with discrete methods.

4.6.2.3. Least-squares refinement

The residual value to be minimised by a least square refinement using harmonics is:

- 128
$$\sum_{\mathbf{h}} \sum_{\mathbf{y}} \left[I_{\mathbf{h}}(\mathbf{y}) - N_{\mathbf{h}} P_{\mathbf{h}}(\mathbf{y}) \right]^2 \mathbf{dy}$$

with $dy = \sin\vartheta_y \, d\vartheta_y \, d\varphi_y$

$N_{\mathbf{h}}$ here represents a normalising factor which has to be refined for each pole figure.

4.6.3. Vector method [Ruer 1976, Ruer et Baro 1977, Vadon 1981]

The vector method is a discrete method which works in the direct space. In this method f(g) is represented by a vector called "Texture vector" $\mathbf{f}_j$, j: 1 .. J, with J the number of cells in which f(g) is discretised. This number of course depends on the resolution of the measurement scans of the pole figures. In the method each pole figure is represented by $\mathbf{P}_i(\mathbf{h})$, i: 1 .. N, with N the number of cells of the pole figure.

Using this approach, the fundamental equation of texture becomes:

- 129
$$P_i(\mathbf{h}) = [\sigma_{ij}(\mathbf{h})] \, \mathbf{f}_j$$

$\sigma_{ij}(\mathbf{h})$ being a P unknowns x N equations rectangular matrix.

The fundamental problem consists therefore in finding the solution of the system - 129 of linear equations, using an iterative calculation process.

4.6.4. Williams-Imhof-Matthies-Vinel (WIMV) method [Williams 1968, Imhof 1982, Matthies et Vinel 1982]

4.6.4.1. Regular WIMV

The WIMV approach [Matthies et Vinel 1982, Matthies et Wenk 1985] for the refinement of the OD is an iterative way which ensures a conditional ghost correction. It is based on the numerical refinement of f(g) at step n+1:

- 130
$$f^{n+1}(g) = N_n \frac{f^n(g) f^0(g)}{\left(\prod_{\mathbf{h}=1}^{\mathrm{I}} \prod_{m=1}^{M_{\mathbf{h}}} P_{\mathbf{h}}^n(\mathbf{y}) \right)^{\frac{1}{IM_{\mathbf{h}}}}}$$

where the product extends over the I experimentally measured pole figures and for all the poles multiplicity $M_{\mathbf{h}}$, $f^n(g)$ and $P_{\mathbf{h}}^n(\mathbf{y})$ represent the refined values of f(g) and $P_{\mathbf{h}}(\mathbf{y})$ at the

n^{th} step respectively. The number N_n is a normalising factor. The $P_{\mathbf{h}}^{n}(\mathbf{y})$ values are calculated at each cycle with Eq. - 114. The first step in this procedure is to evaluate $f^0(g)$:

- 131
$$f^{0}(g) = N_0 \left(\prod_{\mathbf{h}=1}^{\mathrm{I}} \prod_{m=1}^{M_{\mathbf{h}}} P_{\mathbf{h}}^{\exp}(\mathbf{y}) \right)^{\frac{1}{IM_{\mathbf{h}}}}$$

in which $P_{\mathbf{h}}^{\exp}(\mathbf{y})$ stands for the measured pole figures.

The WIMV algorithm maximises the so-called "phon" (orientation background or minimum value of the OD which represents the randomly oriented fraction of the sample) and the texture sharpness.

While in the previous methods of OD resolution low texture and crystal symmetries give rise to large numbers of data to store and large computation times, the WIMV approach does not depend much on these symmetries.

4.6.4.2. Extended WIMV (E-WIMV)

The regular WIMV method necessitates an OD discretised in a finite number of regular cells. Inside each cell a discrete value of the OD is associated. When the WIMV calculation is inserted inside the Rietveld refinement procedure, it requires two additional steps:

- the extraction of the pole figures or texture weights
- the interpolation of these weights to fit the regular grid

This renders non-optimised values of the OD, particularly for sharp textures and coarse irregular coverage of the OD.

The E-WIMV approach can be used with irregular coverage of the OD space and includes smoothing based on a concept similar to the tube projection of the ADC method [Pawlik 1993]. The extension of the method provides with an iterative scheme of the OD refinement which is very close to the maximisation of entropy [Schaeben 1991]. The E-WIMV method is then often called Entropy-modified WIMV [Cont et al. 2002, Morales et al. 2002]. The OD cell values are computed through an entropy iteration algorithm that includes the reflection weights:

- 132
$$f^{n+1}(g) = f^{n}(g) \prod_{m=1}^{M_{\mathbf{h}}} \left(\frac{P_{\mathbf{h}}(\mathbf{y})}{P_{\mathbf{h}}^{n}(\mathbf{y})} \right)^{r_n \frac{w_{\mathbf{h}}}{M_{\mathbf{h}}}}$$

in which r_n is a relaxation parameter such that $0 < r_n < 1$, $M_{\mathbf{h}}$ is the number of division points for the discretisation of the integral of all the orientations around the scattering vector for the pole figure **h**. The reflection weight $w_{\mathbf{h}}$ is introduced to take into account the different accuracy of the more intense and less overlapped reflections with respect to the smaller ones, and is calculated analogously to the weight factors of the Rietveld analysis.

This approach proved its efficiency [Cont et al. 2002, Morales et al. 2002, Lutterotti et al. 2004].

4.6.5. Arbitrarily Defined Cells (ADC) method [Pawlik 1993]

The ADC method is essentially based on a WIMV algorithm. But, instead of calculating pole figures from the OD cells using a projection path, the ADC uses projection tubes which depend on the pole figure cells of concerns. Then, each cell volume is taken into account in the calculations which gives a better smoothing scheme. Also, some choices are operated between the iteration steps depending on the OD cell values relative to 1 m.r.d..

This approach has been compared to others [Wenk et al. 1994] on materials with a relatively low texture strength and did not show neither better nor worse results than the WIMV algorithm.

4.6.6. Entropy maximisation method [Schaeben 1988, Schaeben 1991, Schaeben 1991a]

This method is based on the maximization of the texture 'disorder' or texture entropy, *i.e.* trying to obtain the maximum texture phon from a set of experiment. Following information theory [Shannon 1948, Shannon 1949], the entropy estimator in texture can be estimated by:

- 133
$$S = \sum_i f(g_i) \ln f(g_i)$$

which results in the iterative procedure:

- 134
$$f^{n+1}(g) = f^n(g) \prod_{m=1}^{M_h} \left(\frac{P_h(y)}{P_h^n(y)} \right)^{\frac{r_n}{M_h}}$$

with the previously defined r_n. One can see that, except for the weighting schemes inherent to the Rietveld implementation of the texture, Equation - 134 is exactly the same as Eq. - 132.

4.6.7. Component method [Helming 1998]

4.6.7.1. Description

For very strong textures most of the orientation space cells has zero-values, while few cells exhibit very large distribution densities. In such cases the number of data to be acquired can be tremendously large and tend to an unacceptable limit. However, since the ODF is described by a small number of g orientations, simple functions can be used to represent it, which g values are easily handled. This leads to a drastic reduction of data.

Let a specific texture component centred at the $g = g^c$ orientation be represented by the model-function $f^c(g)$. The total ODF can be represented by:

- 135
$$f(g) = F + \sum_c I^c f^c(g)$$

where the intensity I^c is the volume fraction of crystallites belonging to the component g^c of distribution $f^c(g)$, and F represents the volume fraction of randomly oriented crystallites. For consistency the components have to respect the normalisation conditions:

- 136
$$F + \sum_c I^c = 1 \text{ and } \sum_c f^c(g) = 1$$

The $f^c(g)$ components can be represented by any function, *i.e.* gaussian distributions, that warranty the normalisation possibility. However they are mostly represented using Gaussian functions.

4.6.7.2. Gaussian components [Bunge 1969, Matthies et al. 1987]

$f^c(g)$ represents the orientation distribution of crystallites by using the orientation distance $\tilde{g}$ that separates g from g^c:

- 137
$$f(g, g^c) = f(\tilde{g}) = \frac{2\sqrt{\pi}}{\zeta\left\{1 - \exp\left(-\left(\frac{\zeta}{2}\right)^2\right)\right\}} \exp\left(-\left(\frac{\tilde{g}}{\zeta}\right)^2\right)$$

in which ζ is the Half Width at Half maximum of the component Density (HWHD). This function decreases with increasing $\tilde{g}$. Since there is only one half-width to represent the distribution of the component, such distribution is called spherical component.

One of the properties of the $\mathscr{A}$-space is that $f(\pi+\tilde{g}) = f(\pi-\tilde{g})$. Gaussian functions that respect this conditions are called standard Gauss functions [Matthies et al. 1987]:

- 138
$$f(\tilde{g}) = N(S)\exp\left(S\cos\tilde{g}\right)$$

with
$$S = \frac{\ln 2}{1 - \cos\left(\frac{\zeta}{2}\right)} \qquad \text{and} \qquad N(S) = \frac{1}{I_0(S) - I_1(S)}$$

$I_n(x)$ being the modified Bessel functions.

4.6.7.3. Elliptical components [Matthies et al. 1987]

The component $f^c(g)$ can also be preferably extended along one direction, relative to the sample coordinate system K_A. This gives rise to two FWHD, one being ζ, and the other perpendicular to it, $\zeta_\perp$. The component is then elliptical, and defined by:

- 139
$$f(\tilde{g}) = N(S, S_\perp)\exp\left(S\cos\tilde{g} + S_\perp\cos\tilde{g}_\perp\right)$$

with
$$S_\perp = \frac{\ln 2}{1 - \cos\left(\frac{\zeta_\perp}{2}\right)} \qquad \text{and} \qquad N(S, S_\perp) = 1 / \int_0^1 \exp(S_\perp t^2)(I_0(t) - I_1(t))dt$$

$$T = S_\perp(1-t^2) + S$$

4.6.8. Arbitrary texture correction

This kind of texture correction is not a model, and as such cannot be interpreted in terms of physically understandable parameters of texture. It only deserves the fitting possibility of diagrams that show textures, but ones that are not of interest or that cannot be measured (*e.g.* if not enough data have been acquired for this purpose). For instance, on a summed diagram when texture is not completely removed by the summation procedure, wherever no texture correction would induce unsatisfactory fit, one can use this correction in order to force the program to respect the actually observed intensities, this doing providing a better fit for starting cell parameters.

The correction simply consists in assigning arbitrary intensity values for the peaks in order that it respects observations.

4.7. OD Refinement reliability estimators

4.7.1. RP factors

The best solution found for f(g) is in most programs given for the minimum averaged reliability factors:

- 140
$$\overline{RP_x} = \frac{1}{I}\sum_i \sum_j \frac{\left|P^c_{\mathbf{h}_i}(\mathbf{y}_j) - P^o_{\mathbf{h}_i}(\mathbf{y}_j)\right|}{P^o_{\mathbf{h}_i}(\mathbf{y}_j)}$$

where:

$\mathbf{h}_i$, i = (1..I) Measured pole figures
$\mathbf{y}_j$, j = (1..J) Measured points of the pole figures

$$\begin{cases} \text{o : observed normalised} \\ \text{c : WIMV - recalculated normalised} \end{cases}$$

$P_{\mathbf{h}_i}(\mathbf{y}_j)$: Pole density at $\mathbf{y}_j$ on pole figure $\mathbf{h}_i$

If the RP factors are suitable for the refinement itself, they depend on the texture strength since they are not weighted by the density level, and consequently make the comparison of refinement's quality between samples somehow ambiguous [Chateigner 2000]. In other words, one should compare the refinement quality with RP factors, only for similar texture strengths. Furthermore, these factors can depend on the way the OD refinement is operated (Harmonics, WIMV ...), and depend on the grid used for the measurements.

One should distinguish several RP factors:

- Individual relative deviation factors:

- 141
$$RP^z_x(h_i) = \frac{\sum_{j=1}^{J}\left|\widetilde{P}^o_{h_i}(y_j) - \widetilde{P}^c_{h_i}(y_j)\right|}{\sum_{j=1}^{J}\widetilde{P}^z_{h_i}(y_j)}\ \theta\left(x, \widetilde{P}^o_{h_i}(y_j)\right)$$

with
$$\theta(x,t) = \begin{cases} 1 \text{ for } P_{\mathbf{h}_i}(\mathbf{y}_j) > x \\ 0 \text{ for } P_{\mathbf{h}_i}(\mathbf{y}_j) \le x \end{cases}$$

x = 0, ε, 1, 10 ...: criterion to estimate accuracy *versus* density level.

The value x is a criterion used to appreciate the quality of the refinement for the low and high density levels. We use x = 0.05 to reveal the global quality and x = 1 to show this quality for the density values higher than 1 m.r.d..

These individual factors help to detect if some pole figures are particularly badly reproduced after the refinement, in order to operate to a correction strategy.

- Averaged relative deviation factors:

- 142
$$\overline{RP}_x^z = \frac{1}{I}\sum_{i=1}^{I} RP_x^z(h_i)$$

These are simply the arithmetic average of the previous ones. They help in comparing results on different samples.

- Global relative deviation factors:

- 143
$$RP_x^z = \frac{\sum_{i=1}^{I}\sum_{j=1}^{J}\left|\tilde{P}_{h_i}^{o}(y_j) - \tilde{P}_{h_i}^{c}(y_j)\right|}{\sum_{i=1}^{I}\sum_{j=1}^{J}\tilde{P}_{h_i}^{z}(y_j)}\,\theta\left(x, \tilde{P}_{h_i}^{o}(y_j)\right)$$

Can serve the same uses as the average ones, but the averaging scheme differs.

4.7.2. RPw Surface weighted factors

Matthies, Vinel et Helming (1987) proposed reliability factors weighted by the surface area of the measured cells **y** of the pole figures. The surface-weighted averaged factors are calculated on the base of the pole densities by:

- 144
$$\overline{RP}_{Sx} = \sum_{i=1}^{I} \frac{\sum_{j=1}^{J} S_j \left|P_{\mathbf{h}_i}^{o}(\mathbf{y}_j) - P_{\mathbf{h}_i}^{c}(\mathbf{y}_j)\right|\theta\left(x, P_{\mathbf{h}_i}^{o}(\mathbf{y}_j)\right)}{\sum_{j=1}^{J} S_j P_{\mathbf{h}_i}^{o}(\mathbf{y}_j)}$$

where:

$$S_j = \Delta\alpha\left[\cos\left(\beta_j - \frac{\Delta\beta}{2}\right) - \cos\left(\beta_j + \frac{\Delta\beta}{2}\right)\right];\ S_0 = \pi\left(1 - \frac{\Delta\beta}{2}\right):\ \text{Surface element for } \mathbf{y}_j$$

Results [Chateigner 2000] with surface-weighted factors exhibit less variations with the texture strength than RPs, proving the efficiency of the weighting process, particularly for the higher texture strengths.

Here also the corresponding three different factors can be calculated:
- Individual weighted relative deviation factors [2]:

- 145
$$RPw_x^z(h_i) = \frac{\sum_{j=1}^{J} S_j \left| \tilde{P}_{h_i}^o(y_j) - \tilde{P}_{h_i}^c(y_j) \right|}{\sum_{j=1}^{J} S_j \tilde{P}_{h_i}^z(y_j)} \theta\left(x, \tilde{P}_{h_i}^o(y_j)\right)$$

- Averaged weighted relative deviation factors:

- 146
$$\overline{RPw}_x^z = \frac{1}{I} \sum_{i=1}^{I} RPw_x^z(h_i)$$

- Global weighted relative deviation factors:

- 147
$$RPw_x^z = \frac{\sum_{i=1}^{I} \sum_{j=1}^{J} S_j \left| \tilde{P}_{h_i}^o(y_j) - \tilde{P}_{h_i}^c(y_j) \right|}{\sum_{i=1}^{I} \sum_{j=1}^{J} S_j \tilde{P}_{h_i}^z(y_j)} \theta\left(x, \tilde{P}_{h_i}^o(y_j)\right)$$

4.7.3. RB Bragg-like factors

Another R-factor is interesting to calculate, since it corresponds to the Bragg R-factor of the Rietvelders. We then call it the Bragg-like standard deviation factor:

- Individual Bragg standard deviation factors:

- 148
$$RB_x^z(h_i) = \frac{\sum_{j=1}^{J} \left[\tilde{P}_{h_i}^o(y_j) - \tilde{P}_{h_i}^c(y_j) \right]^2}{\sum_{j=1}^{J} \tilde{P}_{h_i}^{z\,2}(y_j)} \theta\left(x, \tilde{P}_{h_i}^o(y_j)\right)$$

which also would stand if one replaces densities by intensities, since the normalising factor simplifies in the expression:

- 149
$$RB_x^z(h_i) = \frac{\sum_{j=1}^{J} \left[I_{h_i}^o(y_j) - I_{h_i}^c(y_j) \right]^2}{\sum_{j=1}^{J} I_{h_i}^{z\,2}(y_j)} \theta\left(x, \tilde{P}_{h_i}^o(y_j)\right)$$

- Averaged Bragg standard deviation factors:

- 150
$$\overline{RB}_x^z = \frac{1}{I} \sum_{i=1}^{I} RB_x^z(h_i)$$

- Global Bragg standard deviation factors:

- 151
$$RB_x^z = \frac{\sum_{i=1}^{I} \sum_{j=1}^{J} \left[I_{h_i}^o(y_j) - I_{h_i}^c(y_j) \right]^2}{\sum_{i=1}^{I} \sum_{j=1}^{J} I_{h_i}^{z\,2}(y_j)} \theta\left(x, \tilde{P}_{h_i}^o(y_j)\right)$$

4.7.4. RBw Bragg-like weighted factors

The previous factors can also be weighted by the surface elements:
- Individual weighted Bragg standard deviation factors:

- 152
$$RBw_x^z(h_i) = \frac{\sum_{j=1}^{J} S_j \left[\widetilde{P}_{h_i}^o(y_j) - \widetilde{P}_{h_i}^c(y_j)\right]^2}{\sum_{j=1}^{J} S_j \widetilde{P}_{h_i}^{z\,2}(y_j)} \theta\left(x, \widetilde{P}_{h_i}^o(y_j)\right)$$

- Averaged weighted Bragg standard deviation factors:

- 153
$$\overline{RBw}_x^z = \frac{1}{I} \sum_{i=1}^{I} RBw_x^z(h_i)$$

- Global weighted Bragg standard deviation factors:

- 154
$$RBw_x^z = \frac{\sum_{i=1}^{I} \sum_{j=1}^{J} S_j \left[\widetilde{P}_{h_i}^o(y_j) - \widetilde{P}_{h_i}^c(y_j)\right]^2}{\sum_{i=1}^{I} \sum_{j=1}^{J} S_j \widetilde{P}_{h_i}^{z\,2}(y_j)} \theta\left(x, \widetilde{P}_{h_i}^o(y_j)\right)$$

4.7.5. Rw weighted factors

The Rietveld-like R-factors or "intensity-weighted" which takes into account the normal Gaussian distribution standard deviation for each measured intensity, even shows less overall variation with the texture strength. It is a better indicator of the OD refinement reliability whan comparing different samples.

- Individual weighted standard deviation factors:

- 155
$$Rw_x^z(h_i) = \frac{\sum_{j=1}^{J} \left[w_{ij}^o I_{h_i}^o(y_j) - w_{ij}^c I_{h_i}^c(y_j)\right]^2}{\sum_{j=1}^{J} w_{ij}^z I_{h_i}^{z\,2}(y_j)} \theta\left(x, \widetilde{P}_{h_i}^o(y_j)\right)$$

- Averaged weighted standard deviation factors:

- 156
$$\overline{Rw}_x^z = \frac{1}{I} \sum_{i=1}^{I} Rw_x^z(h_i)$$

- Global weighted standard deviation factors:

- 157
$$Rw_x^z = \frac{\sum_{i=1}^{I} \sum_{j=1}^{J} \left[w_{ij}^o I_{h_i}^o(y_j) - w_{ij}^c I_{h_i}^c(y_j)\right]^2}{\sum_{i=1}^{I} \sum_{j=1}^{J} w_{ij}^z I_{h_i}^{z\,2}(y_j)} \theta\left(x, \widetilde{P}_{h_i}^o(y_j)\right)$$

with

$I^z_{h_i}(y_j) = \tilde{P}^z_{h_i}(y_j).N_{h_i}$: Diffracted intensity

N_{h_i} : Refined normalising factor

$w^z_{ij} = \frac{1}{\sqrt{I^z_{h_i}(y_j)}}$: Diffracted intensity weight

4.8. Texture strength factors

Once f(g) is satisfactorily obtained, one can calculate factors which give an estimate of the texture strength. Caution should be taken here when comparing samples on the base of overall texture strength parameters. Samples should have the same crystal symmetry and exhibit similar texture components.

4.8.1. Texture Index

4.8.1.1. ODF Texture Index

The first texture strength parameter is the so-called 'texture index' [Bunge 1982] (expressed in m.r.d.^{2} units):

- 158
$$F^2 = \frac{1}{8\pi^2}\sum_i [f(g_i)]^2 \Delta g_i$$

with $\Delta g_i = \sin\beta_\iota \, \Delta\beta \, \Delta\alpha \, \Delta\gamma$ is the OD cell volume.

This index varies from 1 (random powder) to infinity (perfect texture or single crystal). It represents the mean square value of the ODF.

While for discrete OD this factor is straightfully calculated, in the case of the generalised spherical harmonics model the calculation is based on the C^{mn}_λ coefficients:

- 159
$$F^2 = 1 + \sum_{\lambda=2}^{L}\left[\frac{1}{2\lambda+1}\right]\sum_{m=-\lambda}^{\lambda}\sum_{n=-\lambda}^{\lambda}\left|C^{mn}_\lambda\right|^2$$

4.8.1.2. Pole Figure Texture Index

To compare the texture strength of different samples, the texture index associated to the pole figures may be used. It is calculated similarly to the ODF Texture Index:

- 160
$$J^2_{\mathbf{h}} = \frac{1}{4\pi}\sum_i [P_{\mathbf{h}}(\mathbf{y}_i)]^2 \Delta\mathbf{y}_i$$

with $\Delta\mathbf{y} = \sin\vartheta_\mathbf{y} \, \Delta\vartheta_\mathbf{y} \, \Delta\varphi_\mathbf{y}$

4.8.2. Pole Figure and ODF strengths

Both texture (ODF) and pole figure indexes are expressed in units that are not homogeneous with the distribution density units (m.r.d.). To help comparison and interpretations, it is more convenient to compare the square roots of these values, i.e. the Texture Sterngth [Kock et al. 1998]:

- 161 $$F = \sqrt{F^2},$$

and the Pole figure strength:

- 162 $$J_h = \sqrt{J_h^2}$$

4.8.3. Texture Entropy

The second overall texture strength parameter is a measure of the texture disorder, evaluated by the calculation of the entropy:

- 163 $$S = \frac{1}{8\pi^2} \sum_i f(g_i) \ln f(g_i) \Delta g_i$$

4.8.4. Correlation between F^2 and S

Entropy and texture index are correlated, but it is not possible to obtain an analytical expression for this correlation.

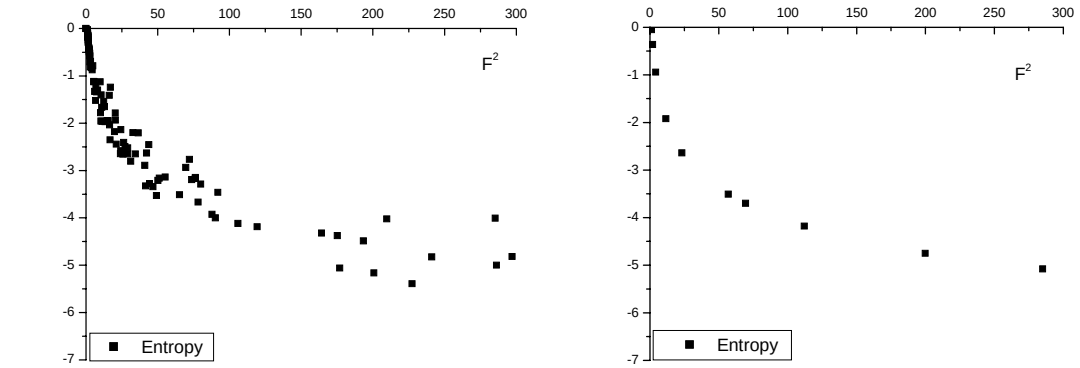

Figure 14: Entropy variation with Texture index. **a)**: for real samples, **b)**: for modelled textures

Looking at the variation of the entropy with the texture index (Figure 14), modelled textures are placed on a single line, meaning that S and F2 are univocally linking, though in a non-analytically solvable manner. Comparing real experiments (Figure 14a) with modelled

textures (Figure 14b) will help in identifying one refinement that may be ameliorated. Lastly, from Figure 14, one can experimentally see the relative evolutions of the texture strength parameters, which result from their analytical expressions: below a value of around 50 m.r.d.^{2}, S is varying much more than F^2, this latter being less efficient in revealing the texture strength. The reverse is true above 50 m.r.d.^{2}.

4.9. Texture programs

Many programs have been developed in order to treat QTA data.

4.9.1. Berkeley Texture Package (BEARTEX)

One of the most actually used is Beartex [Wenk et al. 1998] by the University of Berkeley, California. This package is dedicated to quantitative texture analyses starting from experimental raw pole figure sets. ODFs using regular 5°x5° and hexagonal grids can be calculated after pole figure corrections, and also simulation of standard ODFs and pole figures, modelling of macroscopic elastic tensors and elastic wave propagation, ODFs from single grain orientation mapping ...

4.9.2. Material Analysis Using Diffraction (MAUD)

With the development of experiments using 1D and 2D detectors, MAUD [Lutterotti et al., 1999] is more and more used. It allows the full pattern analysis by combining Rietveld and other codes including QTA. This program works for x-ray, and neutron data, both at monochromatic or energy-dispersive and time of flight experiments.

4.9.3. General Structure Analysis System (GSAS)

GSAS is a comprehensive system for the refinement of structural models to both x-ray and neutron diffraction data. The GSAS package can be used with both single-crystal and powder diffraction data (Rietveld analysis), even both simultaneously. Neutron data can be either from single-wavelength or time-of-flight instrumentation. Up to 99 different sets of data can be modelled using mixtures of up to 9 different phases.
GSAS has been created by Allen C. Larson and Robert B. Von Dreele of Los Alamos National Laboratory [Larson et Von Dreele, 2000].

4.9.4. preferred orientation package, Los Alamos (popLA)

The popLA [Mason, 1994] texture analysis software package, developed at Los Alamos by Fred Kocks and collaborators, provides a comprehensive treatment of material texture analysis by reducing texture data and using these data to predict important material properties. popLA is actually composed of two parts; 1) popLA - a general texture analysis and plotting package, and 2) LApp (Los Alamos polycrystal plasticity code) - a plasticity modelling code for investigating the effect of texture on plastic deformation. The distribution of crystal orientation is calculated and displayed by a wide variety of graphic formats for comparison with published results. Once distributions have been determined, standard methods are used to predict mechanical properties employed by industry to design and control efficient metals and ceramics processing techniques.
Data from three scattering techniques (x-ray, neutron, and electron diffraction) can be used by popLA to determine the ODF through the WIMV or harmonic formalisms. The 3-D orientation can then be used to generate a representative set of weighted orientations. The

weighed orientations serve as input to LApp, which predicts important elastic and plastic properties.

4.9.5. The Texture Analysis software (LaboTex)

The LaboTex [Pawlik et Ozga, 1999] software is the Windows 95/98/NT/Me/2000/XP tool for complex and detailed analysis of crystallographic textures. The program performs in user friendly form the different calculations and graphic analysis of Orientation Distribution Function (ODF), Pole Figures (PFs) and Inverse Pole Figures (IPFs).

4.9.6. Pole Figure Interpretation (POFINT)

POFINT [Chateigner 2002] is a simple MS-DOS based program developed in Turbo-Pascal. It provides simple tools for pole figure interpretation and corrections, file transformations for many experimental purposes, and without having necessity to work with large exploitation systems:

- Direct normalisation of pole figures
- Poles uncertainties after corrections
- Angle calculations between (hkl) and {h'k'l'} planes, and multiples
- Change crystal system, wavelength and conditions of existence
- Pole integration
- X-ray absorption coefficients and penetration depth
- Periodic table of the elements
- Defocusing curves: modifications for thin films, multilayers, fluorescence ...
- File transformations (Dubna, ILL, Beartex, LPEC, LLB, Mossbauer, INEL, Philips, Seifert, Socabim, Dosophatex, ...
- Intensity corrections
- Difference pole figures
- Reliability factors

This program allows the calculation of some parameters, useful for a direct pole figure and texture interpretation, in the case of bulk, thin film and multilayer specimen, and for eventual later analysis through other program packages. All Crystal systems, systematic extinctions and wavelengths are available.

4.9.7. Strong Textures (STROTEX and Phiscans)

This MS-DOS program [Chateigner, 2002a] is only to visualise pole figures in the simplest manner. Its advantage is that it can represent pole figures (and correct them) for all regular grids, but also for small angular steps. Its associate Phiscans allows pseudo-3D drawing, and pole integration to calculate orientation volumes.

4.9.8. STEREOPOLE

This program developed in Interactive Data Language (IDL) 6.0 under the GNU General Public Licence allows graphical comparisons of experimental and simulated pole figures (Salzmann et Resel 2004). It is able to evaluate epitaxial relationships for up to five different layers.

4.10. Limits of the classical texture analysis

Here comes the problem of the pole figure measurements, which has to be adapted to the samples to characterise. It started originally [Schulz 1949a et 1949b] with the use of a 4-circle diffractometer equipped with point detectors, and using a filtered (only) radiation. It became recently a necessity to use also a purer radiation as delivered by a monochromator [Wenk 1992], which was fairly new in the texturologists world. But one of the main problems still remained. One had to measure every single pole figure one after each other, doing the same $\chi\varphi$-scan for each of them. One way to avoid this time-consuming measurement was to build systems with more intense fluxes, as one can have using rotating anodes generators [Chateigner et al. 1997] or synchrotrons [Wenk et al. 1997]. Another way is to use multidetectors, usable on classical generators, like position sensitive (PSD), curved position sensitive (CPS) or 2-dimensional detectors (image plates or CCDs). The first use of position sensitive detectors was developed using neutron radiation [Bunge et al. 1982], were experimental time can be a crucial parameter. In this way, we demonstrated that quite a lot of the experimental time can be saved, also with a limited range in the pole figure coverage [Chateigner et al. 1997]. Using this approach the 5°x5° grid of the rotation around diffractometer axes are in some way deformed in the resulting pole figures [Heizmann et Laruelle 1986], after the localisation corrections. The ideal would be to measure those points that, after correction, result in a non-distorted 5°x5° coverage of the pole figure. However, for one incidence angle, this is feasible only for one of the pole figures, and whatever the grid used. And if several incidences are measured, the experiment needs more time and the use of a PSD becomes less interesting. The way to get rid of this deformation is to spline-interpolate the experimental points and recreate a non-distorted grid. All what is mentioned here is also true for an hexagonal grid [Matthies et Wenk 1992].

But another interest in using PSDs is revealed when the peak position or peak profile is of interest as we'll see in the Combined analysis paragraph. For instance, when internal stresses exist in the studied material, the peak position moves when the tilt angle changes, precluding any reliable measurement of the texture with a point detector, particularly if dealing with a well crystallised material for which diffraction peaks have low FWHMs.
On the other hand, for micro- or partially crystallised materials, peaks are so much broadened that some questions should be pointed out when working with a point detector:

- what are the relative contributions of each of the peaks probed by the detector ?
- what will be these contributions with the occurrence of defocusing or any other instrumental effect ?
- is the detector position representative of all the crystallites (or which part of the irradiated volume does it concern) ?
- how much the diffracted signal is perturbed by the amorphous contribution ?

Figure 15 is an example of a polypropylene diagram that exemplifies how these problems could perturb the results.

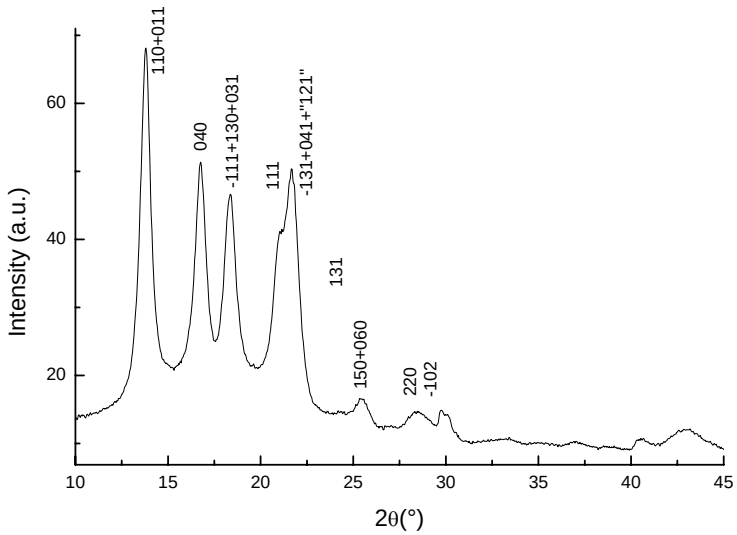

Figure 15: Example of an x-ray diffraction diagram for a plasma-treated polypropylene film.

There are actually three different manners to handle such a problematic analysis, all using a CPS or a PSD. The less elegant, and also less reliable, is to process a direct numerical integration of the peaks with background and amorphous subtraction using a linear interpolation. Since the amorphous part does not evolve linearly, it creates artefacts that act as a random contribution in the pole figures. This method should still be restricted to fully crystallised materials which exhibit individual enough peaks, for which it works nicely.
The second approach is to fit independent peaks with convenient shapes either in a whole pattern fitting procedure or on separated peaks or groups of peaks, *versus* the sample orientation. In this methodology, background and amorphous signals are subtracted with another fitted function [Aouinti et al. 2002]. Of course this approach assumes that the structure is perfectly known, a condition which is not always fulfilled.

The most elegant way at the present time is to resolve the structure and the texture in a combined approach as now developed for few years using TOF [Wenk et al. 1994, Matthies et al. 1997] and monochromatic neutron [Guilmeau et al. 2003], and x-rays [Cont et al. 2002, Morales et al. 2002] investigations.

5 Quantitative Microstructure Analysis (QMA)

5.1 Problematic

Important information on the microstructure may also be extracted from the width of the diffraction peaks. A diffraction peak can be considered as the convolution product of several effects: small size of the coherently diffracting domains, elastic microdistorsions (microstrains) due to linear and point defects, stacking faults, strain heterogeneities… From the peak profile point of view, this is expressed by Eq. - 11 in the direct space, or in the reciprocal space:

- 164 $$V_{\mathbf{h}}(\mathbf{k}) = L_{\mathbf{h}}(\mathbf{k}) \otimes G_{\mathbf{h}}(\mathbf{k})$$

We introduce here the **h** indice to take account of the eventual anisotropy (**h** planes dependency) of the peak broadening. Equation - 164 rewrites:

- 165 $$V_{\mathbf{h}}(\mathbf{k}) = \int L_{\mathbf{h}}(\mathbf{k} + 2\pi\,\Delta\mathbf{h})\; G_{\mathbf{h}}(\Delta\mathbf{h})\; d(\Delta\mathbf{h})$$

Δh being the variation in interreticular spacing due to microstrains and finite sizes. The contribution from microstrains $\varepsilon_{\mathbf{h}}$ produced by stresses are seen as relative variations of the d_{hkl} spacings:

- 166 $$\varepsilon_{\mathbf{h}} = -\,\Delta\mathbf{h} / \mathbf{h}$$

But diffraction only probes the mean values $\langle\varepsilon_{\mathbf{h}}\rangle$ of $\varepsilon_{\mathbf{h}}$ (average over all the equivalents of **h**). The quantity $\langle\varepsilon_{\mathbf{h}}\rangle$ is then the (hkl)-dependent macroscopic strain, which produces a peak shift under residual stress, and will be treated in paragraph 7 Residual Strain-stress Analysis (RSA) (this quantity corresponds to the $\langle\varepsilon^{I}_{\mathbf{h}}\rangle$ kind of residual stresses in paragraph 7.1 Strain definitions). The peak broadening represents the deviation of **Δh/h** from the macroscopic mean value of the strain, and is then $\langle\varepsilon^{2}_{\mathbf{h}}\rangle$ (and corresponds to the $\langle\varepsilon^{III}_{\mathbf{h}}\rangle$ kind of residual stresses in paragraph 7.1 Strain definitions). The contribution from $\langle\varepsilon^{2}_{\mathbf{h}}\rangle$ to the peak broadening is Gaussian while the contribution from finite sizes $\langle R_{\mathbf{h}}\rangle$ is Lorentzian-like:

- 167 $$G_{\mathbf{h}}(\mathbf{k}) = \frac{1}{\mathbf{h}\sqrt{2\pi\left\langle \varepsilon_{\mathbf{h}}^{2}\right\rangle}} \exp\left(\frac{-\Delta\mathbf{h}^{2}}{2\mathbf{h}^{2}\left\langle \varepsilon_{\mathbf{h}}^{2}\right\rangle}\right)$$

- 168 $$L_{\mathbf{h}}(\mathbf{k}) = \frac{3\left\langle R_{\mathbf{h}}\right\rangle}{4\pi}\left(\frac{1}{1+\frac{9}{16}\left\langle R_{\mathbf{h}}\right\rangle^{2}(\mathbf{k}-2\pi\mathbf{h})^{2}}\right)$$

The deconvolution of these effects is generally operated using one of the following methods: a Fourier transformation followed by a deconvolution (Warren-Averbach method), a modelling by analytical peaks followed again by a deconvolution (Integral Breadth method), then a development of the microstrains and sizes contributions into spherical harmonics from the Gaussian and Lorentzian contribution breadths can be applied to estimate anisotropic crystallite sizes and microstrains (Popa method).

Equations - 167 and - 168 can be expressed as functions of the Gaussian (β_{Gh}) and Lorentzian (β_{Lh}) peak broadening parts directly:

- 169
$$G_{\mathbf{h}}(\mathbf{k}) = \beta_{Gh}^{-1} \exp\left(\frac{-\pi z^2}{\beta_{Gh}^2}\right)$$

- 170
$$L_{\mathbf{h}}(\mathbf{k}) = \beta_{Lh}^{-1}\left(\frac{1}{1+\frac{\pi^2 z^2}{\beta_{Lh}^2}}\right)$$

with:

- 171
$$\beta_{Gh} = 2\tan\theta_{\mathbf{h}}\sqrt{2\pi\left\langle\varepsilon_{\mathbf{h}}^2\right\rangle}$$
$$\beta_{Lh} = \frac{2\lambda}{3\left\langle R_{\mathbf{h}}\right\rangle\cos\theta_{\mathbf{h}}}$$

for constant-wavelength diffraction methods ($z = 2\theta_{\mathbf{h}}$), and:

- 172
$$\beta_{Gh} = \lambda_{\mathbf{h}}\sqrt{2\pi\left\langle\varepsilon_{\mathbf{h}}^2\right\rangle}$$
$$\beta_{Lh} = \frac{\lambda_{\mathbf{h}}^2}{3\left\langle R_{\mathbf{h}}\right\rangle\sin\theta}$$

for energy-dispersive diffraction methods ($z = \lambda_{\mathbf{h}}$).

5.2 Isotropic and Anisotropic crystallite sizes and microstrains, Williamson-Hall approach [Langford et al. 1969]

This technique is based on individual profiles determination. It requires the determination of each line width of the experimental diagram, deconvoluted of g(x). Williamson et Hall [Langford & al. 1969] proposed:

- 173
$$\frac{\beta_{\mathbf{h}}\cos\theta}{\lambda} = \frac{1}{T_{\mathbf{h}}} + \varepsilon_{\mathbf{h}}\frac{\sin\theta}{\lambda}$$

in which $\beta_{\mathbf{h}}$ is the sample contribution to the peak width in 2θ, $T_{\mathbf{h}}$ the mean crystallite size and $\varepsilon_{\mathbf{h}}$ the mean microstrains, all in the **h** direction. If the crystallite sizes and microstrains are isotropic, the slope of the linear Equation - 173 provides the microstrain state

while the ordinate at origin gives the inverse of the mean size. For anisotropic crystallite sizes and/or microstrains, one has to plot one linear equation for each **h** direction in order to reconstruct the anisotropy. The main disadvantage of this technique occurs when the peaks are not easily separated (low symmetry phases, polyphased materials). The use of the Rietveld approach to extract the contributions is then preferred.

5.3 Anisotropic crystallite sizes, Popa approach [Popa 1998]

Considering $<R_{\mathbf{h}}>$ the mean crystallite size in the crystal direction **h**, we always can develop $<R_{\mathbf{h}}>$ in a convergent series of symmetrised spherical harmonics, the coefficients of which being refinable parameters. The symmetrised spherical harmonics are expressed by:

- 174

$$P_{2\ell}^{m}(x)\ \cos m\varphi \text{ or } P_{2\ell}^{m}(x)\ \sin m\varphi$$

$$\text{With } x = \cos\chi$$

The ℓ and m parameters follow some selection rules [Popa 1992] and the Legendre polynomia $P_{2\ell}^{m}(x)$ are:

- 175

$$P_{2\ell}^{m}(x) = \sqrt{\frac{(\ell+m)!}{(\ell-m)!}\left(\ell+\frac{1}{2}\right)}\frac{(-1)^{\ell-m}}{2^{\ell}\,\ell!}\left(1-x^{2}\right)^{\frac{-m}{2}}\frac{d^{\ell-m}(1-x^{2})^{\ell}}{dx^{\ell-m}}$$

The angles χ and φ are the co-latitude and azimuth angles respectively, in the sample co-ordinate system K_A. The $<R_{\mathbf{h}}>$ series is truncated at a number of terms which depends on the crystallite anisotropy. The first term R_0 corresponds to the mean crystallite size over all the **h** directions. Hereafter are the development of the series for the Laue groups.

$\bar{1}$: $<R_{\mathbf{h}}> = R_0 + R_1P_2^0(x) + R_2P_2^1(x)\cos\varphi + R_3P_2^1(x)\sin\varphi + R_4P_2^2(x)\cos2\varphi + R_5P_2^2(x)\sin2\varphi + ...$

- 176

2/m: $<R_{\mathbf{h}}> = R_0 + R_1P_2^0(x) + R_2P_2^2(x)\cos2\varphi + R_3P_2^2(x)\sin2\varphi + ...$

- 177

2/mmm: $<R_{\mathbf{h}}> = R_0 + R_1P_2^0(x) + R_2P_2^2(x)\cos2\varphi + ...$

- 178

4/m: $<R_{\mathbf{h}}> = R_0 + R_1P_2^0(x) + R_2P_4^0(x) + R_3P_4^4(x)\cos4\varphi + R_4P_4^4(x)\sin4\varphi + ...$

- 179

4/mmm: $<R_{\mathbf{h}}> = R_0 + R_1P_2^0(x) + R_2P_4^0(x) + R_3P_4^4(x)\cos4\varphi + ...$

- 180

$\bar{3}$: $<R_{\mathbf{h}}> = R_0 + R_1P_2^0(x) + R_2P_4^0(x) + R_3P_4^3(x)\cos3\varphi + R_4P_4^3(x)\sin3\varphi + ...$

- 181

$\bar{3}$m: $<R_{\mathbf{h}}> = R_0 + R_1P_2^0(x) + R_2P_4^0(x) + R_4P_4^3(x)\sin3\varphi + ...$

- 182

6/m: $\langle R_{\mathbf{h}} \rangle = R_0 + R_1 P_2^0(x) + R_2 P_4^0(x) + R_3 P_6^0(x) + R_4 P_6^6(x)\cos 6\varphi + R_5 P_6^6(x)\sin 6\varphi + \ldots$

- 183

6/mmm: $\langle R_{\mathbf{h}} \rangle = R_0 + R_1 P_2^0(x) + R_2 P_4^0(x) + R_3 P_6^0(x) + R_4 P_6^6(x)\cos 6\varphi + \ldots$

- 184

m3: $\langle R_{\mathbf{h}} \rangle = R_0 + R_1 K_4^1(x,\varphi) + R_2 K_6^1(x,\varphi) + R_3 K_6^2(x,\varphi) + \ldots$

- 185

m3m: $\langle R_{\mathbf{h}} \rangle = R_0 + R_1 K_4^1(x,\varphi) + R_2 K_6^1(x,\varphi) \ldots$

- 186

with:

- 187 $K_4^1(x,\varphi) = 0.3046972\ P_4^0(x) + 0.3641828\ P_4^4(x)\cos 4\varphi$

- 188 $K_6^1(x,\varphi) = -0.1410474\ P_6^0(x) + 0.527751\ P_6^4(x)\cos 4\varphi$

- 189 $K_6^2(x,\varphi) = -0.4678013\ P_6^2(x)\cos 2\varphi + 0.3153915\ P_6^6(x)\cos 6\varphi$

The refinable parameters are R_i's. The number of terms that must be used in formulae - 176 to - 186 can be determined by successive refinements starting from the isotropic case $\langle R_{\mathbf{h}} \rangle = R_0$. Terms are then added one by one until the corresponding fitted value becomes insignificant.

5.4 Microstrains, Popa approach [Popa 1998]

The microstrain series development for all the Laue groups is:

$\bar{1}$: $\langle \varepsilon_{\mathbf{h}}^2 \rangle E_{\mathbf{h}}^4 = E_1 h^4 + E_2 k^4 + E_3 \ell^4 + 2E_4 h^2 k^2 + 2E_5 \ell^2 k^2 + 2E_6 h^2 \ell^2 + 4E_7 h^3 k + 4E_8 h^3 \ell + 4E_9 k^3 h + 4E_{10} k^3 \ell + 4E_{11} \ell^3 h + 4E_{12} \ell^3 k + 4E_{13} h^2 k \ell + 4E_{14} k^2 h \ell + 4E_{15} \ell^2 k h$

- 190

2/m: $\langle \varepsilon_{\mathbf{h}}^2 \rangle E_{\mathbf{h}}^4 = E_1 h^4 + E_2 k^4 + E_3 \ell^4 + 2E_4 h^2 k^2 + 2E_5 \ell^2 k^2 + 2E_6 h^2 \ell^2 + 4E_7 h^3 k + 4E_8 k^3 h + 4E_9 \ell^2 h k$

- 191

2/mmm: $\langle \varepsilon_{\mathbf{h}}^2 \rangle E_{\mathbf{h}}^4 = E_1 h^4 + E_2 k^4 + E_3 \ell^4 + 2E_4 h^2 k^2 + 2E_5 \ell^2 k^2 + 2E_6 h^2 \ell^2$

- 192

4/m: $\langle \varepsilon_{\mathbf{h}}^2 \rangle E_{\mathbf{h}}^4 = E_1 (h^4 + k^4) + E_2 \ell^4 + 2E_3 h^2 k^2 + 2E_4 \ell^2 (k^2 + h^2) + 4E_5 k h (h^2 - k^2)$

- 193

4/mmm: $\langle \varepsilon_{\mathbf{h}}^2 \rangle E_{\mathbf{h}}^4 = E_1 (h^4 + k^4) + E_2 \ell^4 + 2E_3 h^2 k^2 + 2E_4 \ell^2 (k^2 + h^2)$

- 194

$\bar{3}$: $\langle \varepsilon_{\mathbf{h}}^2 \rangle E_{\mathbf{h}}^4 = E_1 (h^2 + k^2 + hk)^2 + 2E_2 \ell^2 (h^2 + k^2 + hk) + E_3 \ell^4 + (4/3) E_4 \ell (h^3 - k^3 + 3h^2 k) + (4/3) E_5 \ell (-h^3 + k^3 + 3k^2 h)$

- 195

$\bar{3}$R: $\langle\varepsilon_{\mathbf{h}}^2\rangle E_{\mathbf{h}}^4 = E_1(h^4+k^4+\ell^4) + 2E_2(h^2k^2+h^2\ell^2+\ell^2k^2) + 4E_3\ell hk(h+k+\ell) + 4E_4(kh^3+\ell k^3+h\ell^3) + 4E_5(hk^3+k\ell^3+\ell h^3)$

- 196

$\bar{3}$m1: $\langle\varepsilon_{\mathbf{h}}^2\rangle E_{\mathbf{h}}^4 = E_1(h^2+k^2+hk)^2 + 2E_2\ell^2(h^2+k^2+hk) + E_3\ell^4 + (4/3)E_4\ell(2h^3-2k^3+3h^2k-3hk^2)$

- 197

$\bar{3}$m1R: $\langle\varepsilon_{\mathbf{h}}^2\rangle E_{\mathbf{h}}^4 = E_1(h^4+k^4+\ell^4) + 2E_2(h^2k^2+h^2\ell^2+\ell^2k^2) + 4E_3\ell hk(h+k+\ell) + 4E_4[hk(h^2+k^2)+k\ell(k^2+\ell^2)+h\ell(h^2+\ell^2)]$

- 198

$\bar{3}$1m: $\langle\varepsilon_{\mathbf{h}}^2\rangle E_{\mathbf{h}}^4 = E_1(h^2+k^2+hk)^2 + 2E_2\ell^2(h^2+k^2+hk) + E_3\ell^4 + (4/3)E_4\ell(3h^2k+3hk^2)$

- 199

Hexagonal: $\langle\varepsilon_{\mathbf{h}}^2\rangle E_{\mathbf{h}}^4 = E_1(h^2+k^2+hk)^2 + 2E_2\ell^2(h^2+k^2+hk) + E_3\ell^4$

- 200

Cubic: $\langle\varepsilon_{\mathbf{h}}^2\rangle E_{\mathbf{h}}^4 = E_1(h^4+k^4+\ell^4) + 2E_2(h^2k^2+h^2k^2+k^2\ell^2)$

- 201

5.5 Stacking faults, Popa approach [Popa 1998]

From the anisotropic crystallite size model of Popa as is, the peak broadening encompasses also defects contributions that are not coming from the finite crystallite sizes. for instance stacking faults, point defects ...

The separation of the two effects is however possible if $\langle R_{\mathbf{h}}\rangle$ in Eq. - 168 is replaced by an effective radius:

- 202 $$\langle R_{\mathbf{h}}\rangle_{eff}^{-1} = \langle R_{\mathbf{h}}\rangle^{-1} + 2\,p_f P_{\mathbf{h}}$$

in which p_f is the faulting probability which has to be refinable, and $P_{\mathbf{h}}$ is a determined function of h which can be found in Warren [1969] for the face-centred cubic, body-centred cubic and hexagonal close-packed crystal systems.

6. Quantitative Phase Analysis (QPA)

6.1. Polycrystalline samples

Quantitative phase analysis can be performed on multi-phase samples using the formalism described by Hill et Howard [1987]. The general scattering cross-section for Bragg scattering is proportional to N/V, where N is the number of unit cells contributing to the scattering and V is the unit cell volume. The scale factor, S_Φ, in Equation - 24 is then proportional to N/V for each phase.

The weight fraction W_Φ of phase Φ can then be written as:

- 203

$$W_\Phi = \frac{S_\Phi Z_\Phi M_\Phi V_\Phi}{\sum_{i=1}^{N_\Phi} S_i Z_i M_i V_i}$$

where Z_Φ is the number of formula units per unit cell, M_Φ is the molecular weight of the formula unit, V_Φ is the unit cell volume and i is an index running over all N_Φ phases. It is worth noting that $S_\Phi V_\Phi$ is proportional to the number of diffracting unit cells (N_Φ) and $Z_\Phi M_\Phi$ is just the molecular weight of the unit cell, hence $S_\Phi V_\Phi Z_\Phi M_\Phi$ is proportional to the weight of the diffracting sample.

Figure 16 shows an example of fit of neutron data measured on a sample containing the superconducting $YBa_2Cu_3O_7$ and insulating Y_2BaCuO_5 phases. In this sample 35 % of superconductor and 65 % of insulator was determined using QPA.

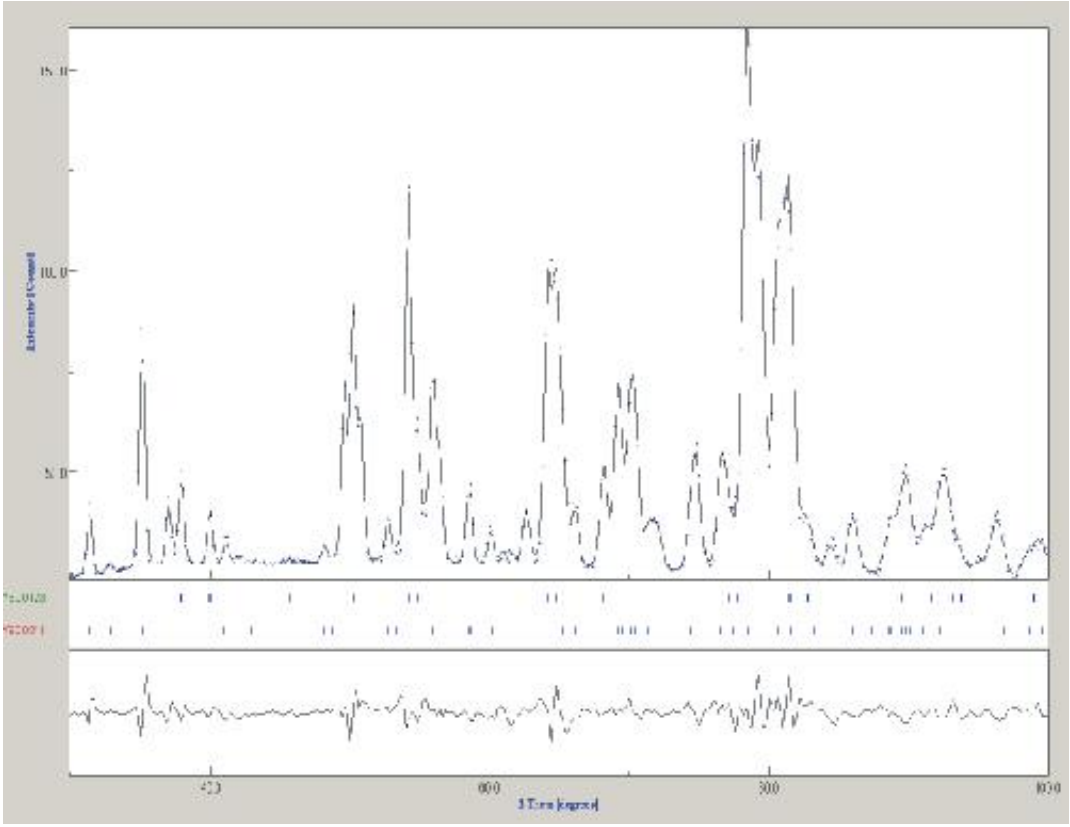

Figure 16: Example of a neutron diffraction diagram (dots) of a biphasic sample, and corresponding fit (line) using QPA as implemented in the MAUD program.

6.2. Amorphous-crystalline aggregates

Dealing with an amorphous and crystalline mixture gives rise to diagrams where amorphous oscillations close to the background superimpose with the diffracted lines. Le Bail [1995] showed, in the case of a SiO_2 partially crystallised ensemble, that Equation - 203 still can be used to determine the volume fraction of the amorphous and crystalline phases, provided that:

- the amorphous phase is declared with a unit-cell
- the crystallite sizes of the amorphous phase are reduced to approximately the dimension of the unit-cell, thereby suppressing the interferences of the scattered signal, in order that diffusion solely remains.

Not all the structures can be modelled using this approach, and it is better to start with the close crystalline structure. Also, when some preferred orientation is present in the crystalline phase(s), the crystalline volume fractions are biased, and a physically understandable QTA has to be practiced.

Figure 17 shows a refinement example on a fluorapatite sample irradiated under 10^{13} Kr cm^{-2}, measured using x-rays. Textural effects explain the imperfect reproduction of the diffracted peaks.

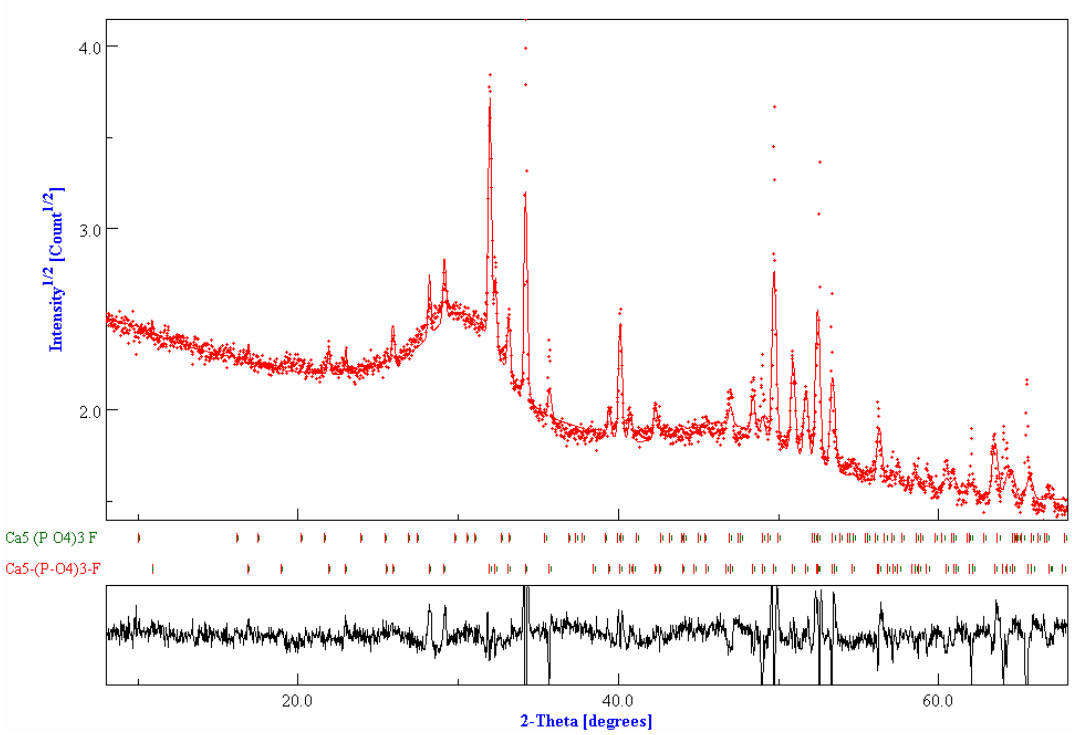

Figure 17: QPA refinement example of an x-ray diagram measured on a 85 % amorphous fluorapatite sample. Refinement operated in MAUD, Miro et al. (2004).

7 Residual Strain-stress Analysis (RSA)

Diffracting planes are used as strain gauge. Stresses are then calculated via continuum mechanics equations. The formalism of these methods is extensively described in the works by Cullity [1978], Maeder [1986], Noyan et Cohen [1987], Noyan et al. [1995], Hauk [1997].

7.1 Strain definitions

The total elastic strain for a grain at the position **X** in the sample can be expressed in the sample reference frame K_A by:

- 204
$$\boldsymbol{\varepsilon}(\mathbf{X}) = \boldsymbol{\varepsilon}^{\mathbf{I}} + \boldsymbol{\varepsilon}^{\mathbf{II}}(\mathbf{X}) + \boldsymbol{\varepsilon}^{\mathbf{III}}(\mathbf{X})$$

$\boldsymbol{\varepsilon}^{\mathbf{I}}$ is the macroscopic strain (first order) averaged over all grains within the macroscopic irradiated volume V_d. This macroscopic strain is induced by macroscopic stresses σ^I (Figure 18). $\boldsymbol{\varepsilon}^{\mathbf{II}}$ is the intergranular strain (2^{nd} order) which characterises the strain deviation from the macroscopic value ε^I for a particular grain. Intergranular strains can be present in the material for several reasons, elastic anisotropy giving rise to ε^{IIe}, thermal anisotropy ε^{IIti}, plastic anisotropy ε^{IIpi}. $\boldsymbol{\varepsilon}^{\mathbf{III}}$ is defined as the position dependent deviations from the average macroscopic strain of the crystal. These latter are often referred as microstrains, with an average value over one crystallite being zero. Microstrains are accessible by a profile analysis of the diffraction peaks.

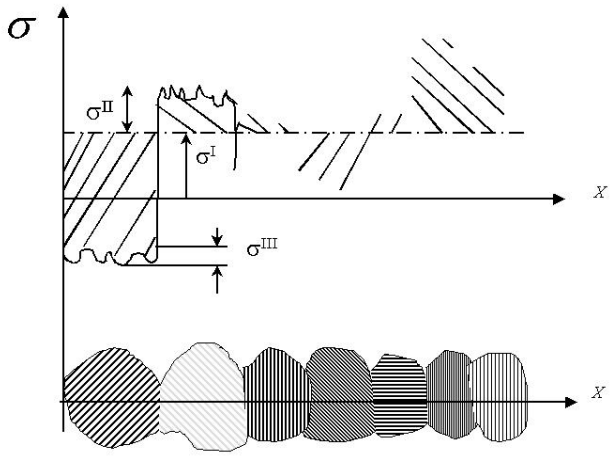

Figure 18: Phenomenological classification of internal stresses. σ^I, σ^{II} and σ^{III} are respectively macro-, meso- and microscopic stresses. One could have drawn the same diagram with strain types ε^I, ε^{II} and ε^{III} respectively.

Diffraction measures the mean interplanar spacing $\langle d(hkl,\phi,\psi)\rangle_{V_d}$ averaged for the diffracting grains which possess a scattering vector normal to the (hkl) planes in V_d. The average strain $\varepsilon_{\phi\psi}$ or $\varepsilon_{\mathbf{h}}(\mathbf{y})$ is measured in the direction $\mathbf{y} = (\phi,\Psi)$ for the crystalline planes $\mathbf{h} = \{h,k,l\}$ defined in the sample coordinate system $K_A = (\mathbf{X}, \mathbf{Y}, \mathbf{Z})$. The angles are the azimuth ϕ and the colatitude ψ. Note that the ψ axis is the tilt angle as used in texture experiments, but may also correspond to the asymmetry angle (2θ-ω) using position sensitive detectors. The ϕ angle is the same as φ in texture analysis:

$$\left\langle \varepsilon_{\mathbf{h}}(\mathbf{y}) \right\rangle_{V_d} = \frac{1}{V_d}\int_{V_d}(\varepsilon_{33}^{I}+\varepsilon_{33}^{II}+\varepsilon_{33}^{III})dV$$

$$= (\varepsilon_{11}^{I}\cos^2\phi + \varepsilon_{12}^{I}\sin 2\phi + \varepsilon_{22}^{I}\sin^2\phi - \varepsilon_{33}^{I})\sin^2\psi + \varepsilon_{33}^{I} +$$

- 205

$$(\varepsilon_{13}^{I}\cos\phi + \varepsilon_{23}^{I}\sin\phi)\sin 2\psi + \frac{1}{V_d}\int_{V_d}(\varepsilon_{33}^{IIe}+\varepsilon_{33}^{IIti}+\varepsilon_{33}^{IIpi})dV$$

$$= \frac{\left\langle d(hkl,\phi,\psi)\right\rangle_{V_d} - d_0(hkl)}{d_0(hkl)}$$

where d_0 is the unstrained lattice plane spacing of the {hkl} planes. d(hkl) and d_0 are accessed via the $\theta_{\phi\psi}$ and θ_0 angular positions of the corresponding diffraction peaks through Bragg's law.

7.1. ε_{33} strain determination

Only one main strain, ε_{33}, is measured, and the other elements of the strain tensor are deduced by means of restrictive hypotheses. The axis 3 refers to the axis perpendicular to the sample surface.

7.1.1 Isotropic polycrystalline sample

Using linear elasticity theory:

- 206

$$\varepsilon_{33} = -\frac{\nu}{1-\nu}(\varepsilon_{11}+\varepsilon_{22})$$

ν: Poisson's ratio.

Hypotheses:

- surface equilibrium conditions: $\sigma_{i3} = 0$, i = 1,2,3
- shear strains are equal to zero (at least ε_{12}, otherwise ε_ϕ cannot be constant in the plane)
- the stress free interreticular distance of the diffracting planes is known (otherwise ε_{33} cannot be measured !)

With isotropic in-plane strains (fibre textures):

- 207

$$\varepsilon_{33} = -\frac{2\nu}{1-\nu}\varepsilon_\phi$$

ε_ϕ: strain in any in-plane direction.

Measuring ε_{33} and knowing ν one can obtain ε_ϕ.

7.1.2 Single crystal

- 208

$$\varepsilon_{33} = -\left(\frac{C_{31}}{C_{33}}\varepsilon_{11} + \frac{C_{32}}{C_{33}}\varepsilon_{22}\right)$$

C_{ij}: elastic constants in the sample frame with the matrix notation.

And the same hypotheses remain.

With isotropic in-plane strains:

- 209
$$\varepsilon_{33} = -\left(\frac{C_{31}+C_{32}}{C_{33}}\right)\varepsilon_{\phi}$$

Measuring ε_{33} and knowing C_{ij} one can obtain ε_{ϕ}.

7.2. Complete strain tensor determination

7.2.1 Isotropic polycrystalline samples

7.2.1.1 triaxial stress state

In the case of polycrystalline samples, the whole strain tensor is obtained thanks to the so-called $\sin^2\psi$ method with the only hypothesis $\sigma_{33} = 0$. This method is based on the measurement of the variations of a {hkl} plane family diffraction peak position ($2\theta_{hkl}$) as a function of the two Euler angles, the azimuth ϕ and the colatitude ψ. Note that the ψ axis is the tilt angle as used in texture experiments, but may also correspond to the asymmetry angle (2θ-ω) using position sensitive detectors.
Using linear elasticity theory, one obtains the general $\sin^2\Psi$ relation in the case of a triaxial stress state:

- 210
$$\varepsilon_{\phi\psi} = \frac{1}{2}S_2(\sigma_{\phi}\sin^2\psi + \tau_{\phi}\sin 2\psi) + S_1(\sigma_{11}+\sigma_{22})$$

with $\sigma_{\phi} = \cos^2\phi\,\sigma_{11} + \sin^2\phi\,\sigma_{22} + \sin 2\phi\,\sigma_{12}$, the main stress in the ϕ direction and $\tau_{\phi} = \sigma_{13}\cos\phi + \sigma_{23}\sin\phi$, the shear stress in the ϕ direction. The S_1 and S_2 "radiocrystallographic" elastic constants can be expressed as a function of the "radiocrystallographic" Young's modulus and Poisson's ratio relative to the considered {hkl} family by $\frac{1}{2}S_2 = (1+\nu)/E$ and $S_1 = -\nu/E$. Applying relation - 210 to at least three different values of ϕ, one gets the whole stress tensor.

7.2.1.2 Biaxial stress state

When shear stresses are negligible (biaxial stress state $\tau_{\phi} = 0$), $\varepsilon_{\phi\psi}$, and consequently $\ln(1/\sin\theta)$, depend linearly upon $\sin^2\psi$:

- 211
$$\ln(1/\sin\theta_{hkl}) = \frac{1}{2}S_2(\sigma_{\phi}\sin^2\psi) + S_1(\sigma_{11}+\sigma_{22}) + \ln(1/\sin\theta_0)$$

7.2.1.2 Uniaxial stress state

Finally, if the in-plane stresses are isotropic ($\sigma = \sigma_{11} = \sigma_{22} = \sigma_{\phi}$), Eq. - 211 rewrites:

- 212
$$\ln(1/\sin\theta_{hkl}) = \frac{1}{2}S_2(\sigma\sin^2\psi) + 2S_1\sigma + \ln(1/\sin\theta_0)$$

Plotting $\ln(1/\sin\theta_{hkl})$ *versus* $\sin^2\psi$, one obtains a straight line which slope is proportional to σ and the intercept allows to determine the stress-free distance d_0. This parameter gives important information on the microstructure of the material compared to the bulk one (d_b): a value of d_0 smaller than d_b indicates a structure with vacancies or smaller substitution atoms, or a stretched film, whereas a value of d_0 larger than d_b denotes a large amount of interstitials, bigger substitution atoms and impurities, or a compressively stressed film.

7.2.2 Single crystal sample

In the case of single crystal samples, the so called "metric tensor method" is used, with or without the $\sigma_{33} = 0$ hypothesis. Only the guideline of this method is given here; for details on the theoretical development, the reader can refer for example to the works from Gergaud [1992] and Auzary *et al*. [1997].

On the basis of the crystal coordinate system $K_B = (\mathbf{e_1}, \mathbf{e_2}, \mathbf{e_3})$ one writes a vector $\mathbf{u} = \Sigma\, x_i\mathbf{e_i}$ with $|\mathbf{u}|^2 = g_{ij}x_ix_j$ where g_{ij} is the fundamental metric tensor of the basis $\mathbf{e_i}$ ($g_{ij} = \mathbf{e_i}.\mathbf{e_j}$). In the small deformation theory of continuum mechanics, the fundamental measure of deformation is defined by $d\ell^2 - d\ell_0^2 = 2\varepsilon_{ij}\, dx_i\, dx_j$ with $d\ell_0^2 = g_{ij}(x)\, dx_i\, dx_j$ and $d\ell^2 = g_{ij}(x)\, dx_i\, dx_j$ ($d\ell_0$ and $d\ell$ are elementary distances before and after deformation). Rotating from the **X**, **Y**, **Z** axes of the sample to the $\mathbf{e_1}$, $\mathbf{e_2}$, $\mathbf{e_3}$ base of the crystal, one can write $E_{ij} = g_{ij} - g_{ij}^0$ where E_{ij} is the strain tensor in the crystal axis system and g_{ij} and g_{ij}^0 are the metric tensors related to the strained and unstrained crystal respectively. The general case is rather complicated but cubic or orthorhombic cases are quite simple.

7.2.2.1 Cubic and orthorhombic crystal systems

In the case of a cubic crystal system, $E_{ij} = a_0^2\delta_{ij}$ (a_0 = lattice parameter) and $g_{ij}^0 = a_0^2\delta_{ij}$, then $g_{ij} = a_0^2(2\varepsilon_{ij} + \delta_{ij})$ which is the metric tensor related to the deformed crystal basis. The angular position of the x-ray diffraction peak gives the interreticular distances d_{hkl} that are directly related to the reciprocal lattice. Therefore it is more appropriate to write $d_{hkl}^{-2} = g^{ij}h_i h_j$, where g^{ij} is the metric tensor related to the reciprocal basis of the crystal. g^{ij} is obtained from g_{ij} by a matrix inversion and gives $g^{ij} = a_0^{-2}(\delta_{ij} - 2\varepsilon^{ij})$, which leads for the orthorhombic crystal to $\varepsilon_{ij} = \frac{1}{2}(\delta_{ij} - a_{0i}a_{0j}g^{ij})$ where a_{0i} are the lattice parameters of the orthorhombic structure. The metric tensor of the deformed bases is obtained from the x-ray diffraction measurements; therefore, at least six peaks are required in the general case.

7.2.2.2 Stress tensor

From Hooke's law and measured strains, the stress tensor can be determined:

$$\sigma_{ij} = C_{ijk\ell}\,\varepsilon^{k\ell}$$

$$\varepsilon^{k\ell} = S_{ijk\ell}\,\sigma^{ij}$$

where $C_{ijk\ell}$ are the elastic stiffnesses and $S_{ijk\ell}$ the elastic compliances of the single crystal.

As seen above the determination of the strain tensor $\varepsilon^{k\ell}$ requires the knowledge of the lattice parameters a_{0i} (g_{ij}^0) of the undeformed (stress-free) lattice that are generally unknown. Therefore a rather reasonable assumption is made: the outer surface of the sample is in equilibrium which gives $\sigma_{33} = 0$ (it is postulated that no gradient on σ_{33} exists and thus $\sigma_{33} = 0$ all along the probed direction of the sample). The stress tensor is then calculated using the lattice parameters of the bulk (or powder) material following an algorithm where σ_{33} must reach the zero value by an iterative calculation as a function of new lattice parameters.

7.3 Textured samples

7.3.1. Generalities

Non-linearity in the $\sin^2\Psi$ relation is observed due to stress gradients or texture (Maeder, 1986). The $\sin^2\psi$ method, or any other methods like the $\cos^2\varphi$ become then non applicable as is.

An easy way to solve this problem, in the case of strong and sharp textures, is to use the "crystallite group method" (Willemse et al. 1982, Hauk et Vaessen 1985): interreticular strains are measured on several well-oriented crystalline planes (corresponding to specific orientation components) and related to the stress tensor via the single crystal elastic constants (Clemens et Bain 1992, Badawi *et al*. 1994, Labat *et al*. 2000). But this approach does not take into account the volume fraction of crystallites actually diffracting in each orientation, a quantity that can be estimated using the ODF.

From a perfectly isotropic powder of Young's modulus E and Poisson coefficient G to a perfect single crystal of elastic compliances $S_{ijk\ell}$, a broad range of mechanical behaviour can be encountered in textured samples. The way the anisotropy in elastic constants can be taken into account is still a long debate. Most of the investigations are dealing with the so-called diffraction stress factors, $F_{ij}(\phi,\psi,\mathbf{h})$, which take into account the deviations of the elastic constants from the single crystal case (Hauk 1997, Welzel et Mittemeijer 2003). This approach needs the ODF to be determined in order to provide a correct average of the diffraction stress factors, and is barely used in the literature.

Another approach is the use of a simulation for the calculation of the macroscopic elastic tensors as they are exhibited by the oriented polycrystal. Knowing the ODF and the elastic compliance or stiffness of the single crystal, several models have been developed to calculate the real macroscopic tensor of the polycrystal (see § 10.2.3.). Strains can then be deduced from the measurements involving different sample orientations (in fact the texture measurements) and the stresses deduced from the simulated macroscopic constants.

7.3.2. Non-linear least-squares fit

For any stress state, and also for non textured specimen, the use of fitting procedures helps the analysis. Non-linear least-squares fit have been developed for residual stress analysis of random samples (Press et al. 1986), but it became an absolute necessity when dealing with anisotropic samples. It that case, strains are changing according to the texture, and it is by far more powerful to adjust the calculated strains to the measured ones. The function used for the minimisation is:

- 214

$$\chi^2 = \sum_i {w_i}^2 \left[\varepsilon_i^{calc}(S_{ijk\ell}^M, \mathbf{h}, \mathbf{y}) - \varepsilon_i^{meas}(S_{ijk\ell}^M, \mathbf{h}, \mathbf{y}) \right]^2$$

in which the number of measured strains is i, and w_i is the weight associated to the different measured strains, liked to the standard deviation obtained in the refinement. This approach is very flexible relative to the number of strains that one can measure. For instance, when strong texture occurs, not all the peaks give a contribution at all the necessary ψ orientations, which makes the $\sin^2\psi$ method vanishing. Even in this case the refinement can be a solution.

7.3.3. Strain and stress distribution functions

From the measurement of the strains in all the sample directions, $\varepsilon^{meas}(\mathbf{h},\mathbf{y})$, the representation of the strain distribution (SD) is straightforward. But only if the strains can be measured for all the directions, which for strong textures is not always possible. In this latter case one has to rely on the values recalculated from the refinement, $\varepsilon^{meas}(\mathbf{h},\mathbf{y})$. However, such values imply that either the macroscopic elastic coefficients ($S_{ijk\ell}{}^{M}$ or $C_{ijk\ell}{}^{M}$) have been refined together with the stresses, or that a modelling of the macroscopic stresses has been operated. Such modelling of the macroscopic elastic constants are detailed in paragraph 10.

8 X-ray Reflectivity (XRR)

8.1 Introduction

X-ray reflectivity has become an invaluable tool to study the structure and the organisation of materials which are grown layer by layer by the bottom up approach in thin films and hetero-structures at the submicronic and atomic scales [Stoev et Sakurai 1999, Bowen et Wormington 1993, Van den Hoogendorf et de Boer 1994, Dietrich et Haase 1995, Deutsch et Ocko 1998, Robinson et Tweet 1992]. In thin film material research, the trend is to design solid films of increasing complexity having specific properties for technical applications. The perfection of layered super-structures can be defined by the quality of the interfaces, the control of the thickness, crystallinity, voids or various defects which may appear during the growing process. In particular, the roughness of the interfaces is of crucial importance for many technological applications and it is a parameter which must be determined to appreciate the quality of the interfaces. In addition it is also of fundamental interest to discriminate between a morphological roughness and a composition gradient at the interface.

8.2 The x-ray refractive index

The interaction of x-rays with matter can be described in a classical way in a first approximation by a refractive index which characterises the refraction in a specific media. A very simple classical model in which an electron of the material is considered to be accelerated by the x-ray field leads to the following expression for the refractive index for x-ray radiation:

- 215
$$n = 1 - \delta - i\beta$$

where the imaginary part of the index accounts for the absorption in the material. The values of δ and β (both positives) depend on the electron density ρ_Φ of the material which can be expressed by:

- 216
$$\rho_\Phi = \sum_k \frac{Z_k + f_k^{'} + if_k^{''}}{V_\Phi}$$

where V_Φ is the unit cell volume of phase Φ, z_k is the number of electrons of atom *k* in the unit cell, *f'* and *f''* are the real and imaginary parts of the anomalous scattering factor for the specific energy of the incident radiation λ. The sum is performed over all the atoms of the unit cell. It is possible to show:

- 217
$$\delta = \frac{r_e}{2\pi}\lambda^2 \sum_k \frac{(Z_k + f_k')}{V_\Phi} = \frac{r_e}{2\pi}\lambda^2 \rho_\Phi$$

and

- 218
$$\beta = \frac{r_e}{2\pi}\lambda^2 \sum_k \frac{f''}{V_\Phi}$$

with $r_e = 2.81310^{-6}$ nm being the classical radius of the electron.

8.3 The critical angle of reflection

For x-ray radiation, the refractive index of a material is slightly less than 1 [Compton 1923]. Crossing an interface from air (n = 1) to a given material (n < 1), it is possible to totally reflect the beam if the incident angle θ is small enough. In order to observe this "total external reflection" of x-rays, the incident angle must be smaller than the critical angle θ_c defined by:

- 219
$$\cos\theta_c = n = 1 - \delta$$

Since n is close to unity, this angle is very small and a Taylor approximation in θ_c yields:

- 220
$$\theta_c^2 = 2\delta = \frac{r_e \lambda^2}{\pi} \rho_\Phi$$

8.4 Fresnel formalism (Specular reflectivity)

The specular reflectivity is conventionally defined as the ratio:

- 221
$$R(\theta) = \frac{I(\theta)}{I_0}$$

where I(θ) is the intensity reflected along the direction θ from the surface and I_0 the intensity of the incident beam at θ from the surface. If the electron density can be considered as a continuous media (small angles of incidence), refraction/reflection at interfaces can be treated as a classical problem of electromagnetic waves. From continuity equations of the electromagnetic field at interfaces, the classical Fresnel relationships are obtained which give the amplitude of the reflection coefficient for the (s) and (p) polarisation. The reflectivity is then the square modulus of this coefficient:

- 222
$$R(\theta) = rr^* = \left| \frac{\theta - \sqrt{\theta^2 - \theta_c^2 + 2i\beta}}{\theta + \sqrt{\theta^2 - \theta_c^2 + 2i\beta}} \right|^2$$

This expression does not depend on the field polarisation. For specular reflectivity (identical incoming and outcoming angles), we obtain after introduction of the wave vector transfer $\mathbf{q}=(0,0,q_z)$ with $q_z = 4\pi\sin\theta / \lambda$:

- 223
$$R(\mathbf{q}) = \left| \frac{q_z - \sqrt{q_z^2 - q_c^2 + \frac{32i\pi^2\beta}{\lambda^2}}}{q_z + \sqrt{q_z^2 - q_c^2 + \frac{32i\pi^2\beta}{\lambda^2}}} \right|^2 \delta q_x \delta q$$

For instance, the reflectivity curve of a flat silicon is equal to 1 below the critical wave vector transfer which is q_c=0.0317Å^{-1}. After this value, the deviation from unity is due to the absorption in the material which plays a major role close to $q = q_c = \frac{4\pi \sin\theta_c}{\lambda} \approx \frac{4\pi\theta_c}{\lambda}$. When $q_z > 3q_c$, the reflectivity rapidly becomes $R(q_z) = \frac{q_c^4}{16 q_z^4}$.

8.5 Surface roughness

One can realize that rough surfaces will be less reflecting than ideally flat surfaces. The roughness can be understood statistically with the help of the moments of the distribution of altitudes z(x,y). The second moment of the distribution is:

- 224
$$\sigma^2 = \left\langle \left(z(x,y) - \bar{z}\right)^2 \right\rangle = \int dz p(z) \left(z(x,y) - \bar{z}\right)^2$$

The square root of this quantity is the roughness σ of the surface. The surface roughness reduces the specular reflectivity by a Debye-Waller-like factor. When the correlation length of the height fluctuations is not very large:

- 225
$$R^{rough}(q_z) = R(q_z) \exp(-q_{z,0} q_{z,1} \sigma^2)$$

where $q_{z,0}$ and $q_{z,1}$ are the wave vector transfers in air and in the material. Conversely [Croce et Névot 1976, Névot et Croce 1980, de Boer 1994]:

- 226
$$R^{rough}(q_z) = R(q_z) \exp(-q_{z,0}^2 \sigma^2)$$

A similar effect is produced by a flat graded layer in which the electron density is represented by an error function of half width σ.

8.6 Matrix formalism (specular reflectivity)

When the wave propagates in a heterogeneous medium presenting regions of different electron densities, it is not possible to directly use the Fresnel coefficients. The calculation is performed by applying the boundary conditions of the electromagnetic fields at each interface [Abeles 1950, Parratt 1954, Born et Wolf 1980]. In the dynamical theory of reflection multiple reflections are taken into account at each interface and the reflected and transmitted electric fields are usually presented in a matrix form [Abeles 1950, Vidal et Vincent 1994, Gibaud 1999].

For a single layer (medium 1) of thickness h deposited on a substrate (medium 2), the reflection coefficient at the air (medium 0) / layer interface is:

- 227
$$r = \frac{r_{0,1} + r_{1,2} e^{-2ik_{z,1}h}}{1 + r_{0,1} r_{1,2} e^{-2ik_{z,1}h}}$$

with $r_{0,1}, r_{1,2}$ the Fresnel coefficients at interfaces 0/1 and 1/2, and $k_{z,1}$ the z component of the wave vector in medium 1. The $r_{0,1}r_{1,2}$ factor in the denominator expresses deviation from unity which comes from multiple reflections in the material. The reflectivity is:

- 228
$$R^{flat} = \frac{r_{0,1}^2 + r_{1,2}^2 + 2r_{0,1}r_{1,2}\cos 2k_{Z,1}h}{1 + r_{0,1}^2 r_{1,2}^2 + 2r_{0,1}r_{1,2}\cos 2k_{Z,1}h}$$

The existence of cosine terms in the reflectivity clearly indicates that the reflectivity does present periodic oscillations in reciprocal space defined as :

$$2k_{z,1}h = q_{z,1}h = 2p\pi$$

The oscillations are the result of constructive interference between the reflected waves at interfaces 1 and 2 and their period gives the thickness of the film.

8.7 Born approximation

X-ray reflectivity curves can be analyzed in the framework of kinematical theory, the so-called Born approximation, as far as the reflected intensity is small compared to that of the incident beam. In the first Born approximation the reflectivity can be written as [Als Nielsen 1985, Hamley et Pedersen 1994, Daillant et Bélorgey 1992]:

- 229
$$R(q_z) = r.r^* = R_F(q_z)\left|\frac{1}{\rho_s}\int_{-\infty}^{+\infty}\frac{d\rho(z)}{dz}e^{iq_z z}dz\right|^2$$

where $R_F(q_z) = (4\pi r_e \rho_s)^2 / q_z^4$ is the Fresnel reflectivity of the substrate and ρ_S its electron density.

The expression - 229 is not rigorous but can be easily handled in analytical calculations [Reiter 1994, Russel 1996, Vignaud et al. 1998]. In addition, following the Wiener-Kintchine theorem:

- 230
$$\frac{R(q_z)}{R_F(q_z)} = TF[\rho'(z) \otimes \rho'(z)]$$

so that the data inversion gives the autocorrelation function of the first derivative of the electron density.

8.8 Electron density profile

For two or more layers deposited on a substrate the analytical expression of the reflectivity becomes tedious. The reflectivity curves are showing typical shape with more or less rapid oscillations and beatings due to interference phenomena. The quantitative analysis made via the matrix technique or by inversion of Equation - 229 leads to the determination of the electron density profile (EDP) along z using specular reflectivity. The EDP provides all

the information about the macroscopic composition of the film in the direction perpendicular to its surface, including the roughness at each interface. The EDP is generally not unique due the loss of the phase through the media and that only a very good knowledge of the sample composition allows the discrimination between different profiles. Similar examples can be found in the work of Banerjee *et al.* [2002], where the comparison of the matrix technique with the Distorted Wave Born Approximation (DWBA) is used to determine the EDP.

8.9 Multilayers reflectivity curves

The reflectivity curve of a multilayer exhibits Bragg peaks separated by Kiessig fringes [Stearns 1992, Baumbach et Mikulik 1999]. The q distance between two Bragg peaks is inversely proportional to the period of the multilayer and the one between Kiessig fringes gives the thickness of the film (one should expect N-2 fringes between two Bragg peaks, N being the number of repeated bilayers).

8.10 Correction for irradiated area

The fact that the reflectivity can be less than 1 below the critical angle is related to a surface effect. At very small angles, it frequently happens that the sample surface does not cross all the beam, so that only part of the incident intensity is reflected. A correction must then be applied to describe this part of the reflectivity curve, provided a monitored sample shape [Gibaud *et al.* 1993].

9 Combined Structure-Texture-Microstructure-Stress-Phase-Reflectivity Analysis

9.1: Problematic

Analysis by diffraction/scattering of rays is nowadays more and more confronted with a major problem: physical-chemists elaborate samples of growing complexity (thin or massive heterostructures, polyphased materials ...) and want to non-destructively know the most possible about their sample's characteristics.

Here is a typical actual problem which regroups actual engrossment concerning diffraction analysis:

Someone crystallises a thin perovskite-like ferroelectric film in a pseudo-cubic phase (*i.e.* with a lot of peaks overlaps) in order to provide it optimised properties. The direct consequence is that the desired property is indeed increased, but only along specific crystalline directions, and it comes out that it is required to give the sample enough anisotropy.

Dilemma 1: This makes indispensable a quantitative texture analysis in order to interpret correctly the diffraction diagrams in terms of structure analysis (and this latter can deviate considerably from the bulk material). In turns, without an exact knowledge of the structure, the quantitative texture determination is for the less delicate to operate !

Dilemma 2: The desired anisotropy is often induced by deposition on single crystal substrates (*e.g.* by hetero-epitaxial relationship), which induces residual stresses in the films. The diffraction peaks are then shifted relative to their unstressed position, which bias on one hand the structural determinations, and on the other hand the QTA analysis since the peak positions are changing with the necessary rotations of the sample for texture measurements. It is then necessary to analyse the residual stresses in order to know structure and texture. However, differently oriented crystallites to not deform the same under the same stress, it exists an influence of the texture on residual stresses.

Dilemma 3: The samples are composed of several layers of different phases (including the substrate), which then have to be characterised in terms of structure/texture/stress too. Volume and absorption corrections become necessary, which are not operated the same on a covered layer, top film, substrate ..., and which bias structural and textural approaches. The corrections to be applied for structure and texture analyses depend on the layers thickness and absorption coefficients. For instance, a wrong determination of the layer thickness can be interpreted as intensity variations coming from atomic position variations and the associated peak shifts to residual stresses or/and different cell parameters. This false determination will modify pole density corrections and affect the texture solution. However, thickness determination is sometimes not easy. For instance ellipsometry may not be applied on films opaque to the considered radiation. For thin enough layers with smooth interfaces and surface, x-ray reflectivity may be used, if the electron densities are correctly determined. This latter depends however on the structure determination ...

Dilemma 4: In polyphased materials (all or partially crystalline), the quantitative phase analysis depends on the texture state of each phase. The quantitative texture analysis is then essential, but depends on the previous dilemma.

Dilemma 5: The interpretation of all these methodologies remains furthermore depending on the microstructural states, crystallite sizes and shapes (isotropic or anisotropic), crystalline defects (punctual, linear, planar or volumic), composition variations and microstrains, which in turns will be determined correctly if the other parameters are known satisfactorily.

Dilemma 6: Grinding samples can provide powders in which all these problems due to anisotropy are apparently bypassed. If one is allowed (or simply is able, for instance grinding thin films is not easy !) to crush the sample, it may however not resolve the problem, cause after grinding:

- the residual stresses are removed partially, or at least different;
- the microstructural state is different;
- all anisotropy like texture, layering, sizes ... is destroyed.

9.2: Implementation

In the preceding problem description, we see that the characterisation keystone lies in the existence, desired or not, of crystallite preferred orientations in the material. It needs then *in fine* to implement the determination of all the parameters accessible to diffraction/scattering of rays in a global methodology of characterisation, which has progressively taken the name of "**combined analysis**". This approach can be developed with a close collaboration of specialists in every domain and modern programming. The MAUD program actually includes the following formalisms:

WIMV, spherical harmonics, maximum entropy, components: QTA
Arbitrary correction of texture
Rietveld: structure analysis, QPA, QMA
Warren-Averbach (Fourier): microdistortions and crystallite sizes
Popa: anisotropic crystallite sizes, stress distribution function
Le Bail: diffraction peak extraction
Matrix: specular reflectivity, thicknesses, roughnesses
DWBA: electronic density profiles
$Sin^2\Psi$ and SDF: residual stresses
Layering: large thickness
Size and microstrain distributions
Warren: Stacking faults
Microabsorption
...

Of course, the previous formalisms could be run independently, fixing fitted parameters coming from one algorithm to refine another formalism, then fixing these latter to refine a second time the former and so on. This would result in a very long, manual, procedure.

It is better to use all these formalisms an an automatic way in one program. They can then interplay on each other using one or the other refinement approach (least-squares, genetic ...). For instance a first Rietveld refinement is operated in a cyclic manner on sets of diffraction diagrams measured at different sample orientations, then the extracted intensities are entered a QTA cycle, the result of which serving to correct diagrams for the next Rietveld cycle ... In between a reflectivity refinement of the thickness may be used to correct the other approaches. The operation leads to the determination of the parameters satisfying the best solution of the whole ensemble of measurements. Figure 19 shows the interdependency of the

parameters accessible to diffraction and scattering and the corresponding formalisms for refinement.

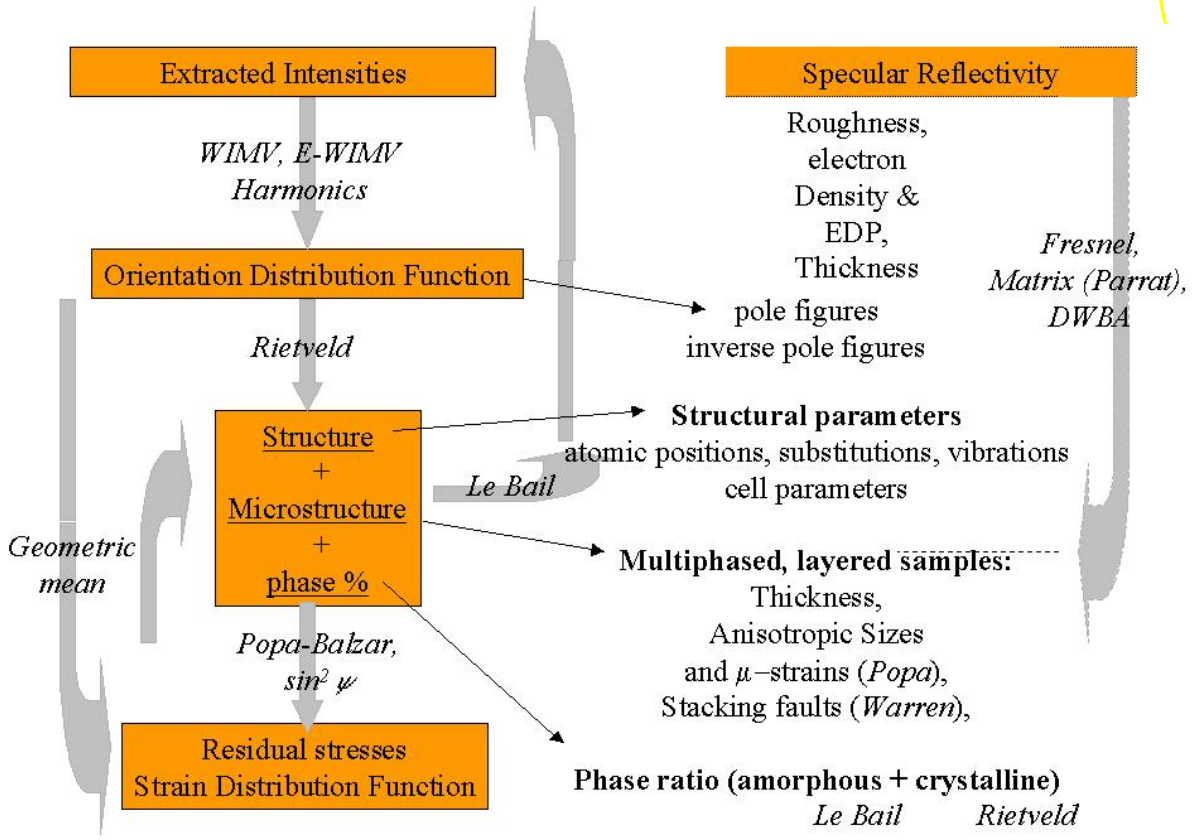

Figure 19: Combined algorithm, using least-squares, simulated annealing or genetic refinement procedures

The programs should give possibility to treat as well x-ray (classical, synchrotron, monochromatic or energy dispersive, symmetric or asymmetric geometries, 0D, 1D or 2D detectors) as neutron (thermal, TOF) data, which is the case of MAUD.

9.3. Used experimental set-up

This methodology requires however a lot of data, then their rapid acquisition using for instance multiple detectors. The first experiment allowing such an approach was developed using neutron data at l'ILL [Chateigner et al 1998] on the D20 beamline with a curved position sensitive detector. Using x-rays the first experiment of this kind [Cont et al. 2002] used a CPS and a 4-circles diffractometer. Since then the methodology has been used for different purposes [Lutterotti et al. 2002, Morales et al. 2002, Guilmeau et al. 2003, Lutterotti et al. 2004, Morales et al. 2004, Ricote et al. 2004].

The required diffractometer has to be equipped with four circles in order to correspond to a texture experiment, *i.e.* at least one tilt rotation χ, one azimuthal rotation φ, an incidence circle ω and a detection circle 2θ. One economises one circle (one scanning movement) by using a linear detector on the 2θ arm. Another circle and scan can be economised using a bidimensional detector. Use of a monochromatic beam is strongly recommended for thin films [Wenk 1992] but not only [Chateigner 1994].

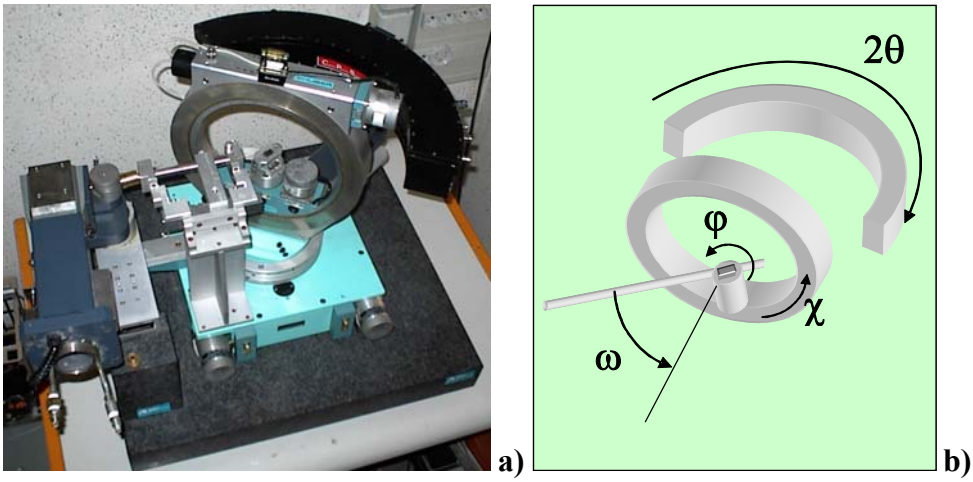

Figure 20: The x-ray diffractometer as set-up at CRISMAT **(a)** and its schematic showing the angle convention **(b)**

9.4. Instrument calibration

The spectrometer space is multidimensional, each rotation axis possibly giving rise to defocusing or misalignment effects. Each of these aberrations have to be calibrated for. Figure 21 is an illustration of such aberrations measured on a KCl standard powder, using the instrument of Figure 20.

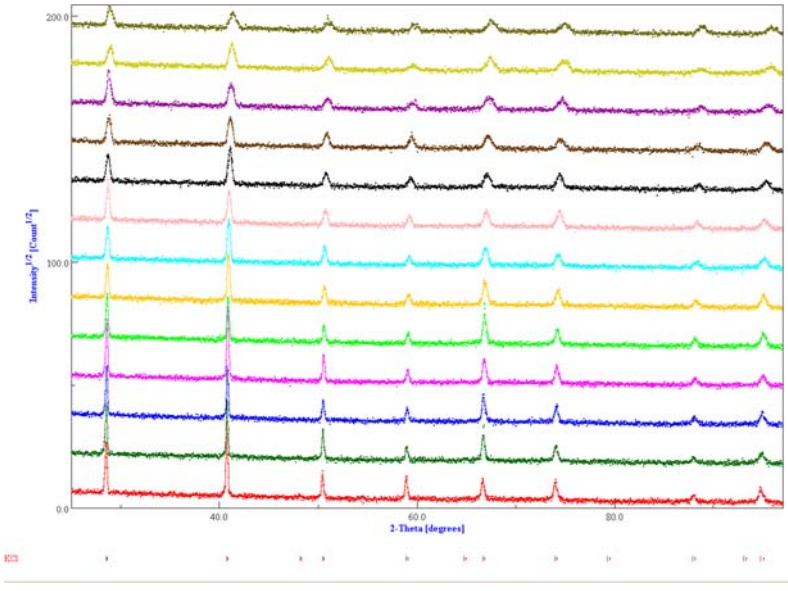

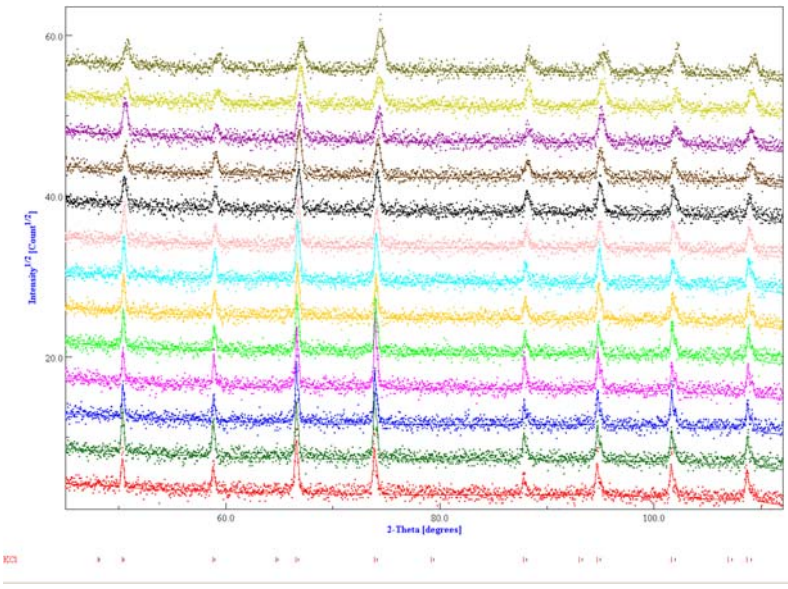

b)

Figure 21: Illustration of defocusing and misadjustment effects on peak shapes and diffractometer resolution function. Measurements on a KCl powder. Diagrams appear on top of each other from $\chi = 0°$ to $\chi = 60°$ by steps of 5° for **a)** $\omega = 20°$ and **b)** $\omega = 40°$.

Three major effects are visible, peak broadenings, peak shifts and background variations.

9.4.1. Peaks broadening

Broadening occurs when the incident beam is defocused at the sample surface due to its geometrical extent, producing variations in the irradiated area and apparent Bragg angle values. The defocusing effects are then depending on the variable angles Figure 22.

9.4.1.1 χ broadening

When χ increases, the peaks broaden by the so-called defocusing effect. If the total integrated intensity is not changed (for a bulk material and enough counting statistics), this broadening has to be calibrated for any quantitative microstructure determination. A polynomial approach is used to follow the broadening with χ:

- 231

$$\Delta_{\chi HWHM} = \Delta_{\chi} H = \sum_{u=0}^{U} p_{\chi u} \chi^{u}$$

with as many $p_{\chi u}$ parameters as necessary, including them progressively in the refinement up to U corresponding to a negligible $p_{\chi U}$ value. Here $\Delta_{\chi} H$ is the variation in HWHM due to the χ rotation.

9.4.1.2. 2θ broadening

For a given diagram measured at ω, peaks are broader at larger 2θ's. This effect is typical of flat specimen analyses (it does not occur for instance in transmission geometry using neutrons), and is illustrated in Figure 21a. It is corrected by the resolution curve using the Cagliotti polynomia.

9.4.1.3. ω broadening

For a given peak at 2θ, the FWHM is smaller at larger ω angles. This effect also is typical of flat specimen analyses (Figure 22b). It is corrected similarly to the χ-broadening by a polynomial approach:

- 232 $$\Delta_{\omega HWHM} = \Delta_{\omega} H = \sum_{u=0}^{U} p_{\omega u}\, \omega^{u}$$

9.4.1.4. General broadening

In order to adapt this type of corrections to diffractometers with more or other rotation axes, we can then use an equation which depends on the varying angle:

- 233 $$\Delta_{r} H = \sum_{u=0}^{U} p_{ru}\, r^{u}$$

with r the rotation of concerns and with as many p_{ru} parameters as necessary, including them progressively in the refinement up to negligible values.

9.4.2. Peak shifts

These effects come from misalignments of one or several of the rotation axes. For instance on Figure 21a one clearly observes a 2θ peak shift for large χ values, and this shift is not the same at two different ω. Depending on the experimental configuration, analytical formulae can be produced to fit these misalignments. Similarly to the previous corrections of Equations - 233, a polynomial approach can be used:

- 234 $$\Delta 2\theta_{r} = \sum_{u=0}^{U} p'_{ru}\, r^{u}$$

with p'_{ru} the factors to be determined, and $\Delta 2\theta_r$ the variation in 2θ peak position due to the misalignment of the rotation r (r = χ, φ, 2θ, ω ...).

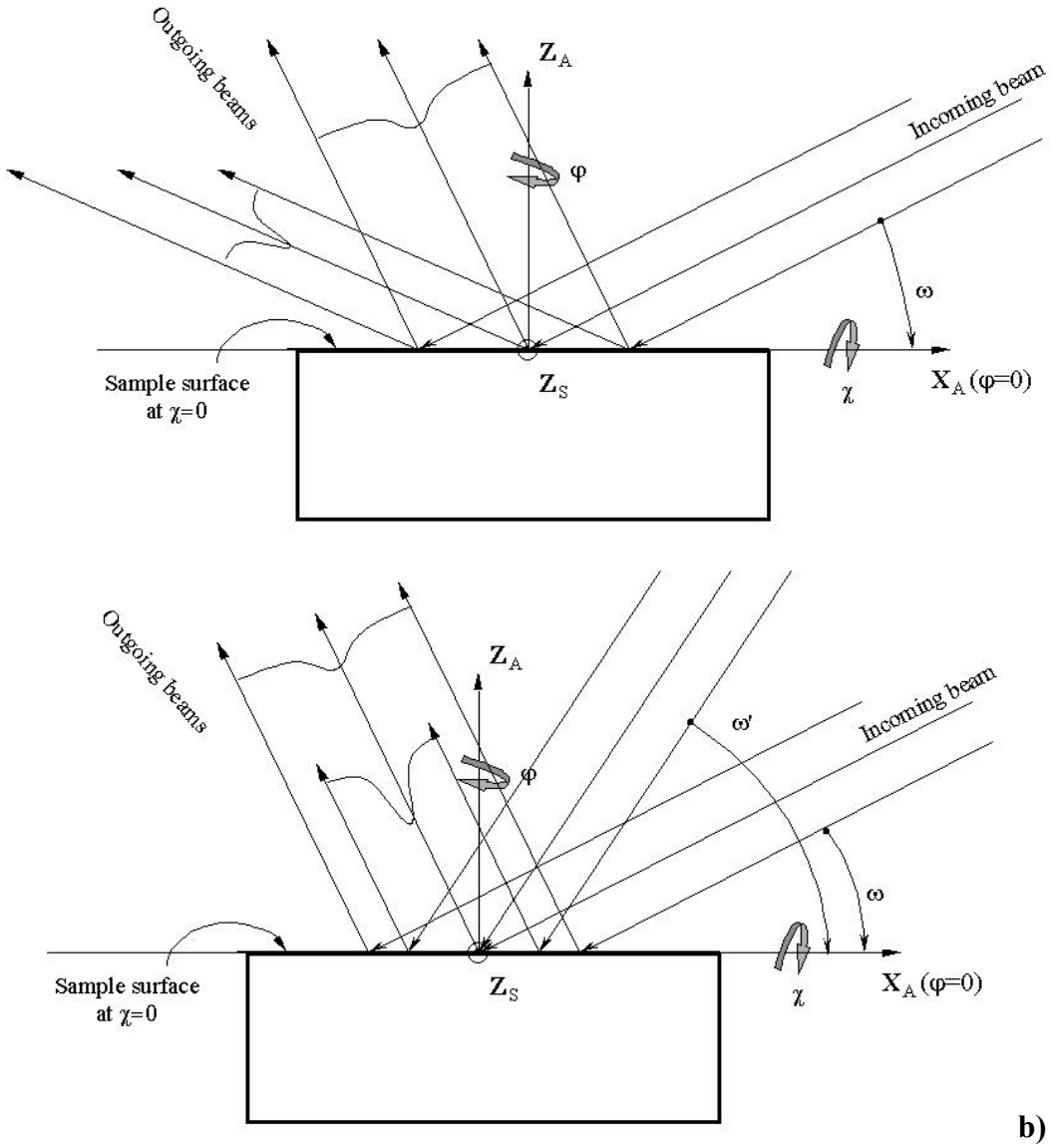

Figure 22: Origins of the **a)** 2θ and **b)** ω broadenings

9.4.3. Background variations

Furthermore, depending on many factors like sample shape, absorption ..., the background B can also vary with the various angles of rotations. These variations have to be corrected, which is usually operated through:

- 235

$$\Delta_r B = \sum_{u=0}^{U} p''_{ru}\, r^u$$

with p''_{ru} the factors to be determined.

9.5. Refinement Strategy

As for the Rietveld traditional refinement, one should not refine all the parameters at once, but chose to resolve the most influencing parameters first. The instrument has to be calibrated for its intrinsic aberrations beforehand (Caggliotti function, zero-shift, asymmetry ...), using the same instrumental parameters (slit sizes ...) and for the corresponding φ, χ, ω, 2θ ... angular ranges as in the previous paragraph.

Here is the procedure that one can use, which may depend on the problems to solve:

1 basic parameters of the Rietveld refinement: Scale factor + polynomial background + variations of the background through χ, ω, 2θ ... angular rotations
2 Same + basic phase parameters
3 Same + microstructure parameters
4 + crystal structure parameters
5 + texture
6 + phase fractions (preferably fitted on a sum diagram in which texture effects are reduced)
7 + strains

Of course there is no systematics since a lot of parameters are influencing one another. For instance reflectivity may be computed between steps 3 and 4 in order to better appreciate the sample thickness used in the rest.

Since a lot of parameters are refined simultaneously at the end of the procedure, the convergence radius of the methodology may be severely reduced. As a general trend the more independent experiments have been measured and the more convergence may be reached easily. However, when texture exists in the samples, the corresponding diffraction patterns exhibit simpler signal than powder patterns, which may be useful particularly for low-symmetry polyphased materials. In this case the combined approach gives access to better reliabilities of the refined parameters. Indeed, textured samples range between powders, in which angular relationships between atomic bonds cannot be probed directly using diffraction, and ideal single crystals for which these angular values are directly measured using four-circle goniometry. As such, texture analysis probes for angular relationships via the calculation of the ODF. The OD can then be seen as an object that self-consistently depends on the crystal structure, which provides a large number of constraints in the refinement, hereby removing parts of the correlation existing between refined parameters and ensuring, when enough independent measurements are available, a better convergence of refinement procedures.

9.6. Examples

9.6.1. Anisotropic crystallite shape, texture, cell parameters and thickness

One part of dilemma 5 considers the existence of anisotropic crystallite shapes, in a textured sample. When not using texture information, *e.g.* when it is impossible as in random powders or when the textured sample as been measured with too few orientations, the anisotropic shape of the crystallites can be, at least partially, masked. This will be illustrated in the following.

9.6.1.1 Diffraction pattern from single sample orientation

In a sample exhibiting a crystallographic texture, for one measured orientation of the sample (one pattern), only some $\{hk\ell\}$ planes are preferentially brought to diffraction, while the others are not detected. Consequently crystallite sizes may be severely biased since they are only estimated from these diffracting planes. Figure 23 illustrates these aspects for a sample exhibiting anisotropic crystallite shapes, ellipsoids elongated along the [111] direction of a cubic crystal system, *e.g.* silicon. In the case of crystallites randomly oriented in the sample (Figure 23a), the mean crystallite size as deduced from the 111 line is an average over the 111 multiplicity. Since for a single crystal of Si, the (111) plane is at 70.53° from $(1\,\bar{1}\,1)$, $(11\,\bar{1})$ and $(\bar{1}\,11)$, the mean size along <111> will take a value between the short and long axes of the ellipsoid. This reasoning remains valid for any $hk\ell$ diffraction line, resulting in a systematic lowering of the shape anisotropy when calculated from a single diagram. For the case of a textured sample having (111) planes mostly parallel to the sample surface and [111] elongated crystallites perpendicular to it (Figure 23b), the long dimension of the crystallites is more favoured than the short one, and this latter has to be probed with other $hk\ell$ lines. However, the long dimension is still underestimated if low ω values are used, because this configuration does not ensure to probe the maximum of the distribution of the crystallites orientation. Such biased estimations are often encountered in works reporting silicon crystallite size determination using the Scherrer formula, resulting in overestimated sizes with underestimate of shape anisotropy (Langford et Louer 1982, Feng et al. 2001, Vallat-Sauvain et al. 2000, Kroll et al. 1998). The integral width approach (Balzar et Popovic 1996) used by Houben et al. (2003) or even the direct Fourier deconvolution of the signal from the x-ray profile gives results closer to the reality but are still however lowering the shape anisotropy.

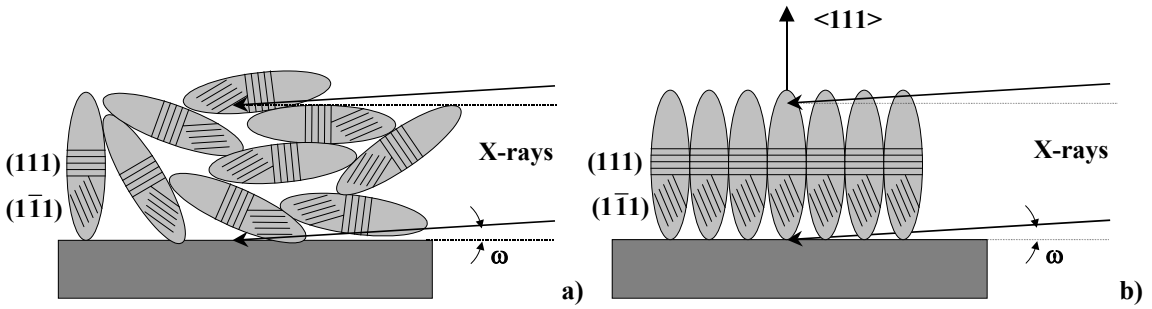

Figure 23: Schematics of a film composed of anisotropically shaped crystallites in a randomly oriented (**a**) and a textured (**b**) sample

9.6.1.2 Use of several sample orientations: combined approach

To overcome the above-mentioned problems, measurements of the full diffraction diagrams for multiple orientations of the sample are needed. This allows one to obtain a better estimate of the anisotropic shapes, weighted by the volumic ratio of material in a given orientation. This is achieved by the simultaneous analysis of the anisotropic shape using the Popa formalism and the quantitative texture using whichever texture model, here the WIMV approach. Figure 24 shows that very satisfactory fits are obtained using this approach on thin nanocrystalline Si films, with reliability factors R_B, R_w and R_{exp} around 5% (Table 2). Consequently the texture reliability factors RP_0 as reported in Table 2 are generally around 1% and never exceed 3%, attesting the good ODF refinement. Such reliabilities, if they could be achieved by simple texture parameter fits like used in the March-Dollase (Dollase 1986, March 1992) or Lotgering (1959) approaches, would not correspond to a physically understandable model of the texture in our case, because of the fairly complex ODF of our samples, as is seen on the inverse pole figure (Figure 25a).

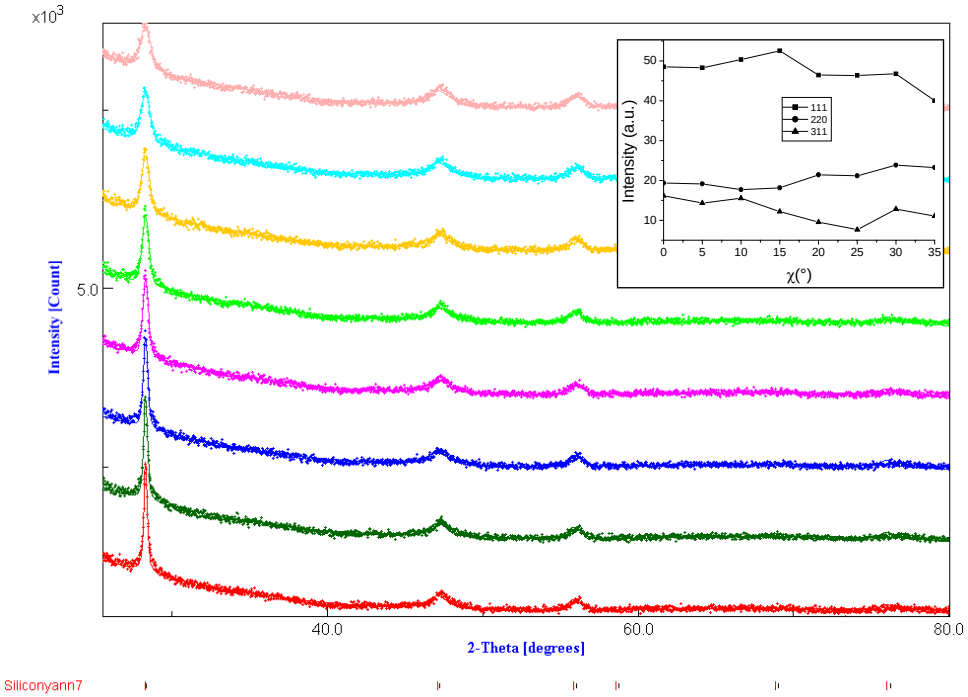

Figure 24: Selected fitted χ-scans that shows large peaks and the presence of texture in a Si thin film deposited on amorphous SiO_2 substrate by magnetron sputtering. The insert shows the net intensity variation of the main peaks, to better visualise the texture.

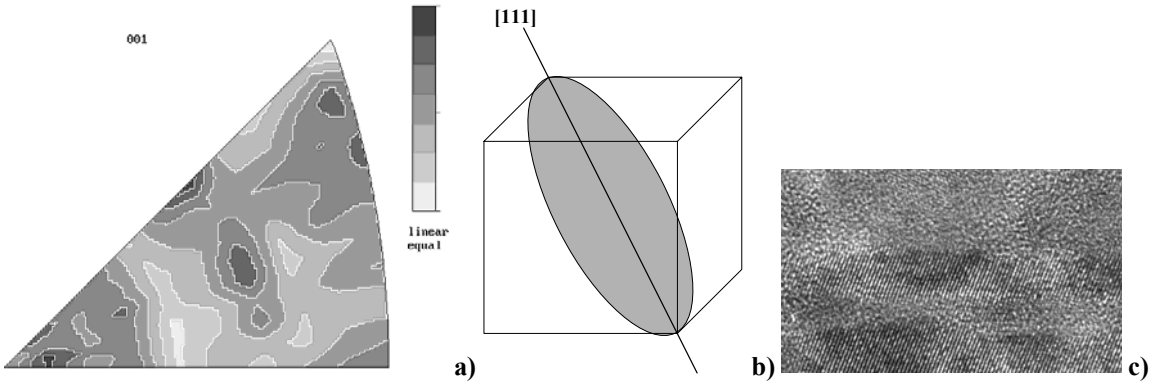

Figure 25: Inverse pole figure for the normal direction of the Si thin film of Figure 24 calculated from the refined ODF (linear density scale, equal area projection, max = 1.59 m.r.d., min = 0.45 m.r.d.) (**a**), schematics of the refined mean crystallite shape from Table 2 (**b**) and (**c**) high resolution TEM image of the Si crystallites.

Figure 25b illustrates the mean anisotropic shape as refined using the combined analysis. This picture coincides perfectly with high resolution TEM microscopy images (Figure 25c) in which elongated single crystals are evidenced. The refined cell parameters are obtained within a maximum of 0.0004 Å of standard deviation maximum, without neat variations with texture components [Magali et al. 2005].

a (Å)	**Anisotropic sizes** (Å)			**Texture parameters**			**Reliability factors** (%)			
				maximum	**minimum**	**F²**	**RP₀**	**R_w**	**R_B**	**R_exp**
	[111]	**[220]**	**[311]**	(m.r.d.)	(m.r.d.)	(m.r.d²)				

5.4466 (3)	94 (3)	20 (1)	27 (1)	1.95	0.4	1.12	1.72	4.0	3.7	3.5
5.4439 (2)	101 (3)	20 (1)	22 (1)	1.39	0.79	1.01	0.71	4.9	4.3	4.2
5.4346 (4)	99 (3)	40 (1)	52 (2)	1.72	0.66	1.05	0.78	4.3	4.0	3.9
5.4461 (2)	100 (3)	22 (1)	33 (1)	1.57	0.63	1.04	0.90	5.5	4.6	4.5
5.4462 (2)	98 (3)	20 (1)	25 (1)	1.22	0.82	1.01	0.56	5.0	3.9	4.0
5.4452 (3)	85 (2)	22 (1)	26 (1)	1.59	0.45	1.05	1.08	4.2	3.5	3.7
5.4387 (3)	89 (3)	22 (1)	28 (1)	1.84	0.71	1.01	1.57	5.2	4.7	4.2
5.4434 (2)	88 (3)	22 (1)	24 (1)	2.77	0.50	1.12	2.97	5.0	4.5	4.3

Table 2: Refined parameters for 8 analysed Si films deposited on various substrates [Morales et al. 2005]. Numbers in parentheses are one standard deviations as refined.

Furthermore, the procedure enables to refine the film thickness from the large angle part of the data, and since the films thickness are "seen" under various incidences due to the χ rotation of the texture scans. Such thicknesses are the ones as probed by x-rays, *i.e.* if strong porosity is present the x-ray thickness appears smaller. This is evidenced on Si nanocrystalline thin films deposited on SiO_2 substrates (Table 3), for which the porosity has been measured by x-ray reflectivity. While profilometry indicates the full geometrical thickness of the films, x-ray refinements show smaller thickness values due to porosity in the films.

Profilometry thickness (nm)	**x-ray thickness** (nm)	**Porosity** (%)
1350	711 (50)	26(3)
1470	1360 (80)	13(3)

Table 3: Thicknesses as measured by profilometry and refined by the combined analysis, compared to the porosity as determined by x-ray reflectivity [Morales et al. 2005] on two Si nanocrystalline thin films deposited on amorphous SiO_2 substrates.

9.6.2. Layering, isotropic shape, microstrains, texture, structure

Dilemma 3 points out that for layered systems the different layers thickness are necessary to correct the data for absorption ... However, for thin heterostructures it is not always possible to measure all the thicknesses, and on the contrary, the effective thicknesses for x-rays are necessary which, depending on the samples, are not all times the theoretical ones or the ones as determined by profilometry. In such cases the combined approach allows for their refinement [Ricote et al. 2003]. We will illustrate this on an as-synthesised spin-coated sol-gel ferroelectric thin structure consisting of a calcium-modified lead titanate film $Pb_{0.76}Ca_{0.24}TiO_3$ (PCT) deposited on a $Pt/SiO_2/Si$-(100) substrate.

In such systems, the texture of the PCT film is desired with <001> directions (directions of the polar axis) perpendicular to the film plane. The Pt electrode is also textured, and can possibly be correlated to the PCT texture. The layers thickness are of importance, so as crystallite sizes and microstrains for both phases. Of course the structure of the PCT film has to be investigated. As we can see (Figure 26) strong overlaps occur in such systems between Pt and PCT peaks. In fact, none of the Pt lines is single, precluding any "conventional" texture analysis using non combined procedures. As a consequence of the spin

coating elaboration process, the texture exhibits a fibre-like character, with single or several fibre components (Figure 27).

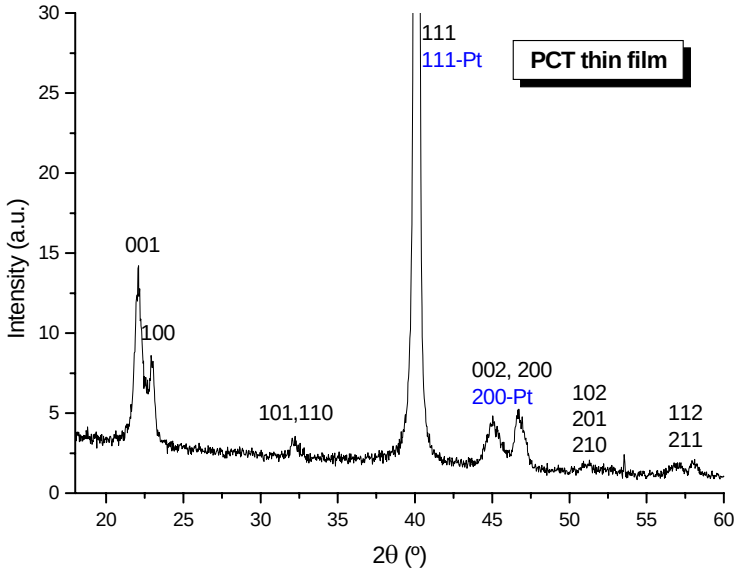

Figure 26: Bragg-Brentano diagram of a PCT/Pt/SiO2/(100)-Si thin structure. Notice the strong overlap between Pt and PCT peaks

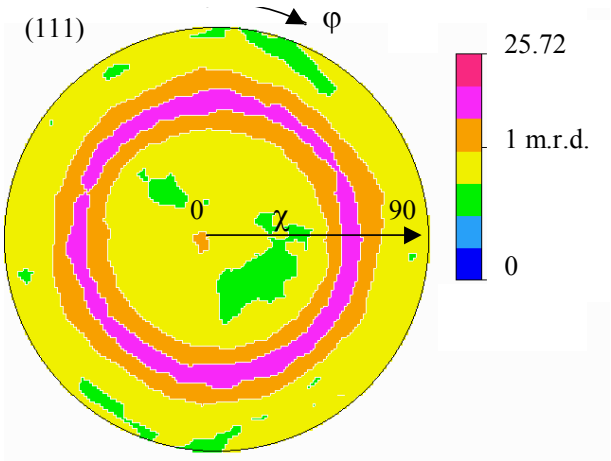

Figure 27: {111}-PCT pole figure recalculated from the OD of a PCT/Pt/SiO2/(100)-Si thin structure which shows the fibre-type character of the texture. Equal area projection, logarithmic density scale

As one can see (Figure 28) the refinement of such a sample gives rise to satisfactory reliability factors with R_{wp} and R_B of 5% and 6% for the texture refinement using the E-WIMV model, and R_{wp} and R_B factors of 13% and 12% for the Rietveld refinement, respectively. In this case, the E-WIMV model results in a better refinement because mainly of the strong texture of Pt [Morales et al. 2002]. The texture of the Pt electrode is very strong and characterised by <111> directions perpendicular to the film plane (Figure 29 left) as the only component. For the PCT film the texture is multicomponent with major components being with <100> and <111> directions perpendicular to the film surface (Figure 29, right). This orientation is detrimental for practical applications of the polarisation direction, since <001> is mainly located in the film plane. The 15% of random c-axes provides however

some, thought moderate, polarisation properties. While the Pt layer appears perfectly crystallised with crystallite sizes extending along the whole layer's thickness and small microstrain values, the PCT layer exhibits approximately twice as microstrains and consequently smaller crystallite sizes around 390 Å (Table 4). All parameters are refined with satisfactory standard deviations, including the z position of titanium and oxygen atoms.

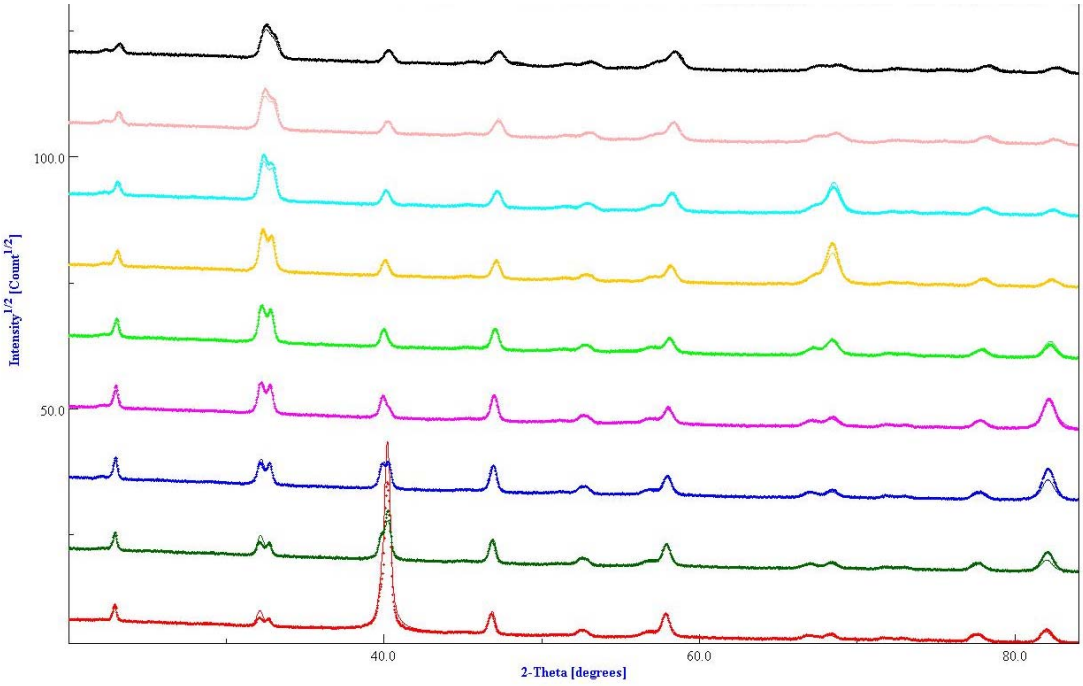

Figure 28: 2θ diagram χ-scans of one film, showing the good agreement between experimental (points) and refined (lines) spectra. Bottom diagram is measured at χ = 0°, top diagram at χ = 40°, by steps of 5° up.

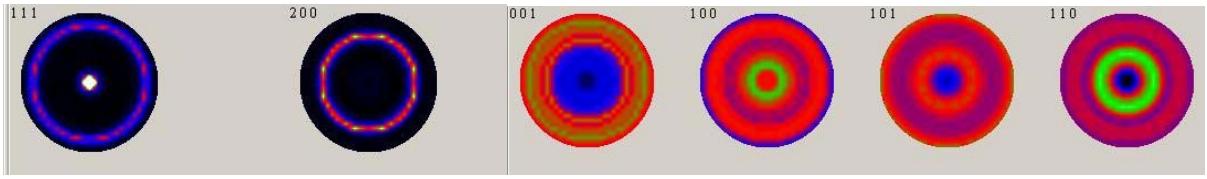

Figure 29: {111} and {200} recalculated pole figures for the Pt electrode layer (left, max. density is 10 m.r.d., min density is 0 m.r.d.) and {001}, {100}, {101}, {110} and {111} for the PCT film (right, max. density is 2.1 m.r.d., min density is 0.15 m.r.d.). Linear density scales, equal area projections.

Layer	Cell parameters (Å)	Thickness (Å)	Crystallite size (Å)	μ-strain (rms)
Pt	3.9108(1)	457(3)	458(3)	0.0032(1)
PCT	a = 3.9156(1) c = 4.0497(6)	2525(13)	390(7)	0.0067(1)

PCT structure	Occupancy	x	Y	z
Pb	0.76	0	0	0
Ca	0.24	0	0	0
Ti	1	0.5	0.5	0.477(2)
O1	1	0.5	0.5	0.060(2)
O2	1	0	0.5	0.631(1)

Table 4: Layer and structural characteristics of the sample of Figure 28.

9.6.3. Phase and texture

9.6.3.1. Texture removal

Preferred orientation is a sample characteristic that can be desired or not. In both cases if the sample can be destroyed, mechanical grinding of the sample can provide an untextured sample. If destruction is prohibited, or if specific characteristics linked to texture would be removed by the grinding process, one can decide either to rotate the sample during measurements in order to suppress textural effects, or to physically interpret this texture and to take it into account using a combined refinement.

However, texture removal using sample rotations is always a risky procedure without knowing the texture itself: it may happen that the rotation axis corresponds to a specific texture axis, *e.g.* the fibre axis of an axially symmetric texture. This will be illustrated for several samples in the following.

9.6.3.2. Crystalline multiphase textured compounds

9.6.3.2.1. Top-seeded MTG grown $YBa_2Cu_3O_{7-\delta}$ / Y_2BaCuO_5 ensembles

In such systems the superconducting $YBa_2Cu_3O_{7-\delta}$ phase (Y123) exhibits critical current densities (Jc) favoured in the (**a**,**b**) plane of the orthorhombic (Pmmm space group) structure, with approximately ten times more conductivities along (**a**,**b**) than along **c**. A strong texture is then necessary in order to benefit of optimised properties, particularly since texture development also strongly reduces weal links for the transport currents [Dimos et al. 1988]. The insulating Y_2BaCuO_5 (Y211) phase (Pnma space group) either precipitates at the peritectic formation of Y123 or/and is added in the process as fine particles. This latter phase acts as flux pinning centres for the enhancement of critical current densities. Many techniques have been developed for the elaboration of textured bulks of this system. The Melt Textured Growth (MTG) technique [Jin et al. 1989] first appeared as very promising in obtaining large Jc values. Alignment under a high magnetic field **H** also promotes **c**-axes alignment with **c** // **H**, due to paramagnetic susceptibility anisotropy of the crystals [de Rango et al. 1991]. A lot of different techniques successfully achieved orientation development by combining MTG processes with thermal gradients, magnetic fields, quenching ... However, growing large single domains of the Y123 phase at a several 10 cm^3 scale could only be operated using the so-called Top-Seeding Melt Textured Growth (TSMTG) technique, consisting in promoting texture using heteroepitaxial like relationship between the growing Y123 and a $YBa_2Cu_3O_{7-\delta}$ (Sm123) crystal seed [Cardwell 1998]. In this elaboration process the Y211 phase is not (or very slightly) textured.

Nevertheless, for such large samples, the oxygenation of the as-synthesised insulating $YBa_2Cu_3O_6$ phase to the superconducting Y123 meets with two difficulties. On one hand macroscopic crack formation occurs, that strongly diminishes the mechanical behaviour of the sample. On the other hand, the oxygenation process, lying on solid state diffusion through the bulk core, becomes problematic and gives rise to unreasonable treatment times. Some authors [Noudem et al. 2003, Guilmeau et al. 2003] proposed to bypass this problem using infiltration techniques on polyurthane foams or artificially patterned holes prior to oxygenation (Figure 30), respectively. Such samples are very hard to study using x-rays because of their irregular geometry, but neutrons are not too much sensitive to such irregularities for the phases into consideration. Figure 31a shows the 1368 neutron 2θ-diagrams measured in as many foam-sample orientations using the D1B line of ILL, in order to carry out combined analysis, while

Figure 31b illustrates the sum of all these diagrams with the associated fit using an arbitrary texture model. As an evidence, although the structures of the two phases are known, the texture correction is not enough to reproduce correctly the experiments. The two rotations χ and φ involved in the 1368 measurements were not enough alone to eliminate texture effects. In this case, this comes from the presence of a very strong texture in Y123 (visible as strong Y123 peak in Figure 31a) while no texture is present for the Y211 phase, leading to a comparatively insufficient probe of the Y123 phase. However this summation approach allows the refinement of the cell parameters and crystallite sizes for the two phases (Table 5), and a rough estimate of the phase volume fractions. The cell parameters are in good agreement with the abundant literature. A calcite sample with large crystallites and without deformation was used as a standard to estimate isotropic crystallite sizes. The instrumental resolution provides with estimates of these sizes, with relatively large standard deviations in this size range.

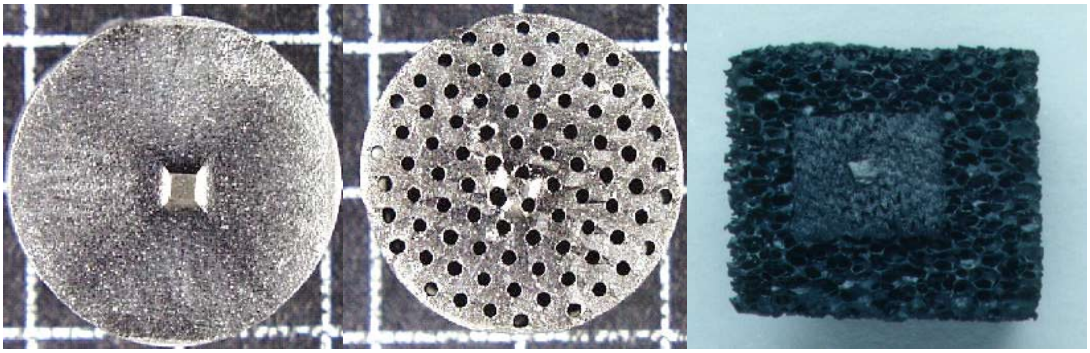

Figure 30: Top surface of a Y123 single domain, before perforation with the Sm123 seed in the middle (left) and after perforation (middle). Squares are 1 cm. A seeded Y123 / Y211 ensemble grown on a polyurethane foam.

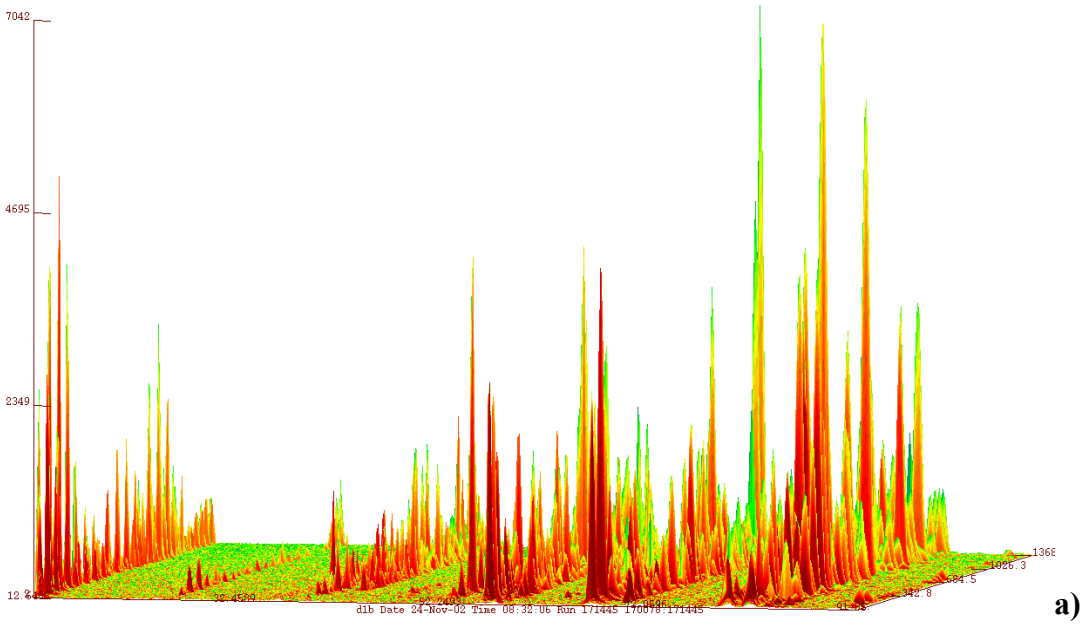

a)

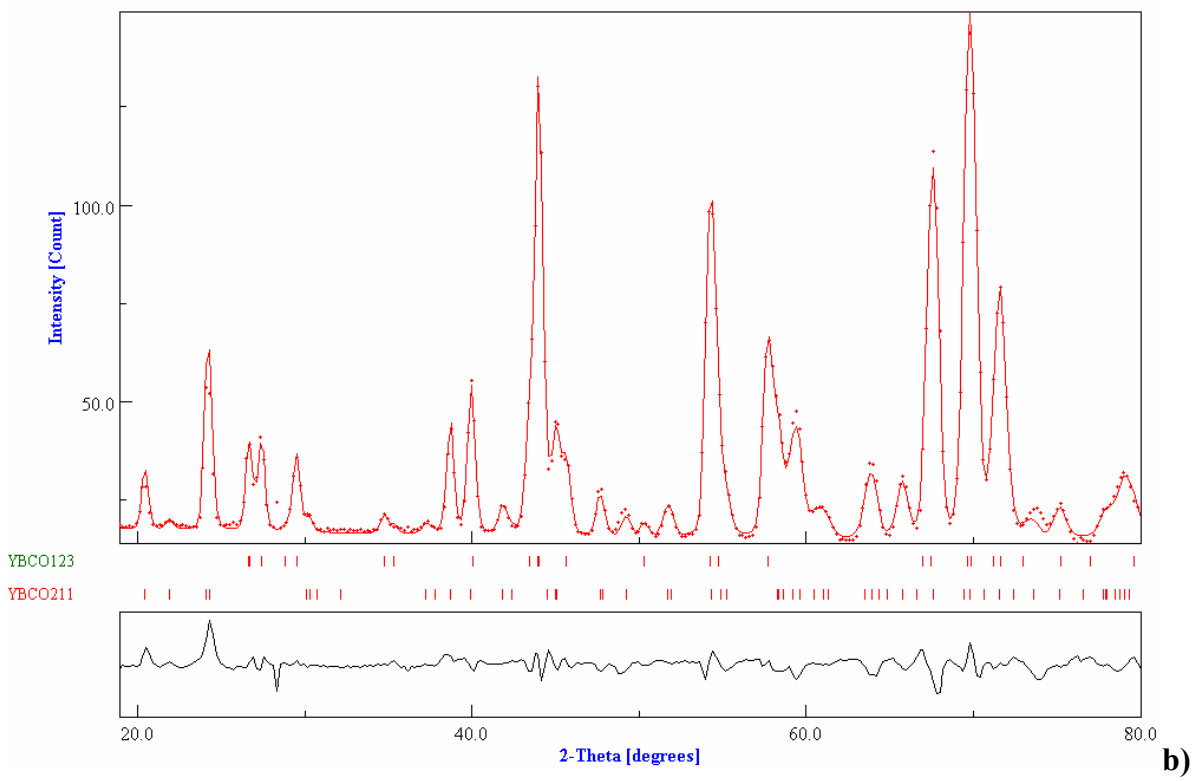

Figure 31: The 1368 neutron 2θ-diagrams measured on the foam sample of Figure 30 **a)** and Rietveld refinement of their sum **b)**, allowing phase, particle size and cell parameters quantitative determinations. Reliability factors: R_w = 5.43 %, R_B = 19.71 %, used wavelength: 2.53 Å.

The texture analysis using the E-WIMV model provides the full QTA of the Y123 phase (Figure 32). While the foam exhibits several single domains, due to the initial complex spacial structure of the polyurethane foam, the perforated sample only shows one single domain that extends throughout the sample volume, and correspondingly approximately 15 times larger maximum orientation densities (if one excepts small poles around 5 m.r.d. compared to the 128 m.r.d. at maximum).

	a (Å)	b (Å)	c (Å)	V (Å^3)	Crystallite size (nm)
Y123	3.8128(6)	3.8803(9)	11.662(4)	46(1)	136(32)
Y211	12.158(4)	5.645(2)	7.117(3)	54(2)	139(43)

Table 5: Cell parameters and volume fractions of the Y211 and Y123 phases of the foam sample as refined for the summed diagram of Figure 31. Parentheses are one standard deviation.

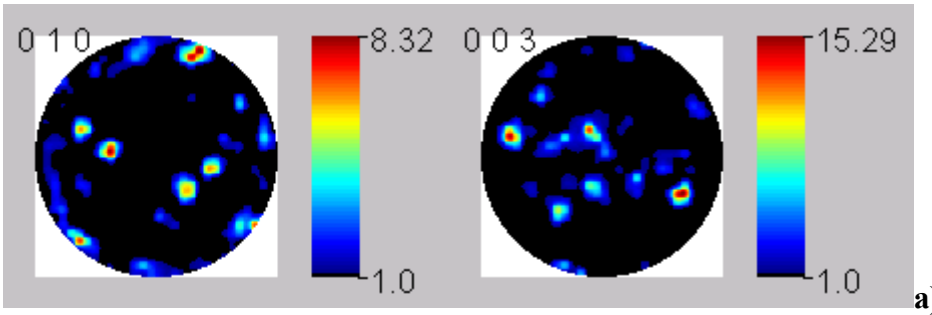

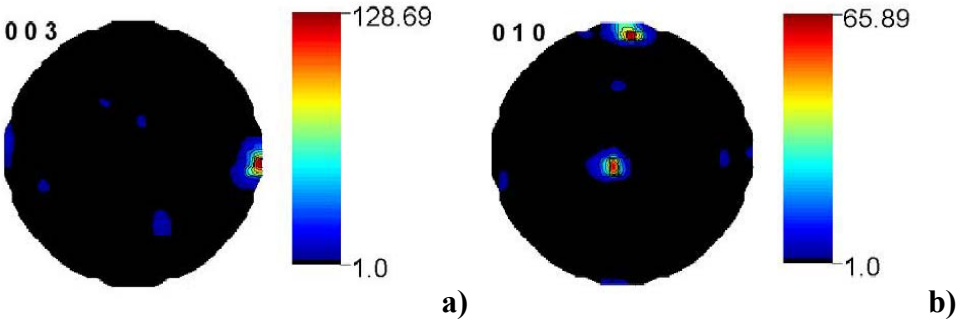

Figure 32: {003}-Y123 and {010}-Y123 recalculated pole figures of the perforated sample **a)** and of the foam **b)** samples of Figure 30. Linear density scales, equal area projections.

The superconducting properties of the perforated samples are in general not affected by the drilling process. This is for instance the case of Jc versus H curves and normalised trapped field maps (Figure 33). Similar values of the trapped field are observed, and even slightly larger Jc's are obtained for the drilled samples with a tendancy to accept larger applied magnetic fields, due to better oxygenation in the bulk of the material [Noudem et al. 2004, Noudem et al. 2004a].

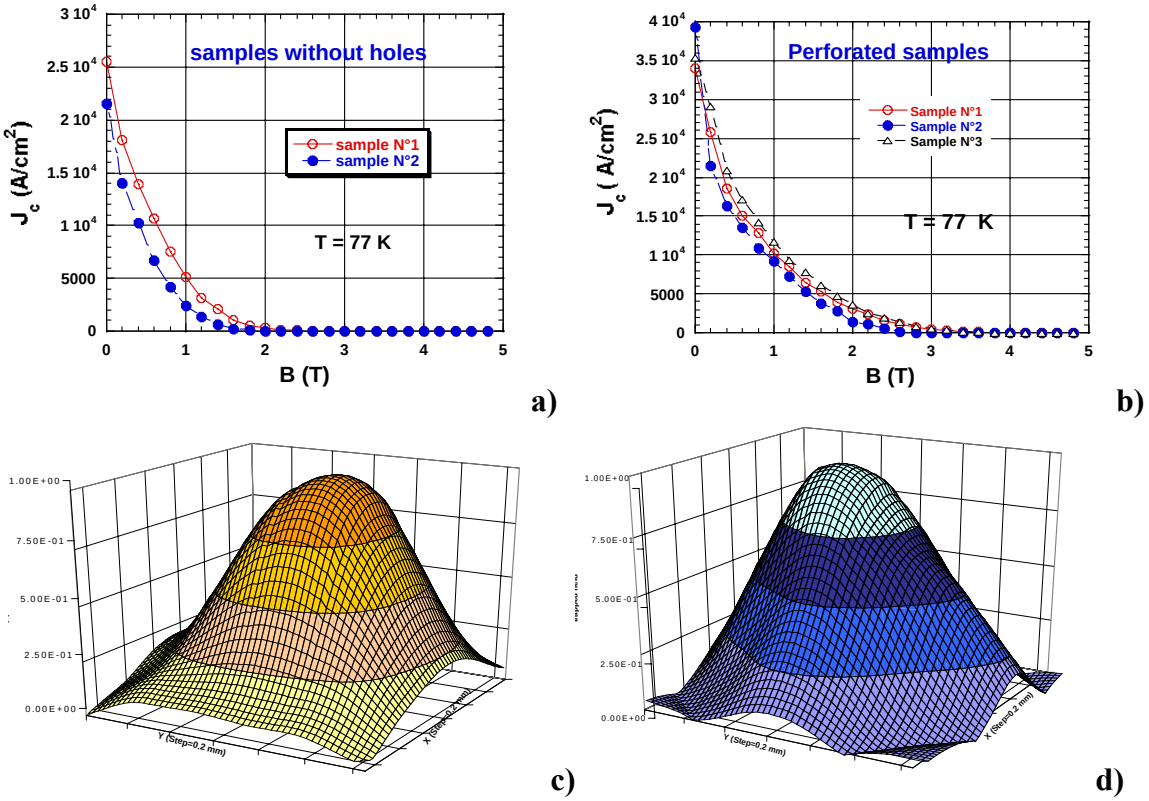

Figure 33: Jc(B) curves at 77 K for the plain **a)** and drilled **b)** samples, and corresponding normalised trapped magnetic field maps field cooled in 0.4 T at 77 K **c)** and **d)** respectively.

9.6.3.2.2. Sinter-Forged Bi2223 / Bi2212 samples

Sinter-forging methods are effective for obtaining bulk ceramics of $(Bi,Pb)_2Sr_2Ca_2Cu_3O_{10+x}$ (Bi2223) superconductor with a grain oriented texture. As in the previous example on Y123, the crystal structure of Bi2223 (and its related Bi2212) is strongly anisotropic and gives rise to strongly larger critical current densities along the (**a**,**b**) planes of the structure. High texture strengths and critical current densities around 10000 A/cm^2 at 77K in self magnetic field have been obtained [Tampieri et al. 1997]. However, in various papers published on this subject, similar optimised transport properties for Bi2223 are reported. The composition of the starting powder is probably the main cause of such saturation, as sinter-forging techniques generally used starting pellets composed of highly pure Bi2223 powder. Thus, the typical sinter-forging process requires precise control of the experimental conditions to allow weak partial fusion of the Bi2223 phase, which produces enough liquid phase to allow sufficient grain rotation and sliding. This weak decomposition is difficult to control and generally leads to a decrease of the Bi2223 phase content.
An alternative route for the synthesis of highly textured Bi2223 discs was recently reported [Guilmeau et al. 2002]. Instead of starting with a pure Bi2223 powder, the alternative proposes the use of calcined powders composed of $(Bi,Pb)_2Sr_2Ca_1Cu_2O_{8+x}$ (Bi2212) and secondary phases such as Ca_2PbO_4, $CaCuO_3$ or CuO [Shi et al. 1989, Uzumaki et al. 1989, Chen et al. 1991, Wang et al. 1993], in solid or liquid states, as starting components. As a result, the plate-like grains grow and reorient more easily because of the large amount of liquid in the powder (Figure 34a). However, the characteristics of the best samples are still not optimised. The Bi2223 phase content is relatively low and must be increased in order to improve the critical current density, which may be accomplished by using different starting powder compositions and grain size distributions in order to increase powder reactivity, i.e. the Bi2223 phase formation kinetic.

We show here how the combined approach helps investigating the influence of starting precursor powders on the transport properties and texture quality of samples prepared by the sinter-forging method.

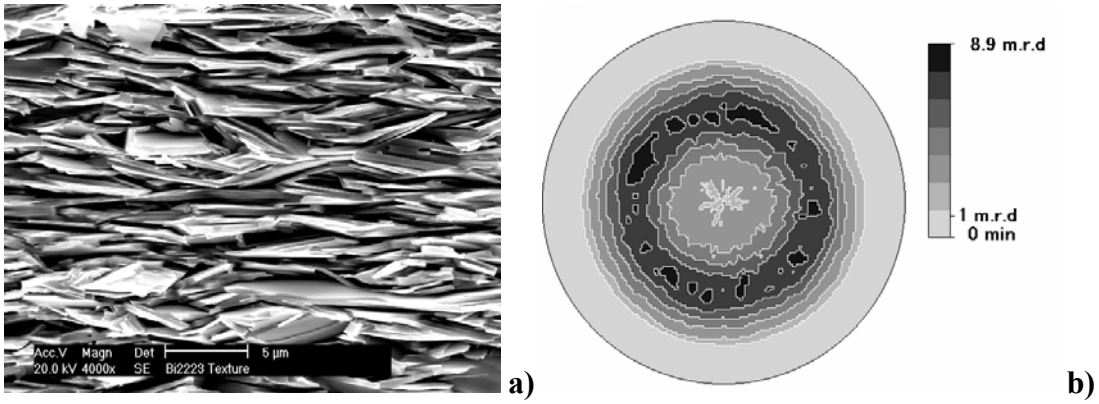

a) **b)**

Figure 34: SEM image of a Bi2223 aligned platelet microstructure resulting from the sinter-forging process under uniaxial pressure. Pressure and mean c-axis directions are vertical **(a)**. Corresponding {119} pole figure showing the axially symmetric texture. Pressure and mean c-axis directions are perpendicular to the pole figure plane, logarithmic density scale, equal area projection **(b)**.

As expected for uniaxially deformed materials without subsequent growth, a C_∞ axis of symmetry aligned with the pressure axis on the samples is observed (Figure 34b). Then only tilt χ-scans were performed. The combined analysis, calibrated on the LaB_6 standard, was operated in order to check for volume fractions of Bi2223 and Bi2212 phases, isotropic crystallite sizes, cell parameters and textures of the two phases.

Neutron investigations clearly show the strong texture achievement in the sinter-forged samples (Figure 35a). They also evidence the presence of the $(Sr,Ca)_{14}Cu_{24}O_{41}$ (14:24) residual phase. On these diagrams, the strong overlaps between the peaks of the two main phases is neatly visible. The fit of the diagrams (Figure 35b) gives reasonable results, with low reliability factors (Table 6) for the Rietveld as well as for the texture fit.

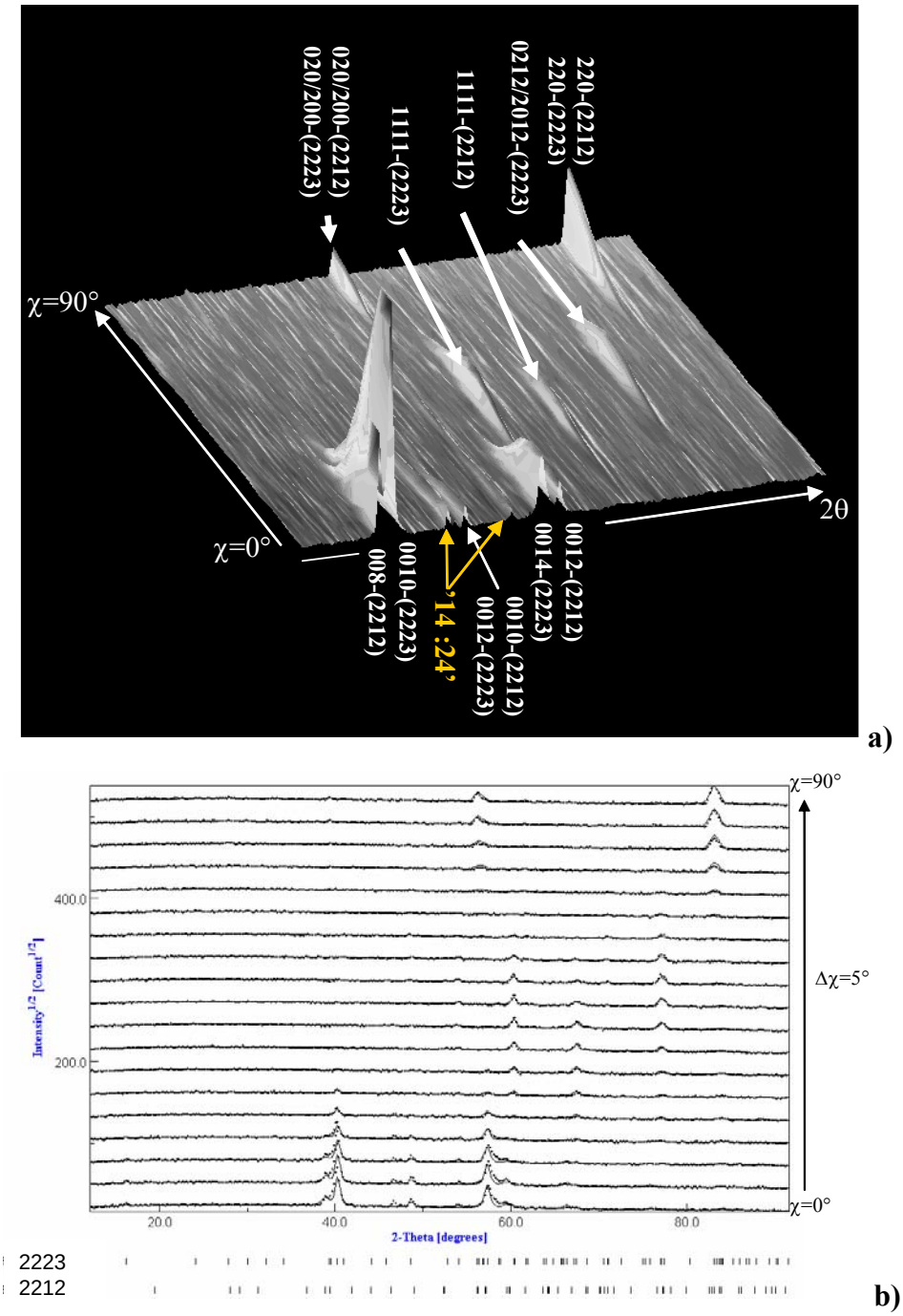

Figure 35: Neutron χ-scans from the D1B-ILL beamline. Note the strong decrease of 00ℓ line in the lower χ range, and the strong increase of hk0 lines in the higher χ range **(a)**. c-scans fit using the combined approach **(b)**.

The full representation of the OD is, in the case of fibre textures, represented by the inverse pole figures (Figure 36) calculated for the fibre direction. We can see a major component with {001} planes perpendicular to the fibre axis, with a small component for

(10ℓ) and (hk0) planes, probably related to the overlapping problems for low χ positions (Figure 35b). Nevertheless, these graphs confirm the development of the (00ℓ) texture and highlights the increase of the texture strength for larger sinter-forging dwell-time.

Transport critical current densities (Table 6, Figure 37) exhibit a clear correlation with the refined parameters and the sinter-forging dwell-time. The improvement of bulk performances, *i.e.* Jc, is closely related to an increase of the OD maximum, the Bi2223 phase fraction and the mean crystallite size. The circulation of the current is not only eased by a better alignment of grains and a larger fraction of Bi2223 but also by a larger crystallite size which limits consequently the number of grain boundaries, *i.e.* current barriers in the material. We can also note that, for 20h and 50h dwell times, the textures of Bi2212 and Bi2223 are intimately linked indicating the strong growing interaction between these phases (Figure 37). It should be noted here, that a nucleation-growth mechanism between Bi2212 and Bi2223 phases, even for long dwell time, has been established in previous works [Guilmeau et al. 2003].

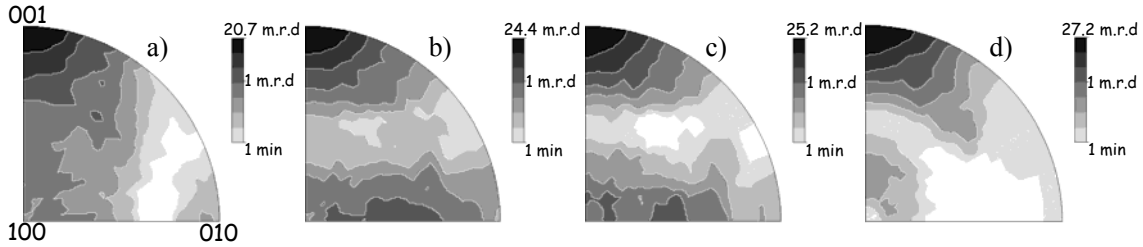

Figure 36: Inverse pole figures of the Bi2223 phase calculated for the direction of the applied pressure (fibre axis of the texture). Samples textured during **(a)** 20h, **(b)** 50h, **(c)** 100h and **(d)** 150h. Logarithmic density scale, equal area projection.

Sinter-forging dwell time (h)	**Orientation Distribution Max** (m.r.d.) *Bi2212*	*Bi2223*	**Bi2223** (%)	**Crystallite size Bi2223** [nm]	$\mathbf{R_B}$ (%)	**Rw** (%)	$\mathbf{RP_0}$ (%)	$\mathbf{RP_1}$ (%)	**Jc** (A/cm^2)
20	21.8	20.7	59.9(1.3)	205(7)	7.56	11.1	17.74	10.56	12500
50	24.1	24.4	72.9(2.9)	273(10)	7.54	11.37	17.05	11.04	15000
100	31.5	25.2	84.4(4.6)	303(10)	5.4	8.04	13.54	9.31	19000
150	65.4	27.2	87.0(4.1)	383(13)	6.13	9.12	16.24	12.25	20000

Table 6*:* Refined parameters extracted from Rietveld/WIMV combined analysis and reliability factors obtained from different sinter-forging time samples. Transport critical current densities, measured on each sample, are also reported.

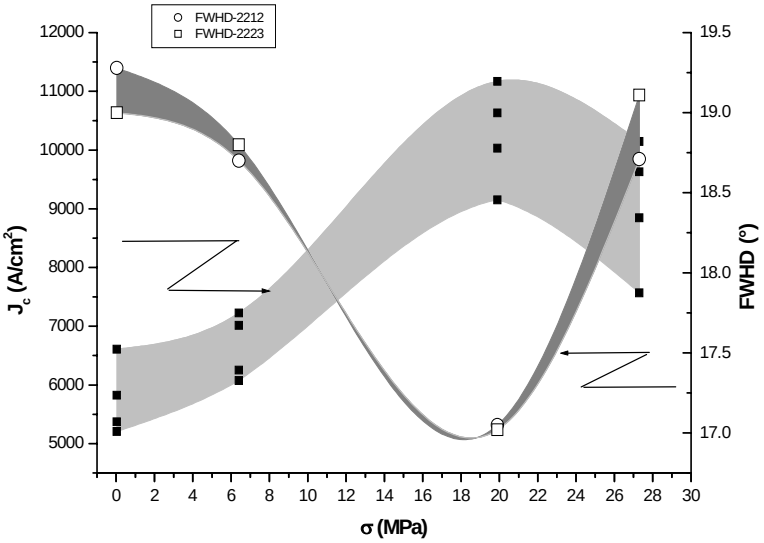

Figure 37: Correlation between FWHD, applied unidirectional stress σ and transport Jc in Bi2223 sinter forged samples. Points for the same σ correspond to identical measurements on various points of the same sample

9.6.3.3. Amorphous-Crystalline multiphase textured compounds

Nuclear waste storage over geological periods is one of the main problems that have to be addressed by the nuclear industry. The synthesis of new specific storage matrices and the study of their sensitivity to irradiation (γ-rays, α particles, fission fragments) is of prior importance. Among the potential matrices, the apatites are considered since their structure allow the incorporation of many elements such as I, Cs and/or trivalent actinides [Erning et al. 1995, Beauvy et al. 1998, Weber et al. 1998, Wang et al. 2000, Konings et al. 2002]. Apatite is the generic name of a family of calcium phosphates with formula $Me_{10}(XO_4)_6Y_2$ which crystallise in the hexagonal $P6_3/m$ space group, with Me (Ca^{++}, Ba^{++}, Pb^{++}) suitable for substitution by (Na^{+}, Rb^{+}, Cs^{+}) or (Al^{3+}, Nd^{3+}, La^{3+}) cations, while the XO_4 group (PO_4^{3-}, VO_4^{3-}) suitable for substitution by SiO_4^{4-}, GeO_4^{4-} or SO_4^{2-}, CO_3^{2-}, HPO_4^{2-} groups. The charge is balanced by monovalent anions, Y, such as F^-, Cl^-, OH^-. The apatite structure is built up of a frame of XO_4^{3-} groups giving rise to two types of tunnels. The first tunnel type is made of Me(I) atoms with 4 Me cations in the 4f sites of the structure surrounded by 9 oxygen atoms, whereas the second tunnel type is formed of 6 Me(II) cations in the 6h sites surrounded by 6 oxygen atoms and 1 Y atom.

The flexibility of the apatite structure versus substitution explains why the silicate substituted apatites also known as britholites, can be used to store iodine, cesium and minor trivalent actinides. Apatites also exhibit a high chemical stability in slightly alkaline water medium and are stable against radioactive excitations: some natural apatites found in In-Ouzzal (Algeria) were found crystallised (non metamict) despite their irradiation to a fluence two to three times higher than the amorphisation dose. The most common apatites are the fluor- and hydroxy-apatites of respective formula $Ca_{10}(PO_4)_6F_2$ (FAp) and $Ca_{10}(PO_4)_6(OH)_2$ (HAp). Furthermore, the most interesting property of FAp is its relatively low recrystallisation temperature, which induces a quasi-total damage recovering under thermal activation associated to the irradiation itself.

Nuclear wastes are mainly composed of actinides produced by nuclear transmutation inside reactors (Np, Pu, Am, Cu) and by fission products (Sr, I, Gd, Cs) resulting from the ^{235}U fission. After their production, most of these radionuclides transform spontaneously following

a complex scheme of spontaneous desintegrations characterized by the emission of α particles. In this way, the damage is mainly due to cascades of nuclear collisions created by emitting nuclei recoil [Ouchani et al. 1997, Soulet et al. 1997, Weber et al. 1997]. Spontaneous fission, which occurs only for a few elements (Np, U, Pu), is less probable but results in the production of highly energetic ions (up to 100 MeV). Thus, during long time storage of nuclear wastes, the matrices can be damaged either by α particles and heavy atoms in the nuclear collision regime or by energetic lighter atoms produced by the fission process in the electronic energy loss regime.

Damage induced by fission fragments can be simulated on fluorapatites ceramics irradiated by heavy ion irradiations (Kr, I). Samples irradiated with 70 MeV ^{87}Kr ions (T = 10°C) delivered by the IRRSUD beamline of the GANIL facility (Caen, France) and with 120 MeV Iodine (T = 298°C) using the Vivitron facility (Strasbourg, France), at fluences ranging from 10^{11} to 5.10^{13} ions cm^{-2} have been analysed.

Irradiation-induced damages are located up to a depth of approximately 10 µm from the incoming surface, and x-rays can be used to probe the amorphised volume fraction of material. The use of a 1D or 2D detector is then mandatory to avoid tremendous acquisition times, and an incidence angle ω = 5° is necessary to probe only the near-surface of the sintered pellets. Under this condition, 97% of the diffracted signal comes from the first 9 µm of the sample, which corresponds to the estimated perturbed thickness. However, because of recrystallisation, planar textures are observed in these pellets. In order to minimise texture effects on the diffraction patterns, the samples were rotated around their normal during acquisition, but the texture could not be fully removed. In order to quantitatively determine the amorphized volumic fraction of the perturbed layer, an arbitrary texture model was introduced for the crystallised fraction. The amorphous phase was modelled using an expended fluorapatite structure with very small crystal sizes, typically of 40Å or smaller. Counting times around 24 h were necessary to detect amorphous fractions below 5% in volume.

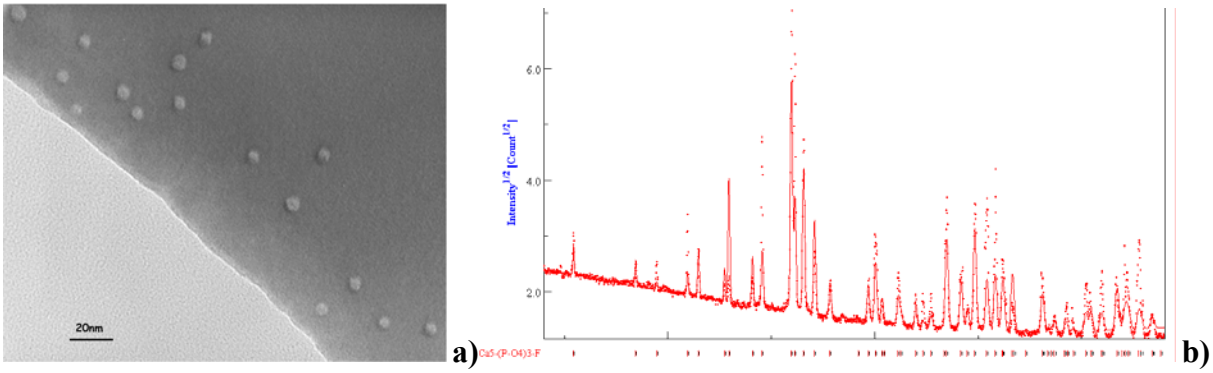

a) **b)**

Figure 38: TEM micrograph of a fluoroapatite crystal irradiated by 70 MeV Kr ions with a fluence of 9.5 10^{10} Kr.cm^{-2} **(a)** and x-ray diagram of a virgin sample showing the presence of texture **(b)**. The diagram has been measured during sample rotation around its normal.

As an example, a TEM image (Figure 38a) of a fluorapatite microcrystal taken with the electron beam parallel to the ion beam, shows the presence of latent tracks after Kr irradiation. The typical X-ray diagram of a virgin sample exhibits reinforced {hkℓ} reflections but low {00ℓ}s, as a sign of existence of a planar texture with **c**-axes of the hexagonal structure preferentially aligned parallel to the sample plane, with no preferred direction in this plane (Figure 38b). The texture is relatively smooth and all the peaks still appear in the diagram, even those corresponding to the **c**-axes, giving rise to an overall bad modelling, and

systematic deviations of the background at large θ values. This texture has to be corrected for in the Rietveld approach in order to carry out the best quantitative results, and particularly to determine volume fractions of the amorphous and crystalline phases.

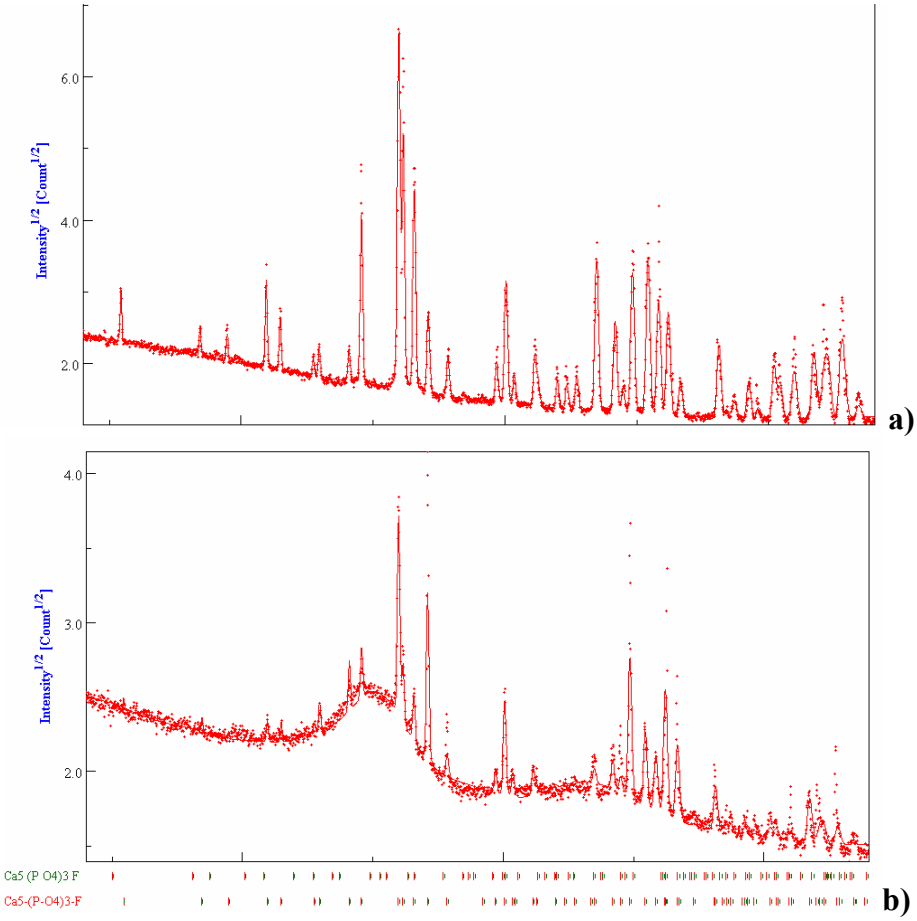

Figure 39: Same diagram as in Figure 38a with the application of an arbitrary texture correction model **(a)**, and 10^{13} Kr.cm^{-2} irradiated sample with 85 % of amorphous phase **(b)**

Figure 39a illustrates a fit with texture an arbitrary texture correction model for the virgin sample of Figure 39b. The experimental points are neatly better reproduced with the texture correction, which decreases the reliability factors from R_w and R_B = 21 % and 20 % respectively to the ones of Table 7 (first row). The described texture corresponds to SEM observations showing needle-like grain shapes with the needle axes aligned parallel to the sample plane.

For Kr irradiation, at the lowest fluence (10^{11} Kr.cm^{-2}), no drastic change in the X-ray diagrams could be observed indicating that the fraction of disordered matter remains smaller than 5%. However, no satisfactory cell parameters could be refined because of peak shifts, probably due to the presence of residual strains in the powder that were not measured using such scans. At such fluences elastic deformation is likely to exist which are difficult to take into account in the fit. Conversely (Figure 39b), for fluences ranging from 10^{12} to 5.10^{13} Kr.cm^{-2}, diffractograms exhibit clearly a broad contribution centred on the most intense peaks of diffraction and corresponding to a growing fraction of disordered matter (Table 7). This broad peak is shifting continuously towards low 2θ angles with increasing fluences, reaching 2θ = 30° for 5.10^{13} Kr.cm^{-2}. No change in the mean crystallite sizes accompanies the irradiation, indicating that the non-amorphous part of the ceramic remains undistorted except

for its volume. Indeed, no microstrains could be detected in the samples. As expected the increase in intensity of the broad peak is coupled to an overall decrease in the intensities of the diffraction peaks.

Fluence (ions.cm^{-2})	Vc/V (%)	A (Å)	C (Å)	<t> (nm)	$\Delta a/a_0$ (%)	$\Delta c/c_0$ (%)	R_w (%)	R_B (%)
0	100	9.3365(3)	6,8560(5)	294(22)	-	-	14.6	9.1
			Kr					
10^{11}	100	-	-	-	-	-		
10^{12}	100	-	-	-	-	-		
5.10^{12}	49(1)	9.3775(9)	6,8912(8)	294(20)	0.44	0.53	24	15
10^{13}	20(1)	9.4236(5)	6,9105(5)	291(20)	0.94	0.82	9.9	6
5.10^{13}	14(1)	9.3160(4)	6,8402(5)	294(22)	-0.21	-0.22	10.5	5.9
			I					
10^{11}	-	-	-	-	-	-		
5.10^{11}	86(2)	9.3603(3)	6.8790(5)	90(10)	0.26	0.35	23.9	15.1
10^{12}	-	-	-	-	-	-		
3.10^{12}	47(2)	9.3645(3)	6.8840(5)	91(6)	0.30	0.42	13.3	9
5.10^{12}	29.2(5)	9.3765(5)	6.8881(6)	77(11)	0.44	0.48	10.4	7.3
10^{13}	13.2(2)	9.3719(4)	6.8857(6)	82(9)	0.38	0.45	6.7	4.9

Table 7: Fitted parameters for the different samples irradiated under Kr and I ions with various fluences. Parentheses are one standard deviations.

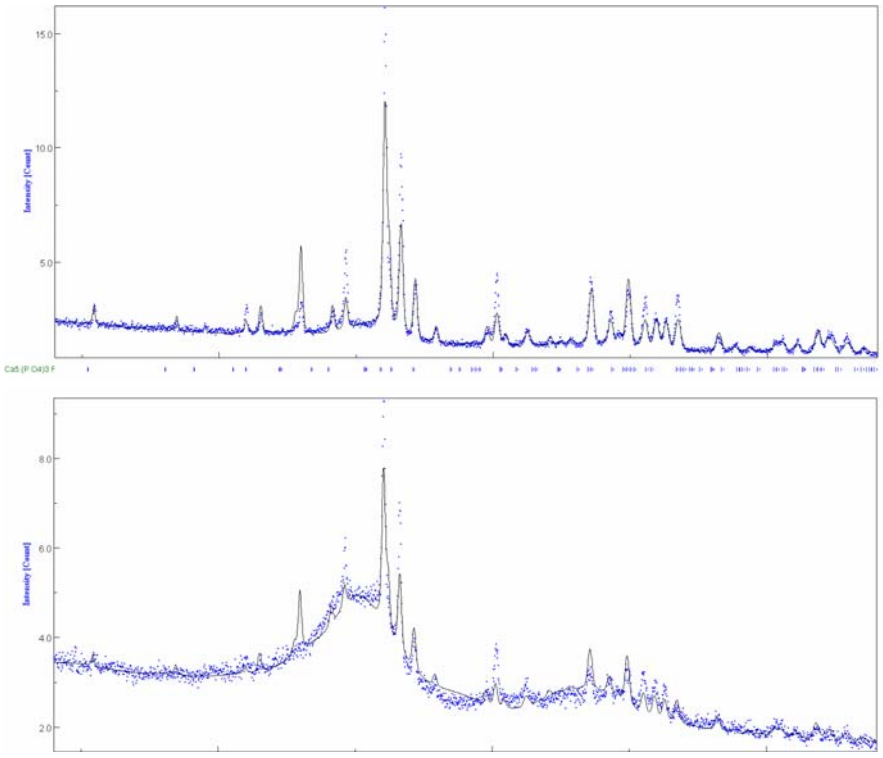

Figure 40: Rietveld refinements of **(a)** the least (5.10^{11} I.cm^{-2}) and **(b)** most (10^{13} I.cm^{-2}) I-irradiated samples, with arbitrary texture correction.

Iodine-irradiated samples (Figure 40) also exhibit an increase in amorphous phase with fluence, but starting at lower fluences (as soon as 5.10^{11} I.cm^{-2}) and with a different evolution. It is then expected a different behaviour to I-irradiation damaging. Interestingly the peak broadening is larger than for Kr-irradiation, mean isotropic crystallite sizes being around 2 times smaller. The iodine induced process creates more crystalline perturbation. Looking at

small angles for low fluence (Figure 40a), one can see some discrepancies in peaks positions with the actually refined parameters. This may also be the sign of residual strains present in a partially elastically deformed material, with the simultaneous presence of plastic zones corresponding to the amorphous volume.

Owing to previous electron microscopy observations [Paul et Fitzgerald 1992], latent tracks formed in the wake of Kr ions in the electron energy loss regime, must present an amorphous core which will account for the amorphisation of the fluorapatite through their overlapping. Whatever the ion used for irradiation, a strong increase in amorphous volume with fluence is observed. However, the results of the simulations show a clear difference between incident ions: upon increase in Kr fluence, a steep decrease in the crystalline phase amount is observed between 5.10^{12} and 10^{13} Kr.cm^{-2} (Table 7). Conversely, upon increase in iodine fluence, the decrease in crystalline phase amount is larger than for Kr-irradiation but exhibits a smoother evolution.

After a strong increase of the unit-cell with irradiation, for the highest doses, the unit-cell parameters of the crystalline phase are approximately coming back to their starting, non-irradiated values. Simultaneously, we do not observe any significant change in the mean crystallite size for Kr-irradiation. The increase in amorphous phase fraction is then associated to the unit-cell expansion up to a value for which the whole material relaxes into unstrained crystalline and amorphous phases. The elastic deformation increase of the crystalline phase up to the 10^{13} cm^{-2} fluence is fully relaxed for 5.10^{13} cm^{-2} in the case of the Kr irradiation. Such a process alone would tend to a progressive complete amorphisation of the material with decreasing crystallite sizes due to damages. However this is not observed, and the amorphised fraction gets saturated around 85% of the material. This is a good indication that another phenomenon competes with the amorphisation process. Heat exchanges are probably large during irradiation, which may promote recrystallisation and at least would explain the conservation of the mean crystallite sizes.

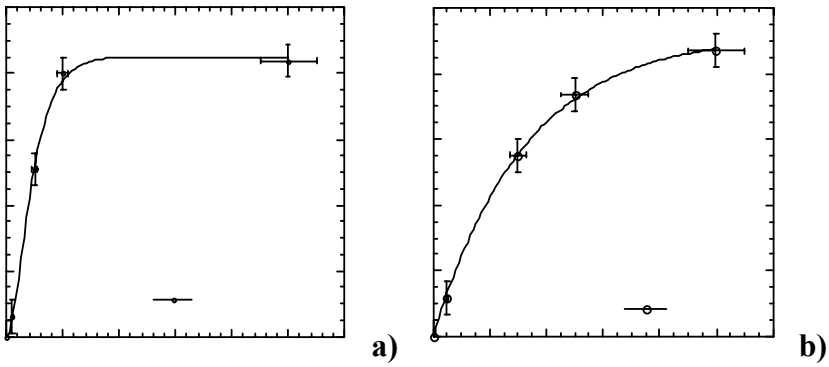

Figure 41: Damaged fraction as revealed by x-ray analyses for Kr- **(a)** and I-irradiated samples **(b)**.

Variations of the damaged fraction (Figure 41) in the material can be identified to the amorphous fraction Fd:

$$Fd = 1 - Fc$$

The damaged fraction for I-irradiated fluorapatite sinters can be fitted properly using a so-called single-impact model, with the classical Poisson's relation:

- 237

$$Fd = B[1 - \exp(-A\Phi t)]$$

$$A = -\pi r^2$$

where the cross section for amorphisation, A, allows the dtermination of the radius, r, of the ion tracks, and B is a maximum value of amorphisation characteristic of fluoroapatite. A second order relation, or double-impact model:

- 238

$$Fd = B[1 - (1 + A\Phi t)\exp(-A\Phi t)]$$

has to be used in the case of Kr irradiated samples [Miro et al. 2004, Table 8]. Consequently the amorphous track core radius are found to be somewhat larger after Kr double impact than after iodine single impact (Table 8). Also in both cases, B values, which correspond to the maximum amorphous fraction that can be obtained in fluorapatite for a given electronic energy loss, increase from Kr (≈ 85%) to iodine (≈ 92%) irradiation in agreement with the increase of the electronic stopping power. The fact that a complete amorphisation of fluorapatite cannot be obtained even for high fluences, confirms the defects autohealing behaviour of this material already quoted by Soulet et al. [1997] upon α irradiation.

	Krypton		**Iodine**
	Single impact	Double impact	Single impact
A (cm^2)	$1.85\ 10^{-13}$	$4.1\ 10^{-13}$	$3.3.10^{-13}$
r (nm)	2.4	3.6	3.2
B	0.87	0.85	0.92
χ2	0.013	0.0006	0.0004

Table 8: Radiation dammage fit results of Figure 41.

Table 7 also reveals an expansion of the cell parameters upon increase in the Kr fluence up to 10^{13} cm^{-2} . Above this fluence, for 5.10^{13} cm^{-2}, the cell parameters show a decrease and tend to recover the initial value. The latter result may be due to a partial annealing of defects above a fluence of 10^{13} cm^{-2}, annealing which induces saturation of the damage around 85% of amorphous phase for Kr-irradiation. The annealing of some defects results in a relaxation of stress on the remaining crystallized zones which thus recover the initial apatitic structural parameters. For iodine irradiation, the same behaviour of the crystalline fraction Fc parameters can be observed although less pronounced than for Kr-irradiation. This can be related to the difference in the damage creation mechanism between I and Kr irradiations quoted above: a single iodine impact allows creation of an amorphous core in latent tracks whereas a double Kr impact is necessary to amorphise the fluorapatite giving rise, after a single impact, to large domains of damage mainly built of stressed zones.

9.6.4. Texture of modulated structures

Modulated structures represent another difficulty for the spectra treatment, due to the appearance of satellite peaks. Their complete analysis needs to take account of such satellites

in a physically understandable way, which is at the present time only available in some Rietveld-based programs, like Jana [????]. The formalism used necessitates the description of the structure in a higher dimension space called super-space. However, in a first approximation, these structures can be represented in a supercell taking account of at least part of the modulations. Doing so, one can use any other program, and in particular programs that can work out the combined approach, as we will illustrate here.

Generally, satellites also preclude direct integration of peaks (as used in classical texture analysis), since they further enhance the peaks overlapping.

9.6.4.1. $Ca_3Co_4O_9$ ceramics

The thermoelectric modulated $Ca_3Co_4O_9$ (Co349) phase [Li *et al.* 1999], commonly formulated $[Ca_2CoO_3][CoO_2]_{1.62}$, ranges in the misfit aperiodic structures. A rigorous description of this phase was notably given from a 4D structure refinement of three polytype phases by Lambert *et al.* [2001]. From these results, a structural model was built concerning the main phase characterised by the previously reported cell parameters. This model was then confirmed using powder neutron diffraction data [Grebille *et al.* 2004] and the corresponding structural parameters were used to reconstruct a commensurate supercell approximant in the $P2_1/m$ space group, with $b \sim 8b_1 \sim 13b_2$ and a resulting unit cell of a = 4.8309 Å, b = 36.4902 Å, c = 10.8353 Å and β = 98.1317° (Figure 42), with 174 atoms per unit-cell.

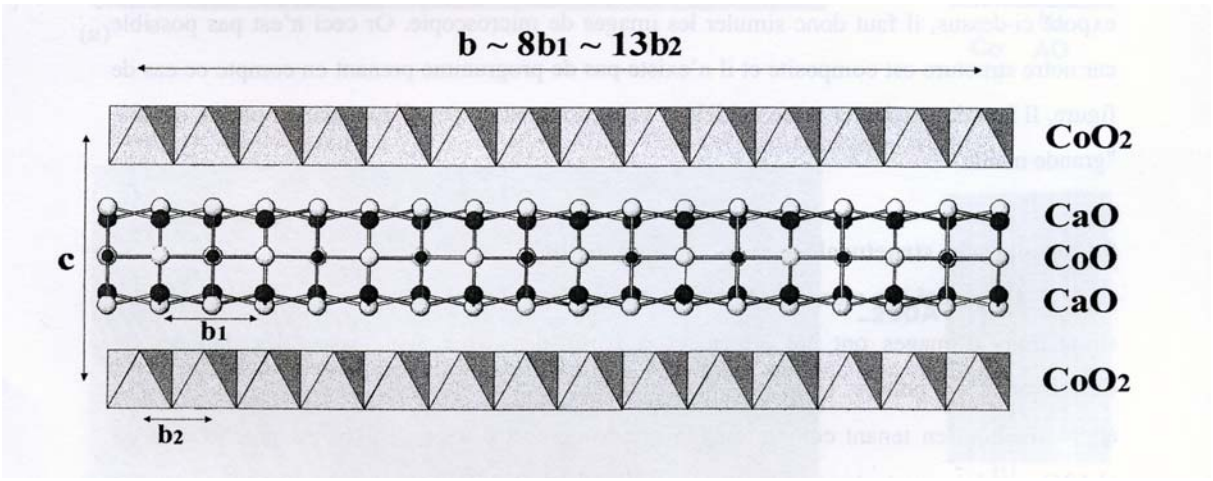

Figure 42: Used supercell approximant for the Co349 structure.

In such a structure the electrical conductivity in the (**a**,**b**) planes (σ_{ab}) is larger than along the **c** axes, which consequently enhances the thermoelectric Power Factor along (**a**,**b**) (PF_{ab}) compared to the one along **c**. It is then of importance to induce preferred orientations in such a manner that all (**a**,**b**) planes are parallel to each other in the ceramic. This can be operated using different ways. Under large magnetic fields, provided the unit-cell exhibits anisotropic paramagnetic susceptibilities (χ_{ab} and χ_c respectively along (**a**,**b**) planes and along the **c** axis) or that the crystallites are anisotropic in shape, the **c** axes will tend to align parallel or perpendicular to the field direction (depending on the ratio χ_{ab}/χ_c and on the crystallite shapes). Using Uniaxial Pressures (UP), anisotropically shaped crystals will tend to align with their larger dimensions perpendicular to the UP direction. For the Co349 phase, $\chi_{ab}/\chi_c < 1$, and **c** tends to orient with the field axis, while crystallites grow as platelets perpendicular to **c**,

which allow UP's to force **c** axes to align with the pressure direction. It is then possible to use both UP and magnetic fields to obtain large orientation degrees in this phase.

A magnetically c-axis aligned sample has been prepared by a slip-casting process using fine Co349 powder with average size of ~3μm in diameter. The Co349 fine powder obtained through a ball-milling process was mixed with solvent (water) and dispersant (polycarboxylic ammonium) to form a slurry. The slurry was cast into a cylindrical die under a magnetic field of 3T applied parallel to the cylinder axis. The slip-casted pellet was pressed in a cold isostatic condition at 392MPa and then heated at 200°C for 2h and 400°C for 3h in order to remove the solvent and dispersant completely. The resulting specimen was then hot-forged (880°C/20h/16MPa) under uniaxial pressure with pressure and magnetic field axes aligned parallel. The final dimensions of the sample are 25×15×4 mm^3.

The samples were measured on the D1B neutron line of the Institut Laüe Langevin, using a monochromatised wavelength of 2.523 Å. The χ angle scans for the observed fibre textures were operated from χ = 0 to 90° (step 5°) using a fixed incidence angle ω of 20.6° ({003} Bragg position), and measuring times around 20 mn per sample orientation.

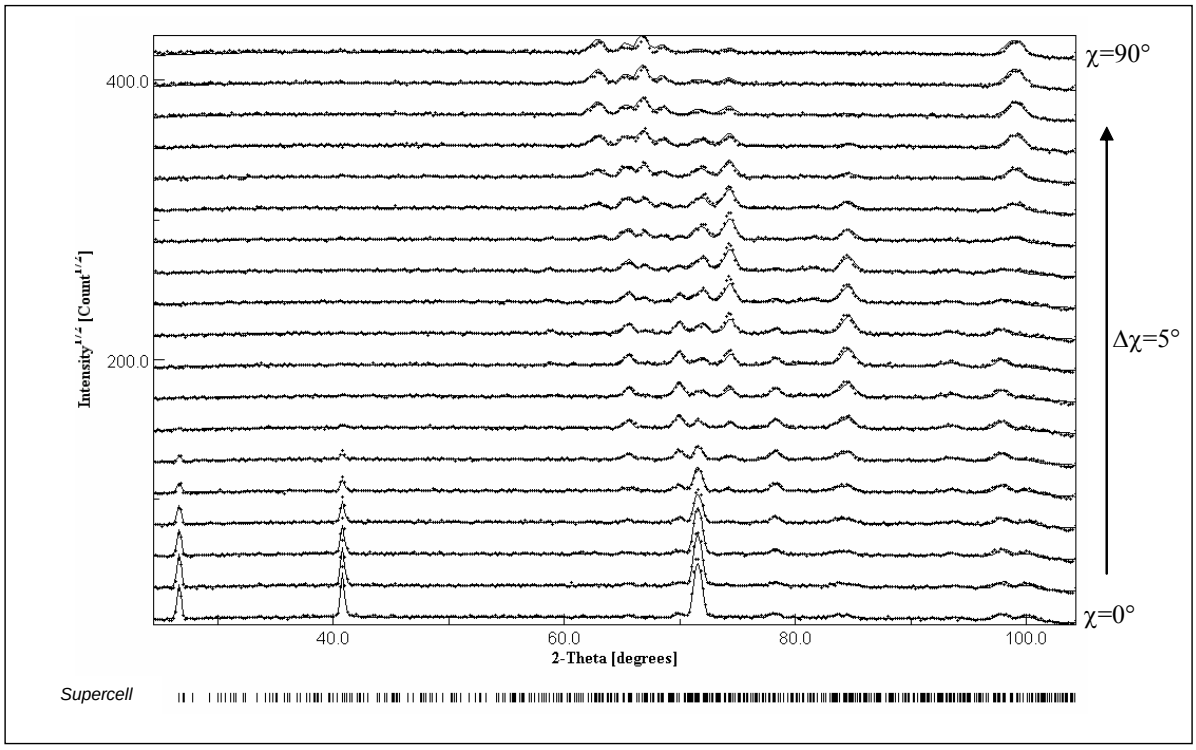

Figure 43: Experimental (dots) and calculated (lines) diagrams for the whole set of χ-scan measurements of a uniaxial stress and magnetically aligned Co349 ceramic

A reasonable reliability is obtained after refinement (Figure 43), with reliability factors of 19.7%, 12.4%, 11.9% and 8.3% respectively for RP_0, RP_1, R_w and R_B. The {003}, {-183} and {-201} calculated and experimental pole figures (Figure 44) attest for the good texture reliability. The inverse pole figure recalculated from the OD for the direction of the fibre (Figure 45) shows that a strong major orientation component is present with basal planes perpendicular to the stress direction, reaching a maximum density around 30 m.r.d.. Another minor texture component is present with a density around the random level, which corresponds to {±1k0} (k around 8) planes perpendicular to the stress direction.

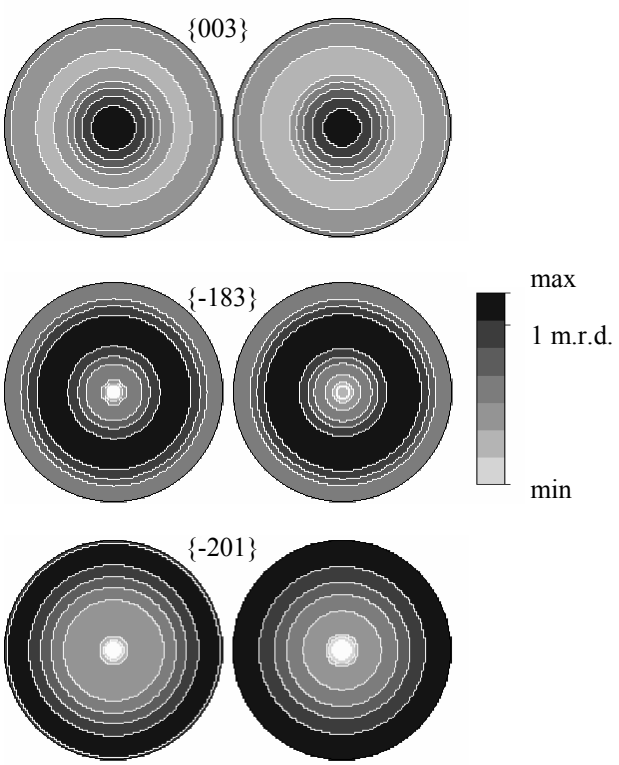

Figure 44: {003}, {-183} and {-201} experimental (left column) and recalculated (right column) neutron pole figures of the Co349 oriented ceramic. Logarithmic density scale, equal area projection, max density values are 32.5, 2.8 and 2.5 m.r.d. respectively, min density values are 0 m.r.d.

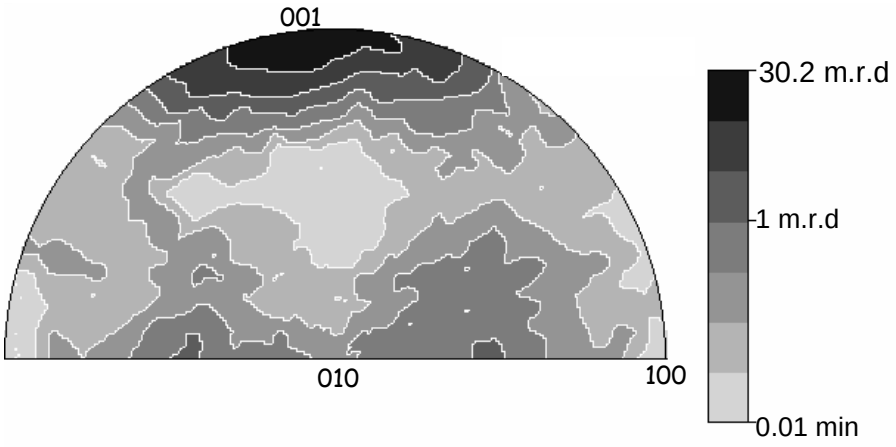

Figure 45: Inverse pole figure for the fibre direction of the Co349 oriented ceramic. Logarithmic density scale, equal area projection.

Using variable UP duration times, one can aim to increase the texture strengths of the components. The texture increase is correlated to an enhancement of TE properties (Fig. 7), with larger σ_{ab} and PF_{ab} values for larger pressures and UP duration times. In contrast, the values of S_{ab} are practically unchanged, so the increase in σ_{ab} is the major contribution to an enhancement of the PF_{ab}. The value of σ is reported to proportionally increase with increasing density.[38-40] However, our three samples have similar densities, *i.e.*, 4380 kg/m^3, 4580 kg/m^3

and 4380 kg/m^3 for samples 1, 2 and 3 respectively. Although it is also reported that the process-induced grain and crystallite size increase influences the transport properties,[41,26] the calculated crystallite sizes and observed grain sizes[16] were respectively similar for our ceramic samples. Therefore, if grain boundaries can affect the transport properties, it depends only on the texture development and the rearrangement of plate-like Co-349 grains by UP. The texture improvement appears here to be the main reason for the increase in σ_{ab} in our ceramic samples. The enhancement of texture would increase the contribution of the conduction path along the *ab*-plane with high σ and decrease that along the *c*-axis with low σ. The current texture analysis technique effectively reveals small differences in orientation degree even for highly-textured ceramics with $f \sim 1$. This demonstrates its importance in the exploitation of textured TE ceramics with enhanced TE properties. The electrical conductivity remains two times lower than in single crystals (~5×10^{-4} S/m) and proves that some efforts have still to be developed in the texturation of bulk textured TE materials.

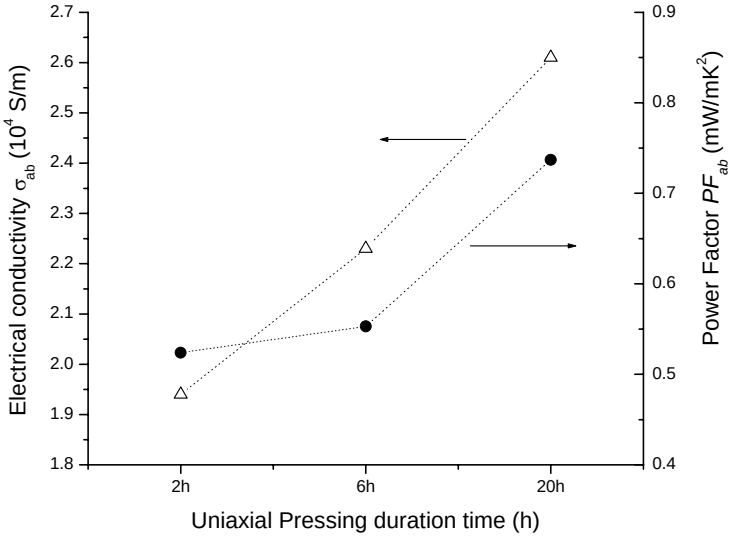

Figure 46: Variation of the electrical conductivity and thermoelectric power factor with UP duration time. Corresponding maxima of the {00ℓ} pole figures are 13.6, 19.8 and 31.8 m.r.d. for 2h, 6h and 20h of UP time respectively.

10 Macroscopic anisotropic properties

10.1. Aniso- and Iso-tropic samples and properties

In order that a given sample exhibits anisotropic macroscopic properties, two necessary conditions must be fulfilled. The first one is that the individual crystallites exhibit intrinsically the anisotropic property of concerns. But, in a polycrystalline aggregate, this intrinsic anisotropy of the crystals can be revealed at the macroscopic scale of the specimen only in the presence of texture. We can then distinguish 4 different types of samples:

- Randomly oriented specimen with isotropic crystallites (isotropic sample)
- Textured specimen with isotropic crystallites (textured isotropic sample)
- Randomly oriented specimen with anisotropic crystallites (isotropised sample)

- Textured specimen with anisotropic crystallites (anisotropic sample)

Texture is understood here as both morphological and crystallographic textures, since a specimen with randomly oriented crystals but with anisotropically aligned grain shapes (morphological texture) can still be macroscopically anisotropic, depending on the properties. For instance, in an isotropised sample, with a strong morphological texture and in absence of crystallographic texture, the interaction between neighbouring grains can result in mechanically anisotropic properties. The term quasi-isotropic is sometimes used for isotropised samples [Welzel et al. 2005], but the term "quasi" would let imagine that anisotropy is quite eliminated but not entirely. The latter term has the advantage, to our opinion, not to mislead the interpretation, but to clearly state the elaboration method has given the specimen a full isotropic character.

10.2. Macroscopic/Microscopic properties

10.2.1. $\vec{\mathcal{T}}^M$ and $\vec{\mathcal{T}}$ tensors

One of the main goals in non-destructively characterising real samples is the prediction of real properties achieved in a given sample, from the measured or refined parameters. Unfortunately, most of the time sustained models do not exist for the researched property, and in particular for crossed-properties (piezoelectricity, magnetoresistance ....). In that cases some literature is available which focuses on the correlation between the extracted parameters and the measured properties, though without modelling the macroscopic material behaviour.

As a general trend, macroscopic scale simulation aims at providing some methodology to model a given macroscopic property, taking the tensorial form $\vec{\mathcal{T}}^M$, from the microscopic, intrinsic properties of the individual crystallites. These latter are characterised by the tensor $\vec{\mathcal{T}}$ of the same order as $\vec{\mathcal{T}}^M$. The link between these two quantities is mainly the concern of preferred orientations, in a general meaning, *i.e.* including crystallographic and morphological textures.

10.2.2. Microscopic properties

10.2.2.1. Extensive and Intensive variables

In thermodynamic we classify two types of variables, depending on their dependence on the mass m, or not. Intensive variables are not depending of the mass of the system. These are for instance the temperature T, pressure p, elastic stress σ^{ij}, electric field E^i , ... When such variables represent tensorial properties, they are represented by superscripts contravariant tensors. Extensive variables are depending on the mass, like entropy S, volume V, elastic strain ε_{ij}, electric induction D_i ..., and tensorial properties are represented by covariant tensor subscripts.

10.2.2.2. Work element of conjugated variables

Variables form conjugated couples, which are associated to give an elementary work dW:

- 239 $$dW = \xi \, d\Gamma$$

for wich ξ and Γ are intensive and extensive variables respectively. For instance, the mechanical work element is $\delta W = \sigma^{ij} \, d\varepsilon_{ij}$, thermal work element $\delta W = T \, dS$ or the electrical work element $\delta W = E^i \, dD_i$.

10.2.2.3. Generalised Energy and Free Enthalpy

The energy element dU of a system can then be represented from the first principle of thermodynamics in its general form by:

- 240 $$\begin{aligned} dU &= dQ + \delta W \\ &= T \, dS + E^i \, dD_i + \sigma^{ij} \, d\varepsilon_{ij} + ... \end{aligned}$$

for which dQ is the caloric elemental variation, the term p dV as been neglected for a solid, and the equation extends to as many energetic contributions exist (magnetic, piezoelectric ...). The generalised energy variation expresses variations of the extensive variables. The second principle obviously gives rise to the definition of free enthalpy, G, generalised to all energetic contributions of the solid:

- 241 $$G = U - TS - E^i \, dD_i - \sigma^{ij} \, d\varepsilon_{ij} - ...$$

and its derivative:

$$dG = dU - T \, dS - E^i \, dD_i - \sigma^{ij} \, d\varepsilon_{ij} - ... - S \, dT - D_i \, dE^i - \varepsilon_{ij} \, d\sigma^{ij} - ...$$

in which the first part of the right hand-side member is 0 ($\delta W - \delta W$):

- 242 $$dG = -S \, dT - D_i \, dE^i - \varepsilon_{ij} \, d\sigma^{ij} - ...$$

which takes into account the variations of all the intensive variables.

10.2.2.4. Thermal properties

Since $dQ = T \, dS = C \, dT$, where C is the molar capacity, thermal properties are represented by zero-order tensors (scalar), and they are isotropic whatever the crystal system.

10.2.2.5. Electric properties

Electric induction and field are vectors (1st order tensors), then linked by the 2nd order dielectric tensor constant κ_{ij}:

- 243 $$D_i = \kappa_{ij} \, E^j$$

which implies, for the equilibrium condition dG = 0, that $\partial D_i / \partial E^j = \partial D_j / \partial E^i$, and consequently one gets the symmetrisation of κ_{ij}: $\kappa_{ij} = \kappa_{ji}$. This tensor contains 6 different components for the triclinic crystal system, while symmetric operators reduce the number of independent values (Table 9).

Triclinic	Monoclinic	Orthorhombic	Tetragonal, trigonal, hexagonal	Cubic, Gyrotropic Isotropic
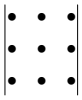	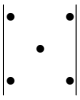		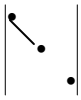	

Table 9: Nye representation for the κ_{ij} dielectric tensor for all crystal classes

10.2.2.6. Mechanical properties

Mechanical (elastic) properties are represented by the fourth order tensors called compliances $S_{ijk\ell}$ and stiffnesses $C_{ijk\ell}$ that link elastic strains ε_{ij} and stresses $\sigma^{k\ell}$:

$$\varepsilon_{ij} = S_{ijk\ell}\, \sigma^{k\ell}$$

$$\sigma^{ij} = C_{ijk\ell}\, \varepsilon_{k\ell}$$

$S_{ijk\ell}$ and $C_{ijk\ell}$ possess a priori 3^4 independent components, which reduces with the condition $S_{ijk\ell} = S_{k\ell ij}$ because of the equilibrium at dG = 0 which imposes $\partial\varepsilon_{ij} / \partial\sigma^{k\ell} = \partial\, \varepsilon_{k\ell} / \partial\, \sigma^{ij}$. However, since the stresses are defined relatively to the force element dF_i of direction i to a surface element dS_j, by $dF_i = \sigma^{ij}\, dS_j$ (Figure 47a), one can see that for mechanical equilibrium the condition on a specific surface, *e.g.* (2,3), (Figure 47b) imposes $\sigma^{23} = \sigma^{32}$. By extension to all surfaces, the condition $\sigma^{ij} = \sigma^{ji}$ must be satisfied. The same stands for deformations, and one obtains $\varepsilon_{k\ell} = \varepsilon_{\ell k}$. As a result, the compliance tensor obei the relation $S_{ijk\ell} = S_{k\ell ji} = S_{jik\ell} = S_{ij\ell k}$, and contains only 21 independent parameters.

Because of this symmetry a conventional notation has been developed which affects the following correspondence between indices: 11 → 1; 22 → 2; 33 → 3; 23 → 4; 13 → 5; 12 → 6. This results in 6x6 matrices, s_{ij} and c_{ij} respectively for S_{ijkl} and C_{ijkl}, representation with i's as rows and j's as columns. This engenders specific relationships for the compliance and stiffness constants (Figure 48).

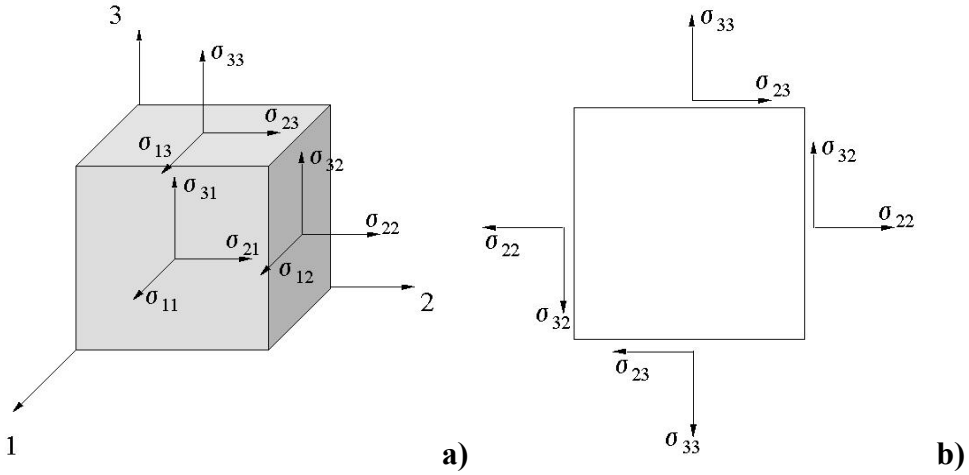

Figure 47: Stress definition relative to the three axes 1, 2 and 3 **(a)**, and projection on the (2,3) plane **(b)**. σ^{ij}: i is the force direction, j is the surface normal to which the force is applied

$$\begin{vmatrix} S_{1111} & S_{1122} & S_{1133} & S_{1123} & S_{1113} & S_{1112} \\ & S_{2222} & S_{2233} & S_{2223} & S_{2213} & S_{2212} \\ & & S_{3333} & S_{3323} & S_{3313} & S_{3312} \\ & & & S_{2323} & S_{2313} & S_{2312} \\ & & & & S_{1313} & S_{1312} \\ & & & & & S_{1212} \end{vmatrix} \begin{vmatrix} s_{11} & s_{12} & s_{13} & s_{14}/2 & s_{15}/2 & s_{16}/2 \\ & s_{22} & s_{23} & s_{24}/2 & s_{25}/2 & s_{26}/2 \\ & & s_{33} & s_{34}/2 & s_{35}/2 & s_{36}/2 \\ & & & s_{44}/4 & s_{45}/4 & s_{46}/4 \\ & & & & s_{55}/4 & s_{56}/4 \\ & & & & & s_{66}/4 \end{vmatrix} \textbf{a)}$$

$$\begin{vmatrix} C_{1111} & C_{1122} & C_{1133} & C_{1123} & C_{1113} & C_{1112} \\ & C_{2222} & C_{2233} & C_{2223} & C_{2213} & C_{2212} \\ & & C_{3333} & C_{3323} & C_{3313} & C_{3312} \\ & & & C_{2323} & C_{2313} & C_{2312} \\ & & & & C_{1313} & C_{1312} \\ & & & & & C_{1212} \end{vmatrix} \begin{vmatrix} c_{11} & c_{12} & c_{13} & c_{14} & c_{15} & c_{16} \\ & c_{22} & c_{23} & c_{24} & c_{25} & c_{26} \\ & & c_{33} & c_{34} & c_{35} & c_{36} \\ & & & c_{44} & c_{45} & c_{46} \\ & & & & c_{55} & c_{56} \\ & & & & & c_{66} \end{vmatrix} \textbf{b)}$$

Figure 48: Correspondence between tensor (left-hand side) and matrix (right-hand side) notations for the compliance (**a)** and stiffness **(b)** constants

Triclinic	Monoclinic	Orthorhombic 222	Orthorhombic mm2, mmm	Tetragonal 4, $\bar{4}$, 4/m
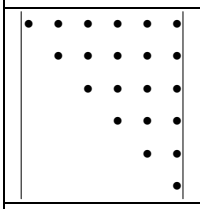	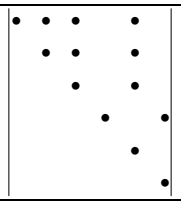	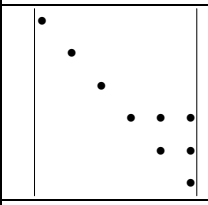	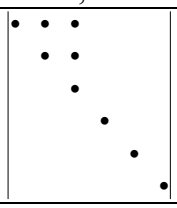	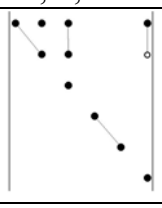
Tetragonal 422, 4mm, 42m, 4/mmm	Trigonal 3, $\bar{3}$	Trigonal 32, 3m, $\bar{3}$m	Hexagonal	Cubic
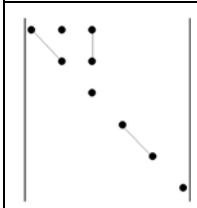	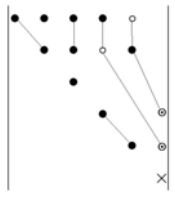	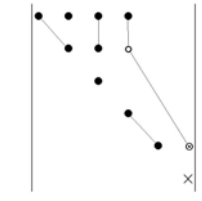	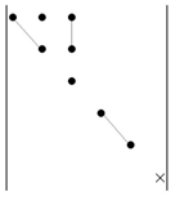	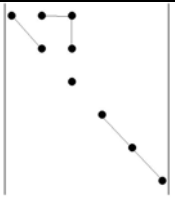
Isotropic				

Gyrotropic				
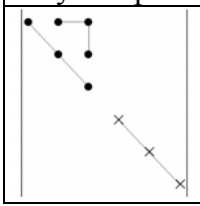				

Table 10: Nye representation for the $S_{ijk\ell}$ compliance tensor for all crystal classes

10.2.3. Macroscopic properties modelling

10.2.3.1. Averaging of tensors

10.2.3.1.1. Volume average

The volume average of a tensorial quantity $\mathcal{T}$, which varies inside the volume V of consideration can be calculated by:

- 245
$$\langle \mathcal{T} \rangle = \frac{1}{V} \int_{V} \mathsf{T}\, dV \,,$$

In general, tensors are considered constant inside individual grains, and the previous equation rewrites:

- 246
$$\langle \mathcal{T} \rangle = \frac{1}{V} \sum_{i} \mathsf{T}\, \mathrm{V_i} \,,$$

for which V_i/V represents the volume fraction or weight associated to each grain i in the volume. It is interesting to notice that using such arithmetic averaging procedures, the average of the inverse of the tensor is in general not equivalent to the inverse of the averaged tensor:

- 247
$$\left\langle \mathcal{T}^{-1} \right\rangle = \frac{1}{V} \sum_{i} \mathcal{T}^{-1}\, \mathrm{V_i} \neq \langle \mathcal{T} \rangle^{-1}$$

Then, if the tensor is aimed at representing a physical property, the average of it being the macroscopic tensor $\mathcal{T}^{M}$ representing the polycrystal property, it is of crucial importance to determine which of the averaging procedures is a correct approach.

10.2.3.1.2. Arithmetic average over orientations

Since tensor properties are by essence depending on the crystal orientations, for polycrystalline textured samples one has to account for the volume fractions of grains in the different orientations g. Using the help of the ODF (Eq. - 106), Equation - 245 rewrites:

- 248
$$\langle \bar{\mathcal{T}} \rangle = \int_g \bar{\mathcal{T}}(g)\, f(g)\, dg$$

where g varies in all the orientation space $\mathscr{A}$. This equation is valid if the tensorial properties are kept constant inside each individual crystallite, and leads to the same ambiguity as in Eq. - 247 that $\left\langle (\bar{\mathcal{T}})^{-1} \right\rangle \neq \left\langle \bar{\mathcal{T}} \right\rangle^{-1}$ in general.

10.2.3.1.3. Geometric average over orientations

In order to remove the previous ambiguity, one has to imagine another approach for the averaging procedure.

10.2.3.1.3.1. Scalar case

A zero-order tensor, or scalar b, can always be decomposed into a linear combination of all its N possible values b_k, each of them being associated to a given probability, or weight, w_k. Its arithmetic average is then:

- 249
$$\langle b \rangle = \sum_{k=1}^{N} b_k w_k \text{, with } \sum_{k=1}^{N} w_k = 1$$

The corresponding geometric mean of this scalar takes the form:

- 250
$$\lceil b \rceil = \prod_{k=1}^{N} b_k^{\,w_k} = \exp\left(\langle \ln b \rangle\right), \text{ with}$$
$$\langle \ln b \rangle = \sum_{k=1}^{N} \ln b_k w_k$$

10.2.3.1.3.2. 2nd order tensors case

Considering matrices the previous approach of the geometric mean is not straightforward. For the eigenvalues λ_I of a given matrix $\bar{\mathcal{T}}$, Eq. - 250 rewrites:

- 251
$$\lceil \lambda_I \rceil = \prod_{k=1}^{N} \lambda_k^{\,w_{i,k}}$$

which ensures that $\lceil \lambda_I \rceil = 1/\lceil 1/\lambda_I \rceil = \lceil \lambda_I^{-1} \rceil^{-1}$. For the matrix $\bar{\mathcal{T}}$ represented in its orthonormal basis of eigenvectors, it can be shown (Matthies et Humbert 1995) that:

- 252
$$\lceil \bar{\mathcal{T}} \rceil_{ij} = \exp(\langle \ln \bar{\mathcal{T}} \rangle_{i'j'})$$
$$= \exp(\langle \Theta \rangle_{ij,i'j'} \ln \bar{\mathcal{T}}_{i'j'})$$

In this equation, Θ stands for the transformation applied to the tensor $\mathcal{T}$, that represents the property of a given single crystal of orientation g in the single crystal reference frame K_B, in order to bring it coincident to the sample reference frame K_A. Θ then depends on the tensor order, and its average is composed of elements $<\Theta>_{ij}$ given by, similarly as in Eq. - 248:

- 253
$$\left\langle \Theta \right\rangle_{ij,i'j'} = \int_g \Theta_i^{i'}(g)\Theta_j^{j'}(g)\, f(g)\, dg$$

10.2.3.2. Thermal properties

Since thermal properties are scalar the macroscopic thermal properties are not depending on crystallite orientations. Hence, if no other effect is present in the material, $C^M = C$.

10.2.3.3. Mechanical properties

Modelling of the mechanical properties has concentrated most of the works of macroscopic anisotropic property modelling, in geology and metallurgy. We describe here the main models.

10.2.3.3.1. The Voigt model

Voigt (1928) assumes that the distribution of strains is homogeneous inside the material, i.e. all the crystallites are deformed in exactly the same way, with a strain tensor ε_{ij}. Consequently the strain is continuous at the grain boundaries. In order to respect this homogeneity condition for crystallites that are not oriented identically, the stress tensor is then different in each differently oriented crystallite. Stresses are then discontinuous at grain boundaries and violate mechanical stress equilibrium.

This model implies $\varepsilon_{ij}^M = \varepsilon_{ij} = <\varepsilon_{ij}>$. The average is calculated using Eq. - 248 for a textured polycrystal, which combined with Eq. - 244 gives:

- 254
$$<C_{ijk\ell} : \varepsilon_{ij}> = C_{ijk\ell}^M : \varepsilon_{ij}^M$$

and it turns out that in order for this equation to be valid for any given strain ε_{ij}, the following condition applies:

- 255
$$C_{ijk\ell}^M = <C_{ijk\ell}>$$

The elastic macroscopic stiffness tensor is then the average of the intrinsic tensor in the Voigt model. In such a way, strain compatibility is satisfied, but at the expense of stress equilibrium. This imposes an upper bound for $C_{ijk\ell}^M$ which will be refered to as $C_{ijk\ell}^V$.

10.2.3.3.2. The Reuss model

Reuss [1929] assumes that the distribution of stress is homogeneous inside the material, i.e. all the crystallites are stressed in exactly the same way, with a stress tensor $\sigma^{k\ell}$. Consequently the stress is continuous at the grain boundaries. In order to respect this homogeneity condition for crystallites that are not oriented identically, the strain tensor is then different in each differently oriented crystallite. Strains are then discontinuous at grain boundaries and violate strain compatibility.

This model implies $\sigma^{k\ell M} = \sigma^{k\ell} = <\sigma^{k\ell}>$. The average is calculated using Eq. - 248 for a textured polycrystal, which combined with Eq. - 244 gives:

- 256
$$<C_{ijk\ell}^{-1} : \sigma^{k\ell}> = (C_{ijk\ell}^{M})^{-1} : \sigma^{k\ell M}$$

and it turns out that in order for this equation to be valid for any given stress $\sigma^{k\ell}$, the following condition applies:

- 257
$$C_{ijk\ell}^{M} = <C_{ijk\ell}^{-1}>^{-1}$$

The elastic macroscopic stiffness tensor is then the inverse of the average of the inverse intrinsic tensor in the Reuss model. In such a way, stress equilibrium is satisfied, but at the expense of strain compatibility. This imposes an upper bound for $(C_{ijk\ell}^{M})^{-1}$, then a lower bound for $C_{ijk\ell}^{M}$, refered to as $C_{ijk\ell}^{R}$. Care should be taken in comparing tensors in the mean of lower and upper bounds. Since we are dealing with tensorial quantities, this does not necessarily means that all the tensor components have to be lower, or resp. larger.

Since the average of the inverses is not in general equal to the inverse of the average, the Voigt and Reuss approaches do not give the same results, except for isotropic and textured isotropic samples, for which the tensors are independent of the orientation. However, they define a limit interval for the elastic tensors which can be used.

10.2.3.3.3. The Hill model

As just said, Voigt and Reuss averages only coincide for isotropic or textured isotropic samples. In any other case they define upper and lower bounds for the elastic constants. Hill [1952] proposed to use an arithmetic mean of the Voigt and Reuss macroscopic elastic constants in order to more closely represent experimental data:

- 258
$$C_{ijk\ell}^{H} = \xi C_{ijk\ell}^{V} + (1-\xi) C_{ijk\ell}^{R} \text{ or}$$
$$S_{ijk\ell}^{H} = \xi S_{ijk\ell}^{V} + (1-\xi) S_{ijk\ell}^{R}$$

Hill uses $\xi = 1/2$, but any other value can *a priori* be used, since the model is purely empirical and will depend on the sample. This estimate of the macroscopic constants neither fulfils strain and stress homogeneity nor it ensures that the macroscopic compliance is the inverse of the macroscopic stiffness.

10.2.3.3.4. The geometric mean model

Because we are dealing with real and symmetric tensors, the eigenvalues of the concerned tensors are real. But neither the $S_{ijk\ell}$ and $C_{ijk\ell}$ nor the s_{ij} and c_{ij} matrices are

diagonal, and Eq. - 252 cannot be used in its actual state. One should first diagonalise them using an orthonormal basis of eigentensors $\mathbf{b}_{ij}^{(\lambda)}$, for instance in the case of the stiffness tensor $C_{ijk\ell}$ of eigenvalues $C^{(\lambda)}$:

- 259

$$((\mathbf{b}_{ij}^{(\lambda)})^{-1}\, C_{ijk\ell}\, \mathbf{b}_{k\ell}^{(\lambda)}) = C^{(\lambda)}\, \delta_{ij} \text{ and}$$

$$C_{ijk\ell} = \sum_{\lambda=1}^{6} C^{(\lambda)} \mathbf{b}_{ij}^{(\lambda)} \mathbf{b}_{k\ell}^{(\lambda)} \text{ which extends to}$$

$$(\ln C)_{ijk\ell} = \sum_{\lambda=1}^{6} \ln(C^{(\lambda)}) \mathbf{b}_{ij}^{(\lambda)} \mathbf{b}_{k\ell}^{(\lambda)}$$

$$= \ln\left[\prod_{\lambda=1}^{6} (C^{(\lambda)})^{\mathbf{b}_{ij}^{(\lambda)} \mathbf{b}_{k\ell}^{(\lambda)}} \right]$$

Now applying the geometric average over orientations (Eq. - 252), the macroscopic stiffness of the polycrystal can be calculated from:

- 260

$$C_{ijk\ell}^{M} = \lceil C \rceil_{ijk\ell} = \exp(\langle \ln C \rangle_{i'j'k'\ell'})$$

$$= \exp(\langle \Theta \rangle_{ijk\ell,i'j'k'\ell'} (\ln C)_{i'j'k'\ell'})$$

with

$$\langle \Theta \rangle_{ijk\ell,i'j'k'\ell'} = \int_{g} \Theta_{i}^{i'}(g) \Theta_{j}^{j'}(g) \Theta_{k}^{k'}(g) \Theta_{\ell}^{\ell'}(g)\, f(g)\, dg$$

and $(\ln C)_{i'j'k'\ell'}$ is given by Eq. - 259. However, before calculating the wanted value $\lceil C \rceil_{ijk\ell}$, one has to first diagonalise $\langle \ln C \rangle_{i'j'k'\ell'}$ in order to extract the new eigenvalues and eigentensors for the oriented polycrystal. The four successive tensor transformations relate to the 4th order stiffness tensor character.

The factorial entering the calculation explains the term "geometric mean", in the sense that the oriented polycrystal macroscopic stiffness is obtained by the mean averaging of the single crystal stiffness eigenvalues. Similar expressions can be obtained for the macroscopic compliance tensor $S_{ijk\ell}^{M}$ which admits as eigenvalues $S^{(\lambda)} = 1/C^{(\lambda)}$ the reciprocal of the stiffness eigenvalues. This waranties that the same macroscopic elastic properties are calculated when using stiffness or compliances in the geometric mean approach. In other words, the average of the inverse macroscopic property is consistent with the inverse of the average macroscopic property. This may be the reason why this modelling gives rather good estimates of the elastic properties (Matthies et Humbert 1995), comparable to ones obtained by more sophisticated models which require larger calculation times, somehow not suitable for implementation in routinely achieved combined algorithm.

References

Abeles F. (1950), *Annales de Physique* **5** 596-???

Akaike H. (1974), *IEEE Transactions in Automatism and Control AC***19** 716-723

Alexander L.E. (1948), *Journal of Applied Physics* **19** 1068-???

Alexander L.E. (1950), *Journal of Applied Physics* **21** 126-???

Alexander L.E. (1955), *Journal of Applied Physics* **25** 155-???

Als-Nielsen J. (1985), *Zeitschrift fur Physik B* **61** 411-???

Antoniadis A., Berruyer J., Filhol A. (1990), *Acta Crystallographica* **A46** 692-711

Aouinti M., Chateigner D., Gibaud A., Poncin-Epaillard F. (2002), *Materials Science Forum* **408-412** 1579-1584

Auzary S., Badawi F., Bimbault L., Rabier J., Gaboriaud R.J., Goudeau P. (1997). *Journal de Physique III* **7** 35-46

Badawi F., Durand N., Goudeau P., Pelosin V. (1994), *Applied Physics Letters* **65** 3075-3077

Baerlocher C. (1993), in "*Proceedings of International Conference on Zeolithes*" (Butterworths, London)

Balzar D., Popovic S. (1996), *Journal of Applied Crystallography* **29** 16-23

Banerjee S., Gibaud A., Chateigner D., Ferrari S., Wiemer C., Dekadjevi D.T. (2002), *Applied Physics Letters* **80** 512-515

Baumbach T., Mikulik P. (1999), in "*X-ray and neutron reflectivity: principles and applications*", Edited by J. Daillant and A. Gibaud, Springer M58, p 232-280

Beauvy M, et al, (1998), *Journal of Alloys and Compounds* **271-273** 557-???

Bérar J.-F., Baldinozzi G. (1993), *Journal of Applied Crystallography* **26** 128

Bernouilli D. (1861), *Biometrika* **48** 3-13

Born, M., Wolf, E. (1980), in "*Principles of Optics*", Pergamon, London 6th Edition

Boultif A., Louer D. (1991), *Journal of Applied Crystallography* **24** 987-993

Boultif A., Louer D. (2004), *Journal of Applied Crystallography* **37** 724-731

Bowen D., Wormington M. (1993), *Advances in X-ray Analysis* **36** 171

Bowman K.J., Mendendorp M.N. (1994), *Advanced in X-ray Analysis* **37** 473

Bragg W.L. (1912), *Proceedings Camp. Philosophical Society* **17** 43

Bunge H.-J. (1969), "*Mathematische Methoden der Texturanalyse*", Berlin, Akademie Verlag.

Bunge H.-J. (1982), "*Texture Analysis in Materials Science*", P.R. Morris Trans., Butterworths, London.

Bunge H.-J., Esling C. (1982), "*Quantitative Texture Analysis*", Bunge and Esling Ed., DGM, Germany.

Bunge H.-J., Wenk H.-R., Pannetier J. (1982), *Textures and Microstructures* **5** 153-170

Caglioti G., Paoletti A., Ricci F.P. (1958), *Nuclear Instrumentation* **3** 223-???

Capkova P., Peschar R., Schenk H. (1993), *Journal of Applied Crystallography* **26** 449-452

Cardwell D.A. (1998), *Materials Science & Engineering B***53** 1-10

Cerny R, Valvoda V., Cladek M. (1995), *Journal of Applied Crystallography* **28** 247-253

Chateigner D. (1994), *"Texture cristallographique de céramiques et de couches minces supraconductrices $Yba_2Cu_3O_{7-\delta}$ en relation avec les propriétés physiques",* Thesis, Université J. Fourier, Grenoble-France.

Chateigner D. (2000), "*Quantitative Texture Analysis, a pot Pourri*", Habilitation, Université du Maine, Le Mans-France.

Chateigner D. (2002), POFINT: a MS-DOS program for Pole Figure Interpretation. http://www.ecole.ensicaen.fr/~chateign/qta/pofint/

Chateigner D. (2002a), STROTEX and Phiscans: MS-DOS programs for pole figure visualisation and integration.

Chateigner D., Germi P., Pernet M. (1992), *Journal of Applied Crystallography* **25** 766-769
Chateigner D., Germi P., Pernet M. (1994), *Materials Science Forum* **157-162** 1379-1386
Chateigner D., Germi P., Pernet M. (1994a). *Journal of Applied Crystallography* **27** 278-282
Chateigner D., Lutterotti L., Hansen T. (1998), *ILL Highlights **1997*** 28-29.
Chateigner D., Wenk H.-R., Patel A., Todd M., Barber D.J. (1997), *Integrated Ferroelectrics* **19** 121-140
Chateigner D., Wenk H.-R., Pernet M. (1997a), *Journal of Applied Crystallography* **30** 43-48
Cheary R.W., Cline J.P. (1994), *Advances in X-ray analysis* **38** ???
Chen F.H., Koo H.S., Tseng T.Y. (1991), *Applied Physics Letters* **58** 637-???
Clemens B.M., Bain, J.A. (1992). *Materials Research Society Bulletin* **17** 46-51
Compton A.H. (1923), *Philosophical Magazine* **45** 112-???
Cont L., Chateigner D., Lutterotti L., Ricote J., Calzada M.L., Mendiola J. (2002), *Ferroelectrics* **267** 323-328
Cransvick L. (1999), http://www.ccp14.ac.uk/mirror/mirror.htm
Croce P., Névot L. (1976), *Revue de Physique Appliquée* **11** 113-125
Cullity B.D. (1978), in "*Elements of X-ray diffraction*", p. 447. Addison-Wesley Publishing Company
Dahms M., Bunge H.J. (1988), *Textures and Microstructures* **10** 21-???
Daillant J., Bélorgey O. (1992), *Journal of Chemical Physics* **97** 5824-5835
De Boer D.G. (1994), *Physical Review B* **49** 5817-5820
De Rango P., Lees M.R., Lejay P., Sulpice A., Tournier R., Ingold M., Germi P., Pernet M. (1991), *Nature* **349** 770-771
De Wolff P.M. (1957), *Acta Crystallographica* **10** 590-595
De Wolff P.M. (1968), *Journal of Applied Crystallography* **1** 108-113
Delhez R., Keiser T.H., Langford J.I., Louër D., Mittemeijer E.J., Sonneveld E.J. (1993), "*Monographs on Crystallographers and Crystallography*", **5**
Deutsch M., Ocko B.M. (1998), *Encyclopedia of Applied Physics* **23** 479-489
Dietrich S., Haase A. (1995), *Physics Reports* **260** 1-???
Dimos D., Chaudhari P., Mannhart J., Legoues F.K. (1988), *Physical Review Letters* **61** 219-???
Dollase W.A. (1986), *Journal of Applied Crystallography* **19** 267-272
Dong C., Wu F., Chen H. (1999), *Journal of Applied Crystallography* **32** 850-853
Dusek M., Petrícek V., Wunschel M., Dinnebier R.E., van Smaalen S. (2001), *Journal of Applied Crystallography* **34** 398-404
Eberhart J.-P. (1989), "*Analyse Structurale et Chimique des Matériaux*" Dunod Ed.
Erwing R., Weber W., Clinard Jr F. (1995), *Progress in Nuclear Energy* **29** 63-???.
Esling C., Muller J., H.-G. Bunge (1982), *Journal de Physique* **43** 189-???
Feng Y., Zhu M., Liu F., Liu J., Han H., Han Y. (2001), *Thin Solid Films* **395** 213-216
Finger L.W., Cox D.E., Jephcoat A.P. (1994), *Journal of Applied Crystallography* **27** 892-900
Fisher R.A. (1922), *Philosophical Transactions of the Royal Society of London Series A* **222** 309-360
Gergaud P. (1992). PhD Thesis, E.N.S.A.M. of Paris, France
Gibaud A. (1999), in "*X-ray and neutron reflectivity: principles and applications*", Edited by J. Daillant and A. Gibaud, Springer M58, p 87-120
Gibaud A., Vignaud G., Sinha S.K. (1993), *Acta Crystallographica A* **49** 642-648
Guilmeau E., Chateigner D., Noudem J.G. (2002), *Superconductor Science & Technology* **15** 1436-???

Guilmeau E., Chateigner D., Noudem J.G. (2003), *Superconductors Science & Technology* **16** 484-491
Guilmeau E., Lambert S., Chateigner D., Noudem J., Ouladdiaf B. (2003), *Materials Science and Engineering B* **104** 107-112
Guinier A. (1963), "*X-ray diffraction*", W. H. Freeman, San Francisco
Hamley I.W., Pedersen J.S. (1994), *Journal of Applied Crystallography* **27** 29-35
Hauk V. (1997), editor, "*Structural and residual stress analysis by non-destructive methods: evaluation, application, assessment"* Amsterdam, Elsevier.
Hauk V., Vaessen G. (1985), *Ziefrischft fur Metallkunde* **76** 102-107
Heidelbach F., Riekel C., Wenk H.-R. (1999), *Journal of Applied Crystallography* **32** 841-849
Heizmann J.-J., Laruelle C. (1986), *Journal of Applied Crystallography* **19** 467-472
Helming K. (1998), *Materials Structure* **1** 3-9
Hill R. (1952), *Proceedings of the Physical Society of London A***65**, 349-354
Hill R.J., Flack H.D. (1987), *Journal of Applied Crystallography* **20** 356-361
Hill R.J., Howard C.J. (1987), *Journal of Applied Crystallography* **20** 467-474
Houben L., Luysberg M., Carius R. (2003), *Physical Review B* **67** 045312
Howard C.J. (1982), *Journal of Applied Crystallography* **15** 615-620
Imhof J. (1982), *Textures and Microstructures* **4** 189-200
Ito T. (1949), *Nature* **164** 755-???
Jansen E., Schäfer W., Will G. (1994), *Journal of Applied Crystallography* **27** 492-496
Jin S., Sherwood R., Gyorgy E., Tiefel T.H., van Dover R., Nakahara S., Schneemayer L., Fastnacht R., Davis M. (1989), *Applied Physics Letters* **54** 584-???
Jones F.W. (1938), *Proceedings of the Royal Society* **166A** 16-???
Jouanneaux A. (1999), *Commission on Powder Diffraction Newsletter* **21** 13-???
Khattak C.P., Cox D.E.(1977), *Journal of Applied Crystallography* **10** 405-411
Klug H.P., Alexander L.E. (1974), "X-ray diffraction procedures for polycrystalline and amorphous materials" Wiley Ed., New York
Kohlbeck F., Hörl E.M. (1976), *Journal of Applied Crystallography* **9** 28-33
Kohlbeck F., Hörl E.M. (1978), *Journal of Applied Crystallography* **11** 60-61
Konings R., Haas D. (2002), Comptes Rendus de Physique **3**1013-???
Kroll U., Meir J., Torres P., Pohl J., Shah A. (1998), *Journal of Non-Crystalline Solids* **227-230** 69-???
Labat S., Gergaud P., Thomas O., Gilles B., Marty A. (2000). *Journal of Applied Physics* **87** 1172-1181
Langford J.I. (1992), "*Proceedings of the International Conference on Accuracy in powder Diffraction II*", NIST special publications **846** 110-???
Langford J.I., Boultif A., Auffrédic A., Louër D. (1993), *Journal of Applied Crystallography* **26** 22-33
Langford J.I. et Louer D. (1982), *Journal of Applied Crystallography* **15** 20-26
Langford J.I., Louër D., Sonnerveld E.J., Visser J.W. (1986), *Powder Diffraction* **1** 211-???
Larson A.C., Von Dreele R.B. (2000), "General Structure Analysis System (GSAS)", Los Alamos National Laboratory Report LAUR 86-748. http://www.ncnr.nist.gov/programs/crystallography/software/gsas.html
Le Bail A. (1992), "*Proceedings of the International Conference on Accuracy in powder Diffraction II*", NIST special publications **846**
Le Bail A. (1995), *Journal of Non-Crystalline Solids* **183** 39-42
Le Bail A., Jouanneaux A. (1997), *Journal of Applied Crystallography* **30** 265-271
Lotgering F.K. (1959), Journal of Inorganic and Nuclear Chemistry **9**, 113-123
Louër D. (1991), Materials Science Forum, **?????**

Louër D., Langford J.I. (1988), *Journal of Applied Crystallography* **21** 430-437
Louër D., Louër M. (1972), *Journal of Applied Crystallography* **5** 271-275
Louër D., Vargas R. (1982), *Journal of Applied Crystallography* **15** 542-545
Lutterotti L., Scardi P. (1994), *Journal of Applied Crystallography* **23** 246-252
Lutterotti L., Matthies S., Wenk H.-R. (1999), National Research Council of Canada, Ottawa 1999, 1599, http://www.ing.unitn.it/~luttero/maud/
Lutterotti L., Matthies S., Chateigner D., Ferrari S., Ricote J. (2002). *Materials Science Forum* **408-412** 1603-1608
Lutterotti L., Chateigner D., Ferrari S., Ricote J. (2004), *Thin Solid Films* **450** 34-41
Maeder G. (1986), *Chemica Scripta* **26A** 23-31
Malmros G., Thomas J.O. (1977), *Journal of Applied Crystallography* **10** 7-11
March ??? (1992) *Proceedings of the Royal Society* **10 ???**
Mason T. (1994). PopLA: http://www.lanl.gov/orgs/mst/cms/poplalapp.html
Matthies S. (1979), *Physica Status Solidi B* **92** K135-K138
Matthies S., Chateigner D. (2000). http://www.ecole.ensicaen.fr/~chateign/texture/working_formulaes.pdf
Matthies S., Humbert M. (1995), *Journal of Applied Crystallography* **28** 31-42
Matthies S., Lutterotti L., Wenk H.-R. (1997), *Journal of Applied Crystallography* **30** 254-256
Matthies S., Vinel G.W. (1982), *Physica Status Solidi B* **112** K111-K114
Matthies S., Vinel G.W., Helming K. (1987), ‘’*Standard Distributions in Texture Analysis’’*. **Vol 1**, Ed. Matthies, Akademie Verlag, Berlin.
Matthies S., Wenk H.-R. (1985). In "*Preferred orientation in deformed metals and rocks : an introduction to modern texture analysis*", H.-R. Wenk editor, Academic Press inc. pp 139-147
Matthies S., Wenk H.-R. (1992), *Physica Status Solidi A***133** 253-257
Matthies S., Wenk H.-R., Vinel G.W. (1988), *Journal of Applied Crystallography* **21** 285-304.
Matulis C.E., Taylor J.C. (1993), *Journal of Applied Crystallography* **26** 351-356
McCusker L.B., von Dreele R.B., Cox D.E., Louer D., Scardi P. (1999), *Journal of Applied Crystallography* **32** 36-50
Miro S., Grébille D., Chateigner D., Pelloquin D., Stoquert J.-P., Grob J.-J., Costantini J.-M., Studer F. (2004), *Nuclear Instruments and Methods in Physics Research B* **227** 306-318
Morales M., Chateigner D., Lutterotti L., Ricote J. (2002), *Materials Science Forum* **408-412** 1055-1060
Morales M., Leconte Y., Rizk R., Chateigner D. (2004), *Thin Solid Films* **450** 216-221
Morales M., Leconte Y., Rizk R., Chateigner D. (2005), *Journal of Applied Physics* **97** 034307-1 - 034307-13
Névot L., Croce P. (1980), *Revue de Physique Appliquée* **15** 761-779
Noudem J.G., Guilmeau E., Chateigner D., Lambert S., Reddy E.S., Ouladdiaf B., Schmitz G.J. (2004), *Physica C* **408** 655-656
Noudem J.-G., Harnois C., Chateigner D., Chaud X. (2003), *Applied Superconductivity* **vol. 181** 1426-1431
Noudem J.G., Meslin S., Harnois C., Chateigner D., Chaud X. (2004a), *Superconductor Science and Technology* **17** 931-936
Noyan I.C., Cohen J.B. (1987), "*Residual Stress: measurement by diffraction and interpretation"* Springer-Verlag
Noyan I.C., Huang T.C., York B.R. (1995), "*Critical Reviews in Solid State and Materials Sciences*" **20** 125-177.

Nye J.-F. (1957), "*Physical Properties of Crystals, their representation by tensors and matrices*", Oxford University Press.
Ouchani S, et al (1997) *Nuclear Instruments and Methods B* **132** 147-???
O'Connor B.H., Li D.Y., Sitepu H. (1991), *Advances in X-ray Analysis* **34** 409-415
O'Connor B.H., Li D.Y., Sitepu H. (1992), *Advances in X-ray Analysis* **35** 277-283
Ouhes R. (1984), "*Elements de radiocristallographie*", *Ed. OPU*, Alger
Parrat L.G. (1954), *Physical Review* **95** 359
Paul T.A., Fitzgerald P.G. (1992), *American Mineralogist* **77** 336-???
Pawley G.S., Mackenzie G.A., Dietrich O.W. (1977), *Acta Crystallographica* **A33** 142-145
Pawley G.S. (1981), *Journal of Applied Crystallography* **14** 357-361
Pawlik K. (1993), *Materials Science Forum* **133-136** 151-156
Pawlik K., Ozga P. (1999), LaboTex: The texture analysis software, "Göttinger Arbeiten zur Geologie und Paläontologie", SB4. http://www.labosoft.com.pl/
Pitschke W., Hermann H., Mattern N. (1993), *Powder Diffraction* **8** 74-83
Popa N.C. (1992), *Journal of Applied Crystallography* **25** 611-616
Popa N.C. (1998), *Journal of Applied Crystallography* **31** 176-180
Press W.H., Flannery B.P., Teukolsky S.A., Vetterling W.T. (1986), *Numerical Recipes*. Cambridge University Press.
Prince E. (1989), Notes available from the *American Crystallographic Association*, PO Box 96, Ellicott station, Buffalo, NY 14205-0096
Reiter G (1994), *Macromolecules* **27** 3046-???
Reuss A (1929), *Z. Angew. Math. Mech.* **9** 49-58
Richardson J.W. (1993), "*The Rietveld Method, IUCr monographs on crystallography 5*", Oxford University Press, p102-105
Ricote J., Chateigner D., Morales M., Calzada M.L., Wiemer C. (2004), *Thin Solid Films* **450** 128-133
Ricote J., Poyato R., Alguero M., Pardo L., Calzada M.L., Chateigner D. (2003), *Journal of the American Ceramic Society* **86(9)** 1571-1577
Riello P., Fagherazzi G., Clemente D., Canton P. (1995), *Journal of Applied Crystallography* **28** 115-120
Riello P., Fagherazzi G., Canton P., Clemente D., Signoretto M. (1995a), *Journal of Applied Crystallography* **28**, 121-126
Rietveld H.M. (1967), *Acta Crystallographica* **22** 151-152
Rietveld H.M. (1969), *Journal of Applied Crystallography* **2** 65-71
Robinson I.K., Tweet D.J. (1992), *Reports on Progress in Physics* **55** 599-651
Rodriguez J. (2003), Fullprof, http://www-llb.cea.fr/fullweb/fp2k/fp2k.htm
Rollett J.S. (1965), in "*Computing Methods in Crystallography*", Pergammon Press pp. 32–37
Ruer D. (1976), "*Méthode vectorielle d'analyse de la texture*", Thesis Université de Metz, France.
Ruer D., Baro R. (1977), *Advances in X-ray Analysis* **20** 187-???
Runge C. (1917), *Physics Zeitschrift* **18** 509-???
Russell T.P. (1996), *Physica B* **221** 267-???
Salzmann I., Resel R. (2004), *Journal of Applied Crystallography* **37** 1029-1033
Savitzky A., Golay M.J.E. (1964), *Anal. Chem.* **36** 1627-1639
Schaeben H. (1988), *Journal of Applied Physics* **64** 2236-???
Schaeben H. (1991), in "*Advances and applications of quantitative texture analysis*", Bunge H.-J., Esling C. Eds, DGM, Oberursel, Germany. pp109-118
Schaeben H. (1991a), *Journal of Applied Physics* **69(3)** 1320-1329
Scherrer P. (1918), *Gött. Nachr* **2** 98-???
Schulz L.G. (1949a), *Journal of Applied Physics* **20** 1030-1033

Schulz L.G. (1949b), *Journal of Applied Physics* **20** 1033-1036
Schwarz G. (1978), *Annual Statistics* **6** 461-464
Shannon C.E. (1948), *Bell System Technology Journal* **27** 623
Shannon C.E., Weawer W. (1949), "*The mathematical theory of communication*", Univ. of Illinois Press, Urbana
Shi D., Boley M.S., Chen J.G., Xu M., Vandervoort K., Liao Y.X., Zangvil A. (1989) *Applied Physics Letters* **55** 699-???
Shirane G. (1959), *Acta Crystallographica* **12** 282–287
Shirley R. (1980), *Natural Bureau of Standards, (US) special Publications* **N° 567**, 361
Shirley R. (1990), "*Computing in crystallography*", Ed. H. Shenk, Delf University Press 221
Sidey V. (2004), *Journal of Applied Crystallography* **37** 1013-1014
Smith D.K. (1989), *Reviews in Mineralogy* **17** 183-???
Smith G.S. (1977), *Journal of Applied Crystallography* **10** 252-255
Smith G.S., Snyder R.L. (1979), *Journal of Applied Crystallography* **12** 60-65
Snyder R.L. (1983), In "A*dvance in Materials Characterisation II*", Plenum Press ED. 449
Solovyov L.A. (2004), *Journal of Applied Crystallography* **37** 743-749. http://krsk.info/icct/en/cont/persons/sol/ddm.html
Sonneveld E.J., Visser J.W. (1975), *Journal of Applied Crystallography* **8** 1-7
Soulet S., et al (1997) *Nuclear Instruments and Methods B* **132** 447-???
Sparks C.J., Kumar R., Specht E.D., Zschack P, Ice G., Shiraishi T., Hisatsune K. (1992), *Advances in X-ray Analyses* **35** 57-62
Stearns, D.G. (1992), *Journal of Applied Physics* **71** 4286-4298
Stephens P.W. (1999), *Journal of Applied Crystallography* **32** 281-289
Stoev K.N., Sakurai K. (1999), *Sepctrochimica Acta B* **54** 41-82
Suortti P. (1972), *Journal of Applied Crystallography* **5** 325-331
Tampieri A., Celotti G., Calestani G., Lesca S. (1997), *Key Engineering Materials Euro Ceramics V* **132** 1247-???
Taupin D. (1973), *Journal of Applied Crystallography* **6** 380-385
Taylor J.C., Miller S.A., Bibby D.M., *Zeitschrift fuer Kristallographie* (1985) **176** 183-???
Thompson P., Cox D.E., Hastings J.B. (1987), *Journal of Applied Crystallography* **20** 79-83
Toraya H. (1986), *Journal of Applied Crystallography* **19** 440-447
Uzumaki T., Yamanaka K., Kamehara N., Niwa K. (1989), *Japanese Journal of Applied Physics* **1** 75-???
Vadon A. (1981), "*Généralisation et optimisation de la méthode vectorielle d'analyse de la texture*". Thesis, Université de Metz.
Vallat-Sauvain E., Kroll U., Meier J., Shah A. (2000), *Journal of Applied Physics* **87(6)** 3137-3142
Van den Hoogendorf W., de Boer D.K.G. (1994), *Surface and Interface Analysis* **22** 169-???
Vidal J., Vincent ??? (1984), *Applied Optics* **23** 1794-1801
Vignaud G., Gibaud A., Grübel G., Joly S., Ausserré D., Legrand J.F., Gallot Y. (1998), *Physica B* **248** 250-257
Visser J.W. (1969). A fully automatic program for finding the unit cell from powder data. *Journal of Applied Crystallography* **2** 89-95
Voigt W. (1928), *Lehrbuch der Kristallphysiks* (Leipzig: Teubner).
Von Dreele R.B. (2002), http://www.ncnr.nist.gov/programs/crystallography/software/gsas.html
Von Dreele R.B., Jorgenson J.D., Winsdor C.G. (1982), *Journal of Applied Crystallography* **15** 581-589
Wagner G.N.J. (1966), *Metallurgical Society Conference* **36** 219-???

Wagner F., Dahms M. (1991), in "*Advances and applications of quantitative texture analysis*", Bunge H.-J. et Esling C. Eds, DGM, p101-108
Wang M., Xiong G., Tang X., Hong Z. (1993), *Physica* C **210** 413-???
Wang S., et al, (2000), *Nuclear Instruments and Methods B* **166-167** 293-???
Warren B.E. (1969), "*X-ray diffraction*", Ed. Addison-Wesley, Reading, Massachusetts, New-York
Weber W., et al (1997), *Journal of Nuclear Materials* **250** 147-???
Weber W., et al, (1998), *Journal of Materials Research* **13** 1434-???
Welzel U., Ligot J., Lamparter P., Vermeulen A.C., Mittemeyer E.J. (2005), *Journal of Applied Crystallography* **38** 1-29
Welzel U., Mittemeyer E.J. (2003), *Journal of Applied Physics* **93** 9001-9011
Wenk H.-R. (1992), *Journal of Applied Crystallography* **25** 524-530
Wenk H.-R., Heidelbach F., Chateigner D., Zontone F. (1997), *J. Synchrotron Radiation* **4** 95-101
Wenk H.-R., Matthies S., Donovan J., Chateigner D. (1998), *Journal of Applied Crystallography* **31** 262-269
Wenk H.-R., Matthies S., Lutterotti L. (1994), *Materials Science Forum* **157-162** 473-479
Wenk H.-R., Pawlik K., Pospiech J., Kallend J.S. (1994), *Texture and Microstructure* **22** 233-260
Werner P.E. (1964), *Zeitschrift für Kristallographie* **120** 375-???
Werner P.E., Erickson L., Westdahl H. (1985), *Journal of Applied Crystallography* **18** 367-370
Wiles D.B., Young R.A. (1981), *Journal of Applied Crystallography* **14** 149-151
Willemse P.F., Naughton B.P., Verbraak C.A. (1982), *Materials Science and Engineering* **56** 25-37
Williams R.O. (1968), *Journal of Applied Physics* **39** 4329-???
Wilson A.J.C. (1963), "*Mathematical Theory of x-ray Powder Diffractometry*", Eindhoven, centrex
Young R.A., Larson A.C., Paiva-Santos C.O. (1999), DBWS-9807a, *Program for Rietveld analysis of x-ray and neutron powder diffraction patterns.* School of Physics, Geargia Institute of Technology, Atlanta, Georgia, USA
Young R.A., Mackie P.E., Von Dreele R.B. (1977), *Journal of Applied Crystallography* **10** 262-269

Used variables:

dS	Surface element of the Pole Sphere
a, b, c, α_c, β_c, γ_c	Unit-cell parameters
a, **b**, **c**	Unit vectors of the unit-cell
Δk	Scattering vector
n	Normal to the sample surface
$\mathcal{S}$	Spectrometer (Diffractometer) space
χ	Polar angle in the diffractometer space
φ	Azimuthal angle in the diffractometer space
$\mathcal{Y}$	Pole figure space
ϑ_y	Polar angle in the pole figure space
φ_y	Azimuth of pole figures
hkℓ	Miller indices
(hkℓ)	Crystallographic plane hkℓ
{hkℓ}	Crystallographic planes hkℓ and diffracting equivalents
[hkℓ]	Crystallographic direction hkℓ
[hkℓ]*	Crystallographic direction hkℓ of the reciprocal space
<hkℓ>	Crystallographic direction hkℓ and diffracting equivalents
<hkℓ>*	Crystallographic direction hkℓ and diffracting equivalents of the reciprocal space
$L_{hk\ell}$	Lotgering factor
p, p_0	ratio entering the Lotgering factor for a textured and a random sample respectively
h	<hkℓ>* directions
y	ϑ_y, φ_y direction in
$I_{\mathbf{h}}(\mathbf{y})$	Direct pole figure
$P_{\mathbf{h}}(\mathbf{y})$	Normalised pole figure
K_A	Sample reference frame
($\mathbf{x_A}$, $\mathbf{y_A}$, $\mathbf{z_A}$)	Unit-vectors of the sample reference frame
X_A, Y_A, Z_A	Sample axes aligned with $\mathbf{x_A}$, $\mathbf{y_A}$, $\mathbf{z_A}$ respectively
[XYZ]	Vector of the sample reference frame
($\mathbf{x_B}$, $\mathbf{y_B}$, $\mathbf{z_B}$)	Unit-vectors of the crystal reference frame
X_B, Y_B, Z_B	Sample axes aligned with $\mathbf{x_B}$, $\mathbf{y_B}$, $\mathbf{z_B}$ respectively
$\mathcal{H}$	Orientation space
g	Set of three Euler angles defining one orientation
g	Orientation distance
dg	Orientation element in the $\mathcal{H}$-space
α, β, γ	Euler angles in the $\mathcal{H}$-space in the Roe-Matthies convention
φ_1,Φ,φ_2	Euler angles in the $\mathcal{H}$-space in the Bunge convention
f(g)	Orientation Distribution Function
$d_{hk\ell}$,	Inter-reticular distance between (hkℓ) planes
ω	Angle between the incident beam and the sample surface: incidence angle
θ	Angle between the incident beam and the scattering planes {hkℓ}: Bragg angle
δ	Angle running along the Debye ring on a 2D detector
V	Irradiated volume of the sample

dV(**y**)	Volume of crystallites having **h** between **y** and **y** + **dy**
dV(g)	Volume of crystallites which orientation is between g and g + dg
Jc	Superconducting transport critical current density
Fd	Damaged (amorphous) fraction of an irradiated sample
Fc	Crystalline fraction of a sample
$\overline{\mathcal{T}}$	Microscopic tensor for a property
$\overline{\mathcal{T}}^{M}$	Macroscopic tensor
$<\overline{\mathcal{T}}>$	Arithmetic average of the tensor $\overline{\mathcal{T}}$
ε_{ij}	strain tensor
ε_{ij}^{M}	macroscopic strain tensor
σ_{ij}	stress tensor
σ_{ij}^{M}	macroscopic stress tensor
$S_{ijk\ell}$	elastic compliance tensor
$S_{ijk\ell}^{M}$	macroscopic elastic compliance tensor
$S_{ijk\ell}^{V,R,H}$	macroscopic elastic compliance tensor calculated using the Voigt, Reuss, Hill models
$C_{ijk\ell}$	elastic stiffness tensor
$C_{ijk\ell}^{M}$	macroscopic elastic stiffness tensor
$C_{ijk\ell}^{V,R,H}$	macroscopic elastic stiffness tensor calculated using the Voigt, Reuss, Hill models
ξ	mixing parameter of the Hill model

Abbreviations:

14:24	$(Sr,Ca)_{14}Cu_{24}O_{41}$
Bi2223	$(Bi,Pb)_2Sr_2Ca_2Cu_3O_{10+x}$
Bi2212	$(Bi,Pb)_2Sr_2Ca_1Cu_2O_{8+x}$
CPS	Curved Position Sensitive detector
ESR	Electron Spin Resonance
Fap	$Ca_{10}(PO_4)_6F_2$
FWHM	Full Width at Half Maximum
HAp	$Ca_{10}(PO_4)_6(OH)_2$
HWHM	Half Width at Half Maximum
HWHD	Half Width at Half maximum of the distribution Density
ILL	*Institut Laue-Langevin*
m.r.d.	multiple of a random distribution
MTG	Melt Texture Growth
NMR	Nuclear Magnetic Resonance
ODF	Orientation Distribution Function
PSD	Position Sensitive Detector
QMA	Quantitative Microstructure Analysis
QPA	Quantitative Phase Analysis
QTA	Quantitative Texture Analysis
RSA	Residual Strain-stress Analysis
SEM	Scanning Electron Microscope
TEM	Transmission Electron Microscope
TSMTG	Top-Seeded Melt Texture Growth
XRR	X-Ray specular Reflectivity
Y123	$YBa_2Cu_3O_{7-\delta}$
Y211	Y_2BaCuO_5

Mathematical operators

Vectors are in bold
Unless specified, diffraction means "normal diffraction" (opp. anomalous diffraction)
^: vector product
.: scalar product
⊗: convolution product
*: as a superscript of a matrix, stands for the complex conjugated
as a superscript of a vector, stands for the vector of the reciprocal space
:: division of tensors
erfc: complementary error function
<>: arithmetic average of a tensor

Tensor notations:

Tensors are represented by matrices, following the Nye [1957] notation, for instance for a 2nd order tensor:

$$\mathcal{T} = \begin{vmatrix} \bullet & \bullet & \bullet \\ \bullet & \bullet & \bullet \\ \bullet & \bullet & \bullet \end{vmatrix} = \begin{vmatrix} T_{11} & T_{12} & T_{13} \\ T_{21} & T_{22} & T_{23} \\ T_{31} & T_{32} & T_{33} \end{vmatrix}$$

●	non-zero values
●—●	identical values (different from zero)
●—○	opposite values
⊙	twice the ● component to which it is linked
◎	opposite to the twice of the ● component to which it is linked
×	value linked to others by a specific relationship, *e.g.* $2(s_{11} - s_{12}) = s_{44}$

all tensors are symmetric relative to their main diagonal.

Acknowledgements

This work could not have been carried out without supports from the following institutions, through constant financial or contracts:

- Ministère de l'Enseignement Supérieur et de la Recherche
- Délégation Régionale à la Recherche et à la Technologie, Basse-Normandie
- GdR Nomade: Groupement de Recherche "NOuveaux MAtériaux pour les Dechets radioactifs"
- CNRS-CSIC French-Spanish cooperation "Crystallographic texture influence on polycrystalline ferroelectric materials properties" (contract n° 16215, 2004-2005)
- European project ESQUI "X-ray Expert System for microelectronic films Quality Improvements"
- CNRS-CSIC French-Spanish cooperation "PTL, SBT and PTC ferroelectric film characterisation" (contract n° 8540, 2000-2001)
- European Concerted Action "ELENA: ELEctroceramics from NAnopowders produced by innovative methods" (COST n° 539, 2005-2009)
- European Concerted Action "Application of ferroelectric thin-films for SAW devices" (COST n° 514, 1998)

Warnings and comments

This text is appended regularly. If you detect any incoherence, mistake, typos, lost or missing reference or whatsoever, or if you miss some explanation or development, please warn the author directly by email at daniel.chateigner@ensicaen.fr

Figures caption

Tables caption